ISSN 0377-9416

PMAI

www.pmai.in

TRANSACTIONS OF POWDER METALLURGY ASSOCIATION OF INDIA

Vol. 48, June-December 2023

Chief Editor - **Dr. Deep Prakash**

ISSN 0377-9416

www.pmai.in

TRANSACTIONS OF POWDER METALLURGY ASSOCIATION OF INDIA

Vol. 48, June-December 2023

Chief Editor - **Dr. Deep Prakash**

Powder Metallurgy Association of India

Office Bearers

President
Mr. Aniket Gore

Vice President
Dr. N. B. Dhokey
Mr. Sandeep Fatangare
Mr. Rajendra Sethiya
Mr. Niranjan Narkhede

General Secretary
Mr. Prakash Khole

Joint Secretary
Dr. Malobika Karanjai
Mr. Deepak Kumar Pattanayak

Hon. Treasurer
Mr. Mahesh Nipanikar

Price Rs. 500/-

Chief Editor
Dr. Deep Prakash

Managing Editor
Dr. V. C. Srivastava

Editorial Advisory Board
Prof. Ajit R. Kulkarni
Prof. Anish Upadhyay
Prof. B. S. Murty
Dr. G. Appa Rao
Prof. J. Konstanty
Dr. Litström Ola
Prof. Manoj Gupta
Prof. N. K. Mukhopadhyay
Prof. Satish Kumar Ogale
Prof. Shrikant Joshi
Dr. Suman K. Mishra
Dr. V. Uhlenwinkel

Editorial Board
Dr. Amartya Mukhopadhyay
Dr. Amit Sinha
Dr. Bharat Panigrahi
Dr. Deepak K. Pattanayak
Dr. Ilya Okulov
Dr. Joydip Joardar
Dr. Kumarbabu Surreddi
Dr. Malobika Karanjai
Prof. N. V. Ravikumar
Dr. N. B. Dhokey
Prof. P. Gargarella
Dr. Saurabh Nene
Dr. Sergio Scudino
Prof. S. P. Butee
Dr. T. Mahata
Dr. Vikram Dabhade

Published by :
Powder Metallurgy Association of India (PMAI)
102, Anandi, 1st Floor,
M.B. Raut Road, Shivaji Park, Dadar,
Mumbai - 400028, India
Tel.: +91 9820951180
+91 9821111677
E-mail: info@pmai.in

Neither the Powder Metallurgy Association of India nor the editor assumes responsibility of opinions expressed by the authors of the papers published in this transaction.

Editorial

We are very happy to present you this latest volume of Trans. PMAI, as it is the first volume coming out after re-constituted Editorial as well as Advisory Boards, which we believe, are more inclusive and wide-spread across this tiny field of work. The papers contained in this volume are a selected lot from the works presented during the International Conference on Powder Metallurgy, held at The Lalit, Mumbai from 13th -15th March 2023. As the scientific journals are chronicles of contemporary works being conducted to update technological prowess in the field, the selection of the papers is done to this effect. As there are continuous progress in some super-speciality, critical reviews become necessary to pause and take a stock for the benefit of researchers. This volume contains three review-papers, on the topics 'Metal-organic frameworks', 'Additive Manufacturing of Ni-based Superalloys' and 'Thermoelectricity', which are all emerging areas of advanced research. Further, it is interesting to observe that since the time of classical paper by Benjamin, 'Mechanical Alloying' is still well sought-after work, and finding its usage for multi-components systems such as Fe-Cr-Mo or high-entropy alloys, as is evident from the two papers in this volume. In addition, as P/M has marked its place as one of the most significant manufacturing methods, correlating process parameters and properties and their evaluation carries important scientific information to be disseminated among the fraternity. Papers on feedstock preparation for thermal spraying, effect of pre-heat temperature on swarf, processing of Al with W-dispersoids, wear performance of PA-6, ZnO powders, thermal conductivity of Alumina-boride and residual stresses are testimonial to this surmise. Last two papers in the volume indicate some encouraging trends. The paper on numerical methods for the air-jet mill is a welcome work for optimization of machinery used for P/M processing, whereas commitment of scientific fraternity towards environment-friendliness is witnessed in the efforts to develop lead-free piezoelectric as detailed in the last paper of the volume. We hope the PM fraternity of researchers, teachers, industry, equipment manufacturers and students will benefit by these works.

With warm regards

Dr. Deep Prakash

CHIEF EDITOR	
Dr. Deep Prakash	Department of Atomic Energy, New Delhi, India
MANAGING EDITOR	
Dr. V. C. Srivastava	CSIR-National Metallurgical Laboratory, Jamshedpur, India
EDITORIAL ADVISORY BOARD	
Prof. Ajit R. Kulkarni	Indian Institute of Technology Bombay, Mumbai, India
Prof. Anish Upadhyay	Indian Institute of Technology, Kanpur, India
Prof. B. S. Murty	Indian Institute of Technology, Hyderabad, India
Dr. G. Appa Rao	Defence Metallurgical Research Laboratory, Hyderabad, India
Prof J. Konstanty	AGH University of Science & Technology, Krakow, Poland
Dr. Litström Ola	Höganäs AB, Höganäs, Sweden
Prof. Manoj Gupta	National University of Singapore, Singapore
Prof. N. K. Mukhopadhyay	Indian Institute of Technology (BHU), Varanasi, India
Prof. Satish Kumar Ogale	Indian Institute of Science Education & Reserach, India
Prof. Shrikant Joshi	University West, Trollhaettan, Sweden
Dr. Suman K. Mishra	CSIR-Central Glass and Ceramic Research Institute, Kolkata, India
Dr. V. Uhlenwinkel	Leibniz InstitutfuerWerkstofftechnik, Bremen, Germany
EDITORIAL BOARD	
Dr. Amartya Mukhopadhyay	Indian Institute of Technology Bombay, Mumbai, India
Dr. Amit Sinha	Bhabha Atomic Research Centre, Mumbai, India
Dr. Bharat Panigrahi	Indian Institute of Technology, Hyderabad, India
Dr. Deepak K. Pattanayak	CSIR-Central Electrochemical Research Institute, Karaikudi, India
Dr. Ilya Okulov	Leibniz Institut fuer Werkstofftechnik, Bremen, Germany
Dr. Joydip Joardar	International Advanced Research Centre for Powder Metallurgy and New Materials (ARCI), Hyderabad, India
Dr. Kumarbabu Surreddi	Luleå University of Technology, Luleå, Sweden
Dr. Malobika Karanjai	International Advanced Research Centre for Powder Metallurgy and New Materials (ARCI), Hyderabad, India
Prof. N.V. Ravikumar	Indian Institute of Technology Madras, Chennai, India
Dr. N. B. Dhokey	College of Engineering Pune, Pune, India
Prof. P. Gargarella	Universidade Federal de São Carlos - UFSCar, Brazil
Dr. Saurabh Nene	Indian Institute of Technology, Jodhpur, India
Dr. Sergio Scudino	Institute of Complex Materials, IFW Dresden, Germany
Prof. S P Butee	College of Engineering Pune, Pune, India
Dr. T. Mahata	Bhabha Atomic Research Centre, Mumbai, India
Dr. Vikram Dabhade	Indian Institute of Technology, Roorkee, India

TRANSACTIONS OF
POWDER METALLURGY ASSOCIATION OF INDIA

Vol. 48, June-December 2023

CONTENTS

ASSESSMENT OF PROCESS PARAMETERS FOR MECHANICALLY ALLOYED $Fe_{(84-x)}$-16% Cr-Mo_x ALLOYS

Subrahmanyam S[1*], Pardhasaradhi R[1] and SunilKumar R[1]

[1]Department of Metallurgical & Materials Engineering, NIT Andhra Pradesh, India.
*subbuaugust1987@gmail.com

Abstract: *The addition of molybdenum in ferritic stainless-steel compositions will improve the surface properties such as hardness and pitting corrosion resistance, which facilitates its use in most surface engineering applications. In this study, Iron-based $Fe_{(84-x)}$-16%Cr-Mo_x alloys with x = 0%, and 3% (by weight) of molybdenum addition are prepared by the mechanical alloying process at different milling times using a planetary ball mill, followed by cold compaction and conventional sintering process steps. The phaseevolution studies of the mechanically alloyed $Fe_{(84-x)}$-16%Cr-Mo_x powders milled for 0h, 1h, 5h, 15h & 30h are investigated by X-Ray diffraction. Morphological assessment & mechanical properties of these sintered compacts were investigated by optical microscopy, and the Vickers hardness testing respectively. The changes in lattice parameter, crystallite size & lattice strain in the mechanical alloyed $Fe_{(84-x)}$-16%Cr-Mo_x (x = 0 & 3%)alloys were evaluated.*

Keywords: *Mechanical alloying; Fe-Cr-Mo alloys; X-ray diffraction; Crystallite Size; Lattice Strain; Sintering; Microhardness;*

1. Introduction

Iron-based alloys & steels developed through powder metallurgy routes have gained huge importance owing to their applications in various fields of engineering including structural components, energy storage devices, automotive parts, etc.[1-4]. However, the mechanical, tribological, and corrosion evaluation of these iron - chromium- based alloys which are nanocrystalline in nature require samples in bulk quantity. These materials, thus require mechanical alloying (MA) for the synthesis of artifact-free nanocrystalline alloys in bulk quantities [5]. The alloying elements present in the PM-Steels dictate its fabrication & development and Powder metallurgy process parameters employed during the fabrication, and further influence the mechanical properties of these materials. The process-friendly alloying elements of PM-Steel include Cu, Ni, and Mo, which are generally used in low compositions. The use of less costly alloying elements is preferred in the PM industry when hardenability is a major criterion for steel making. However, Cris a very good alternative when high hardenability is desired and a low-cost material compared to other hardenable materials such as Vanadium. The limitation of Cris that it has a high affinity for oxygen, which turns the Powder metallurgical processing of Cr-alloyed materials challenging during its oxidation and oxide reduction [6]. However, Cr-Mo alloy steels possess higher creep resistance at elevated temperatures and can be used in various high-temperature applications including boilers, pressure vessels, etc. Sintering of Cr-Mo steels at high temperatures yields enhanced mechanical properties [7], thus, recommending the importance of Mo alloying in different types of steels for various applications. The diffusion mechanism of Mo & Cr during the sintering of Fe-Cr-Mo-based alloys will help in estimating the improved density and hardness [8,9].

The existing literature reported limited studies on ball-milled high chromium Fe-based alloys and their impact on mechanical properties and corrosion behavior [10-12]. However, the influence of Mo addition on the phase evolution, mechanical properties, and electrochemical properties of Stainless-Steel compositions fabricated through the PM route is not reported in the literature published so far [13]. This paper

investigated the phase evolution of $Fe_{(84-x)}$-16%Cr-Mo_x (x = 0 & 3) alloys developed through the MA technique of powder metallurgy and presented results.

2. Materials & Experimental Methods

Iron, Chromium, and Molybdenum metal powders of high purity are considered for this study, with specifications as mentioned in Table 1. The designed compositions of these metal powders are pre-mixed and ball milling is performed in a planetary ball mill (Retsch PM 100, Germany), by maintaining a ball-to-powder ratio of 10:1. The cylindrical vial of 125ml capacity is filled with 25 grams of pre-mixed powder of corresponding $Fe_{(84-x)}$-16wt.%Cr-Mo_x compositions, which is then loaded into the ball mill and a rotational velocity of 300 rpm is maintained. A milling cycle of 1 hour with a pause time of 20 minutes is considered, and 30 cycles are implemented for all sample compositions.

Table1: Specifications of elemental metal powders

Material	Particlesize (microns)	Purity(%)
Iron powder	45-50µm	99.9
Chromium powder	45-50µm	99.0
Molybdenum powder	45-50µm	99.99

Diffraction patterns are recorded using an X-ray diffractometer (Rigaku Ultima III, Japan) from as-mixed & milled $Fe_{(84-x)}$-16wt.%Cr-Mo_x (x=0&3) alloy powder samples prepared during MA with ball milling technique. Parameters considered for diffractometry include as can rate of 2◦/min, a step size of 0.02 degrees &Wavelength of radiation kα =0.154056nm, and a 30◦-90◦scan range considered. Phase analysis is carried out by using PANalytical X'pert high- score software and the developed phases were analyze during the ICDD PDF-2 database [14]. Lattice parameter values for as-mixed (0h) & milled $Fe_{(84-x)}$-16wt.%Cr-Mo_x(x = 0 & 3) powder at different time periods are calculated by determining the inter planar spacing value 'd'for the highest peak (011)and then the below equation was employed:

$a=d.(h^2+k^2+l^2)^{0.5}$……. (1)

Here: (h k l)=Plane of indexing

d = Interplanar spacing

a = Lattice parameter (A°)

The crystallite size and lattice strain estimates were done for the highest diffraction peak Fe(011)using the following Williams on-Hall equation [15]:

$\beta_{hkl}.cos\theta= k\lambda/D+4\varepsilon sin\theta$ …….. (2)

Here: D=crystallite size (A◦)

K=shape factor (K=0.904; Constant);

λ = wavelength of the X-ray source (1.5406A◦); & β_{hkl}=corrected instrumental broadening (FWHM Value in A◦);

These powders are further compacted using a hydraulic press with a load of 550 MPa to prepare samples of 10mm diameter. The compacts are then sintered at 1200°C for 90 minutes using a nitrogen gas atmosphere and then furnace-cooled [8]. An optical microscope was used for microstructure studies of the sintered $Fe_{(84-x)}$-16%Cr-Mo_x(x= 0 and 3) alloys. Micro hardness readings were taken at a load of 50 grams for both the sintered alloys, for a dwell time of 15 seconds.

3. Results and Discussion

The dissolution of Chromium & Molybdenum present in the ferrite matrix will occur upon sintering the as-mixed Fe-16%Cr-3%Mo alloy. The distribution of alloying elements Cr, and Mo in the ferrite matrix and the formation of Fe-Mo

& Cr-Mo intermetallic compounds (if any) in the sintered alloys can be evaluated from optical microscopy & XRD analysis respectively.

3.1 Microstructure examination

The optical microscope investigations for sintered Fe-16% Cr-3%Moalloy are carried out by following standard metallography procedures. The polished specimens are etched with Ralph's agent for 20 seconds. Figure1(a), & 1(b) shows the ferrite phase microstructures of Fe-16%Cr-3%Moalloy at different magnifications. Molybdenum and chromium are expected to dissolve in the α-ferrite matrix upon the mechanical alloying process.

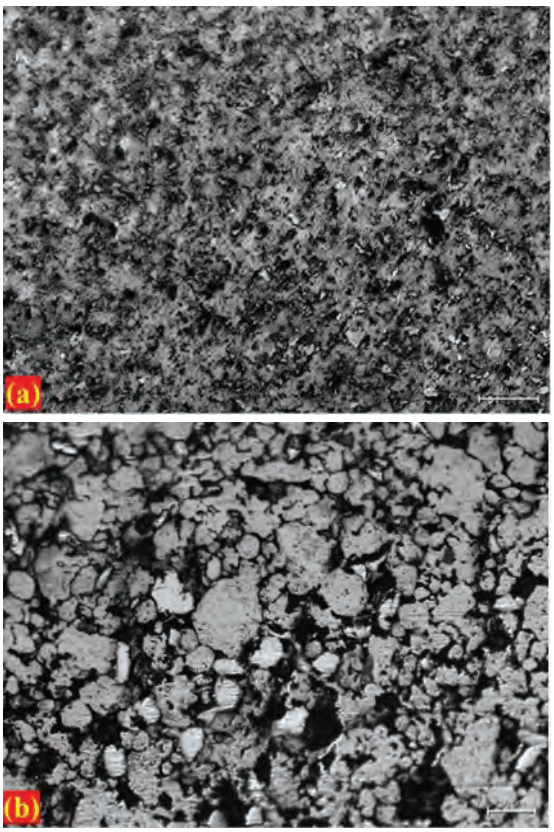

Figure 1: Microstructure of Sintered Fe-16% Cr-3% Moalloy.

The subsequent sintering treatment of these alloys is depicted in Figure 2. This will favor further densification and strengthening by diffusion, which results in the development of Mo-Fe intermetallic compounds. Agglomeration of Molybdenum with Iron is developed, which will then improve the bond strength between Fe & Mo elements in the ferrite matrix during sintering treatment, and a harder phase will be developed.

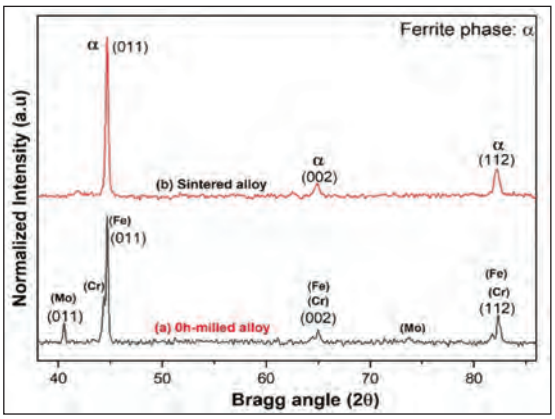

Figure 2: X-Ray diffraction of (a) As-mixed (0h-milled)&(b) sintered; Fe-16%Cr-3%Mo alloy.

3.2 Phase evolution of mechanically alloyed Fe (84-x)-16%Cr-Mox alloys: XRDAnalysis

X-Ray diffraction studies are conducted to determine the phase evolution at the beginning and after regular intervals of ball-milled $Fe_{(84-x)}$-16% Cr-Mo_x alloys. Figure 3, depicts the XRD spectra of these $Fe_{(84-x)}$-16% Cr-Mo_x (x = 0 and 3) wt.% alloys for different milling times.

It is clear from Figure 3 (a) that the powder mixture of $Fe_{(84-x)}$-16%Cr-Mo_x (x = 0) wt.% prior to milling (0 h) & milled for 1 hour has Fe and Cr clear peaks, upon further milling up to 30h, the intensity of the major peak is decreasing, and the corresponding width of the peak was slightly increased indicating the particle refinement [16]. It is also observed from Figure 3 (a) that the α-Fe

peak in the (011) plane is shifted towards lower diffraction angles from 5h, 15h, and up to 30h milling times, which shows an increase in the lattice parameter of Fe. This increase is due to the bigger size of the Cr atom compared to Fe; hence, the development of a solid solution is seen for a 5h milled alloy with Crdis solution in the Fe matrix [15]. Ball milling at 15h further broadens the α-Fe (011) peak, and the formation of fine particles is attributed to the corresponding peak broadening [16]. Also, the XRD of this alloy milled for 30h recorded almost a similar intensity of the Fe (011) peak to that of the 15h milled peak, which indicates the formation of saturation of chromium dissolved in the ferrite matrix.

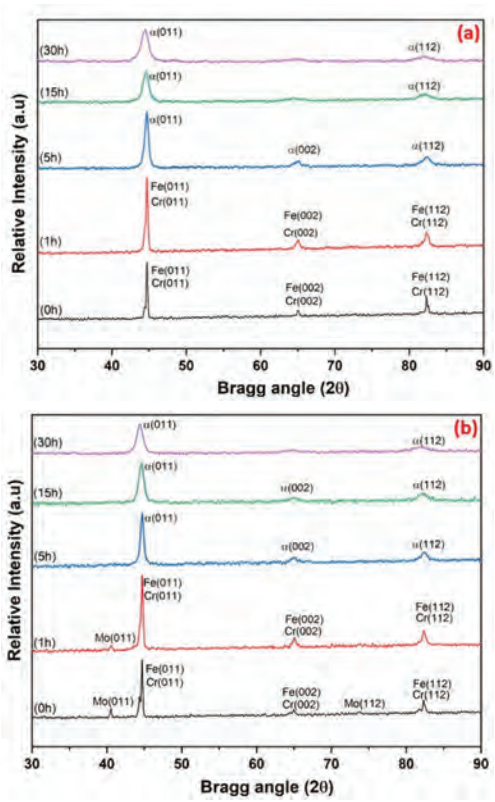

Figure 3: XRD Spectra of $Fe_{(84-x)}$-16%Cr-Mo_x alloys for (a)x=0%; (b)x =3%; milled for 0h,1h, 5h, 15h & 30h.

Figure 3 (b) discussed the phase evolution of $Fe_{(84-x)}$-16% Cr-Mo_x alloy when 3%Mo was added to the alloy. It is understood that a similar behavior to that of the alloy presented in Fig.3 (a) was observed. Amorphous phase formation is prevalent in $Fe_{(84-x)}$-16%Cr-Mo_x(x = 0 & 3) alloys when milled for longer milling durations, as per the results presented in Figures 3 (a) and (b). Further reported by other researchers on different Fe-Cr-based alloys[15, 17].

3.3. Calculation of Lattice parameter, Crystallite size & Lattice strain for MA$Fe_{(84-x)}$-16% Cr Mo_x alloys

The change in lattice parameter value at different milling durations (0, 1, 5, 15, and 30h) can be seen in Figure4. The lattice parameter value is found to increase, for both Fe-16%Cr&Fe-16%Cr-3% Mo alloys, from 0h to 30 h of milling. It is understood from Figure 4 that when milling time is increased, the α-Fe (011) peak is broadened, and a slight shift in the peak to a lower Bragg angle, which is found in both the $Fe_{(84-x)}$-16%Cr-Mo_x(x=0&3) alloys, which indicates an increase in lattice parameter [16, 17]. During the initial stages of milling (at 5h), Cr dissolution in Fe lattice in $Fe_{(84-x)}$-16%Cr-Mo_x (x = 0) alloy and the dissolution of both Cr, & Mo in $Fe_{(84-x)}$-16%Cr-Mo_x (x = 3) alloy will form a supersaturated solid solution. Since Cr (0.128 nm)& Mo (0.139 nm), atoms are larger in size than Fe atoms (0.126 nm), there is an increase in the lattice parameter of α-phase, which forms a solid solution as was observed in Figure 4 (from 5h to 30h of milling time). The value of the lattice parameter for $Fe_{(84-x)}$-16%Cr-Mo_x (x = 0) & $Fe_{(84-x)}$-16%Cr-Mo_x (x=3) alloys was increased upto 30h of milling.

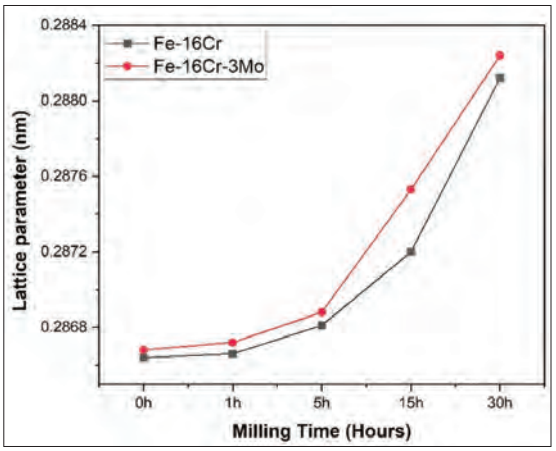

Figure 4: Changein Lattice parameter for $Fe_{(84-x)}$-16% Cr-Mo_x (x=0&3) alloys with milling time

The variation in crystallite size for $Fe_{(84-x)}$-16%Cr-Mo_x(x=0,&3) alloys with the increase in milling time is reported in Figure 5. It is found that an increase in milling time resulted in decreased crystallite size for both alloys. However, it is found that the drop in crystallite size for 3 wt.% Mo $Fe_{(84-x)}$-16%Cr-Mo_x alloy is relatively higher as compared to0wt.% Mo alloy and this variation is the result of the increased strain energies with the addition of Mo in these alloys[17,18].

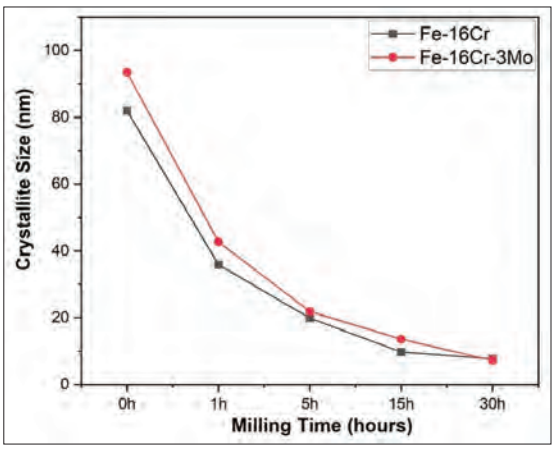

Figure 5: Change in Crystallite size for $Fe_{(84-x)}$-16%Cr-Mo_x (x=0 &3) alloys with milling time

The variation in Lattice strain for both the alloys $Fe_{(84-x)}$-16% Cr-Mo_x (x=0,3) with raise in milling time is illustrated in Figure 6. The lattice strain was found to increase as a function of milling time, with the development of higher strain energies during the higher ball milling time periods of 15h & 30h.

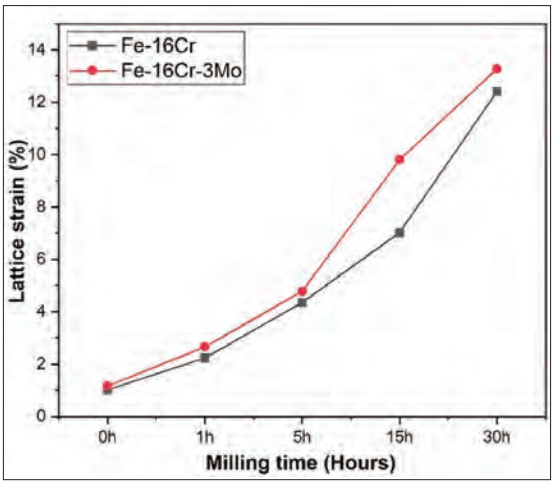

Figure 6: Change in Lattice strain of a-phase in $Fe_{(84-x)}$-16% Cr-Mo_x(x =0&3) alloys with milling time

3.4. Micro hardness of sintered $Fe_{(84-x)}$)-16% Cr Mo_x alloys

The hardness values of the sintered compacts of Fe_{84-x}-16%Cr-Mo_x(x = 0 & 3) alloys ball milled at different time periods are shown in Figure 7. It is found that the addition of Mo content of the sintered Fe-Cr-Mox alloys increased the surface hardness due to the formation of intermetallic compounds formed by molybdenum with chromium and iron present in these alloys during mechanical alloying and strengthened with the subsequent sintering treatment of the cold compacts developed by powder die compaction technique.

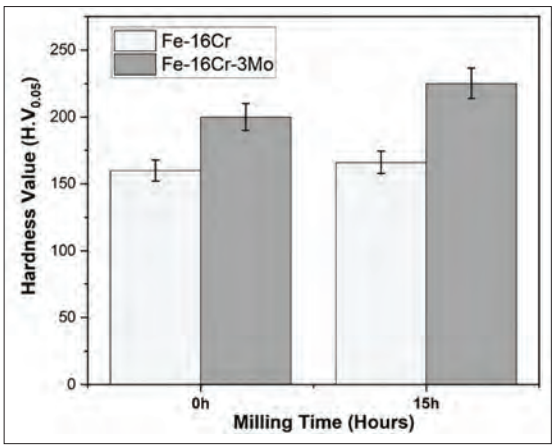

Figure 7: Hardness of Sintered $Fe_{(84-x)}$-16% Cr-Mo_x (x = 0 & 3) alloys milled at both 0h & 15h

4. Conclusions

The mechanical alloyed $Fe_{(84-x)}$-16% Cr-Mo_x (x=0&3) alloys, developed at different milling times are investigated using XRD analysis to understand the phase evolution. It is also found that,

- The formation of solid solution is identified with the α-Fe phase at 5h of milling and it continued upto 30h of milling in both the alloys $Fe_{(84-x)}$-16% Cr-Mo_x(x=0&3).
- The decrease in crystallite size and a corresponding increase in lattice strain with the rise in the milling time for both the $Fe_{(84-x)}$-16%Cr-Mo_x(x =0 &3) alloys.
- Hardness of sintered compacts of both $Fe_{(84-x)}$-16%Cr-Mo_x(x=0&3) alloys is increased for15h milled alloys when compared to as-mixed (0h) compositions.
- However, the pores are still present in these sintered alloys, which may be further controlled by adapting advanced hot consolidation techniques.

Acknowledgments

The authors are thankful and acknowledge the support provided by all the working staff of the Department of Metallurgical & Materials Engineering, NIT Andhra Pradesh to carry out this work.

References

1. Al-Mangour, Bandar. "Powder metallurgy of stainless steel: state-of-the-art, challenges, and development." Stainless Steel: Microstructure, Mechanical Properties and Methods of Application:Nova Science Publishers (2015):pp.37-80.
2. Klar,Erhard,and Prasan K.Samal. Powdermetallurgy stainlesssteels: processing, microstructures, and properties. ASM International, 2007.
3. Makhmutov, Tagir, Nikolay Razumov, Artem Kim, Sergey Ganin, Alexey Shamshurin, Anatoliy Popovich, and VeraPopovich. "Microstructure and mechanical properties of high-nitrogen 16Cr-2Ni-Mn-Mo-xN stainless steel obtained by powder metallurgy techniques."Materials Today: Proceedings 30(2020):pp.768-772.
4. Ma, Lina, Cancan Zhang, Yuting Wu, and Yuanwei Lu. "Comparative review of different influence factors on molten salt corrosion characteristics for thermal energy storage." Solar Energy Materials and Solar Cells235 (2022):111485.
5. SuryanarayanaC,"Bibliographyonmechanicalalloyingandmilling,CambridgeInt."Sci.Publ(1995).
6. Bergman, Ola, Björn Lindqvist, Sven Bengtsson, "Influence of sintering parameters on the mechanical performance ofPM steels pre-alloyed with chromium." In Materials Science Forum, Trans Tech Publications Ltd, (2007): vol. 534, pp.545-548.
7. Park, Jooyoung,Gowoon Jeong,Sing on Kang, Seok-JaeLee, Hyunjoo Choi,"Fabrication of Fe-Cr-Mo powder metallurgy steel via a mechanical-alloying process."Metals and Materials International (2015):21(6),pp.1031-1037.
8. Chauhan, Sandeep, Vikas Verma, Ujjwal Prakash, P. C. Tewari, and Dinesh Khanduja, "Studies on induction hardeningofpowder-metallurgy-processedFe–Cr/Moalloys."International Journal of Minerals, Metallurgy, and Materials (2017):24(8), pp.918-925.

9. T. Marcu, A. Molinari, G. Straffelini, and S. Berg: Microstructure and tensile properties of 3%Cr-0.5%Mo high carbon PM sintered steels, Powder Metall., 48(2), (2005):pp.139.
10. Javanbakht, M., E.Salahinejad, and M.J. Hadianfard."The effect of sintering temperature on the structure and Mechanical properties of medical-grade powder metallurgy stainless steels." Powder Technology 289(2016):pp.37-43.
11. Zhou, Xiaosheng, etal. "Microstructure characteristics and mechanical performance of Fe-Cr-Ni-Al-Ti super alloy fabricated by powder metallurgy."Journal of Alloys and Compounds918(2022):165612.
12. Souza, C.A.C., D.V. Ribeiro, and C.S. Kiminami."Corrosion resistance of Fe-Cr-based amorphous alloys:Anoverview."Journal of non-crystalline solids442(2016):pp.56-66.
13. Ahmed, Junaid, M.A.Hussein,F.Patel,andN.Al-Aqeeli."Phase evolution studies during mechanical alloying of Fe(82−x)-Cr18-Six(x=0,1,2,3) alloy."Journal of Alloys and Compounds 683(2016):pp.463-469.
14. JCPDS. PDF-2data base,Version2.1.International Center for Diffraction Data, (2002).
15. V.Mote,Y.Purushotham, B.Dole,Williamson-Hall analysis in estimation of lattice strain in nanometer-sized ZnO particles, J. The or. Appl. Phys.6(2012)6.
16. U.Patil,S.-J.Hong, C.Suryanarayana, An unusual phase transformation during mechanical alloying of a Fe-based bulk metallic glass composition, J. Alloys Compd. 389(2005):pp.121-126.
17. Kawashima, A., K. Hashimoto, and T. Masumoto. "Hydrogen embrittlement of a morphous Fe-Cr-Moalloys."Corrosion36.10(1980): pp.577-585.
18. Li,Wei,etal."The effect of Al on the 475 Cembrittlement of Fe–Cralloys." Computational materials science 74(2013):pp.101-10

NOVEL BLENDING METHODOLOGY TO PRODUCE NANO-REINFORCED FEEDSTOCK POWDERS FOR THERMAL SPRAYING

Ajaykumar Solanki[a,b], Hetal Chauhan[b], Sahil Variya[b], Daulatkumar Sharma[c], Sekar Saladi[b*]

[a]Research Scholar, Gujarat Technological University, Ahmedabad, India
[b]Sardar Vallabhbhai Patel Institute of Technology, Vasad, India
[c]Government Engineering College, Gandhinagar, India

Abstract: *Metallic, intermetallic, ceramic and cermet feedstock powders are extensively used for producing various wear, erosion, and corrosion resistant thermal spray coatings. These coatings are widely used in capital-intensive machinery such as gas turbines, aero-engines, boilers, steam turbines, incinerators etc. Recent studies have shown that addition of small quantities (1 wt. %) of different nano-reinforcements such as carbon nanotubes, graphene nanoplatelets, graphene oxide, boron nitride nano sheets, nano rare earth oxides have significantly enhanced the characteristics and performance of thermal spray coatings. Also, the uniform dispersion of nano-reinforcements is widely acknowledged to play an important role in improving coating properties. Researchers have employed various methods to prepare nano-reinforced feedstock powders, such as mechanical milling and spray drying. However, mechanical milling does not result in uniform dispersion of nano-reinforcements, and spray drying is not a cost-effective solution because powder preparation requires expensive nano size feedstock powders in addition to nano-reinforcements. Furthermore, dispersing nano-reinforcements is difficult because they agglomerate due to Van der Waals cohesive forces, which must be overcome to achieve homogeneous dispersion. As a result, effort has been taken to develop a novel blending methodology incorporates probe ultrasonication, magnetic stirring, oven drying, and 3D tumbler mixing for uniformly dispersing nano-reinforcements in conventional feedstock powders used in thermal spray processes. In the present study graphene nano platelets (GNP) and nano-ceria particles were reinforced with Cr_3C_2-NiCr feedstock powders using the blending methodology. Advanced characterization techniques viz., Raman Spectroscopy, X-ray diffraction, FE-SEM, and EDS mapping were used to identify the phases and to evaluate the homogeneity of dispersion. The results indicate that the developed blending methodology produced highly uniform nano-reinforced feedstock powders without damaging or degrading the original powders. The blending method used in this study is easy to use, cost effective and scalable to produce various combinations of nano-reinforced coating powders.*

Keywords: *Ultrasonication, Blending, 3D mixing, Nano-reinforcements, GNP, Nano-ceria*

1. Introduction

Thermal spraying is a technology which improves or restores the surface of a solid material and extends the life of new components. The process can be used to apply coatings to a wide range of materials and components, to provide resistance to: Wear, erosion, cavitation, corrosion, abrasion, or heat. In thermal spray processes, fully or partially molten coating material is sprayed on the substrate with high velocity and temperature[1]. Reclamation and re-engineering of a wide range of rotating and moving parts from machines of all kinds, including Gas turbines, Automobiles, Aerospace, Oil & gas industries, Biomedical applications, Road and rail vehicles, ships, aircraft, pumps, valves, mining and quarrying machinery, earthmovers, landing gear and virtually any equipment which is subject to wear, erosion, or corrosion[1]. This is done using either atmospheric plasma spray (APS), high velocity oxy fuel (HVOF) spray process, flame spray process, detonation gun (D-Gun) spray process, high velocity air fuel process (HVAF) and cold spray process to spray Metals & alloys

(Ni,Al, NiCrAlY), Ceramics (Al_2O_3, ZrO_2, TiO_2), Carbides & Cermets (WC-Co-Cr, Cr_3C^2-NiCr), and Polymers (polyethylene, polyamide)[1].

Many researchers have reported improvements in desired properties and behavior of these thermal spray coatings by inclusion of nano-reinforcement materials [2]. Thermal spray processes can be used to deposit nanomaterials as they are simple, have high deposition efficiency, has a wide range of coating materials and matrix, and offer ease in formation of composite coatings [2]. Nanomaterials offer benefits such as grain refinement, toughening mechanisms, and change in physical and chemical properties. However, the superior characteristics of the nanomaterials can only be tapped into the coating if they are uniformly dispersed in the coating powder. The blending of nanomaterial with thermal spray feedstock powder is a challenging task. To blend them in powder form various forms of mechanical milling are used. Some researchers have used ultrasonication of nanomaterials in suspension and then mechanical milling. Spray drying method is also widely used. There are some suspensions based thermal spray methods, in which the powder is mixed in suspension form through ultrasonication and then sprayed as coating. Mechanical milling is a traditional method for blending powders, in which the powders to be mixed are placed in a cylindrical jar and then rotated in presence of mixing medium such as balls[3]. Milling speed, ball to powder weight ratio, milling time, and process control agent are the main process parameters[4]. Ward et al[5]. used horizontal jar mixer to mix metallic powder Ni-Al with nanomaterial edge oxidized graphene oxide (EOGO) with steel balls. as mixing medium. Adding EOGO in the NiAl coating, improved hardness, adhesion strength and wear resistance by 49%, 18% and 14% respectively.

Li et al[6]. improved microstructure and wear behavior of plasma sprayed ZrO_2 coatings by reinforcing it with graphene nanosheets. They employed planetary ball milling for mixing. Wang et al [7]. and Qin et al[8]. prepared WC-Co/GO coating powders for D-gun spray with 4 methods: wet ball milling, wet mixing using a stirrer, sintering & crushing and spray drying. Liang et al[9]. reviewed physical dispersion methods (ultrasonic treatment, stirring, and ball milling) and covalent bonding methods.

Spray dried powders were reported to give the best microstructure and wear resistance. The spray drying process is used by many researchers. In this process, the nano-sized powder particles are dispersed in an organic binder to form slurry and then the slurry is passed through an atomizing orifice into a hot chamber. The droplets coming out of the orifice dry and form micron size agglomerates of coating powder[10]. Amudha et.al[11, 12]. used spray drying process to mix 0.5, 1.0, 1.5 and 2.0% graphene oxide (GO) with Al_2O_3, deposited with plasma spray process, and reported increase in microhardness and fracture toughness. Al_2O_3 powder spray dried with graphene nanoplatelets (GNP) and carbon nanotubes (CNT), and then deposited with atmospheric plasma spray process showed remarkable improvement in toughness[10], electrical conductivity[13] and tribological properties[14]. Although the spray drying approach is very promising for producing nanocomposite coating powders, it is not a cost - effective method because it requires expensive nano size feedstock powders as well as nano reinforcements for powder preparation.

Feng et al[15]. used a colloidal method to mix Al_2O_3-13%TiO_2 with graphene nanosheets (GNs). Both the constituents along with ethanol were stirred using blade agitator in ultrasonic bath

and then the blended slurry was dried in oven. They have reported 13% and 19% reduction in friction coefficient and wear rate respectively. Mukherjee et al[16]. made NiAl-GNP composite feedstock powder by first ultrasonicating GNP in acetone and then mixing the ultrasonicated GNP with NiAl powder in planetary ball mill. Plasma sprayed coating deposited with this composite powder, offered high tensile strength and good ductility.

Suspension plasma spray and suspension high velocity oxy fuel spray processes are used to deposit nanocomposite coatings. Murray et al[17]. deposited Al_2O_3 coating with 1 wt.% GNP by suspension HVOF process and exhibited enhancement in wear resistance due to improved microstructure and fracture toughness. Mahade et al[18]. used suspension plasma spay process to deposit GNP reinforced Al_2O_3 coating with water-based GNP + Al_2O_3 mixed suspension. They reported 36% lower friction coefficient and 69% lower specific wear rate. Suspension spray processes can deposit wide range of coating materials. The limitations of these processes are the complexity of the process and high capital cost.

Since the last three decades, many researchers have investigated the behavior of CeO_2 reinforced thermal spray coatings. They have reported that even small amounts of CeO_2 can significantly enhance the microstructural and mechanical characteristics of coatings, as well as increase their resistance to wear, erosion and corrosion. Also, it has been reported that the microstructure of coatings is significantly influenced by the CeO_2 particle size[19-22]. The most popular kind of reinforcement for improving the performance of Cr_3C_2-NiCr coatings is micro CeO_2. Due to improved dispersion in the coatings, nanosized CeO_2 exhibits a superior ability to refine the microstructure of the coatings as compared to micron sized CeO_2. According to the authors' knowledge, there is no literature available on the role of nano CeO_2 in enhancing the performance of Cr_3C_2-NiCr coatings. In order to homogeneously distribute nano CeO_2 with conventional feedstock powders used in thermal spray techniques, an effort has been undertaken to develop a novel blending approach.

According to Yin et al. [23], CeO_2 doped Cr_3C_2-NiCr coatings deposited by HVOF spraying is an effective technique to enhance the coating's hardness and toughness as well as increases resistance to wear, erosion, oxidation, and corrosion. By using supersonic plasma spraying, Zhang et al. [24] prepared coatings of rare earth oxide and Cr_3C_2-NiCr. The improvement of the microhardness, degree of friction, and wear resistance of Cr_3C_2-NiCr coatings was made possible by the addition of CeO_2. Most of the time, micro-CeO_2 particles are added to the Cr_3C_2-NiCr coating, which can result in an uneven distribution of cerium oxide.In comparison to micro-CeO_2, it is thought that nano-CeO_2 has a more homogenous dispersive distribution in the coating, which may help to further refine the microstructure and reduce the formation of flaws.

Jiyu Du et al.[25] examined a newly developed Cr_3C_2-NiCrCoMo/nano-CeO_2 composite coating that was applied using the HVOF procedure, the findings show that the newly developed NCE coating has improved resistant to wear at elevated temperatures with a decreased friction coefficient and wear depth.Ghadami et al. [26] prepared, characterized, and then analyzed the

oxidized behaviour of NiCrAlY coatings and (0.5-2 wt%) CeO_2 gradient NiCrAlY coating. Byincreasing the amount of nano-CeO_2, the hardness of nanocomposite coatings increased, and coating had minimum porosity content as compared to other types of conventional and nanocomposite coatings.Wang et al.[27]studied Fe-Al inter-metallic coatings by HVOF thermal spray technique. It was observed that the CeO_2 infused Fe-Al inter-metallic coatings had less porosity, fewer cracks, and improved hardness than the pure Fe-Al coatings. The Fe-Al inter-metallic coatings, which contained CeO_2, have shown enhancement in their resistance to abrasion and erosion compared to pure Fe-Al coatings.

Vishnoi et al.[28] concluded rare earth metal enhances the mechanical properties such as hardness, strength, and elastic modulus, refine microstructure and reduces porosity and cracks. Considering the beneficial mechanical and tribological effects incurred by GNP andnano CeO_2 in coatings, the authors decided to use it as reinforcement materials.

Blending of these nano-reinforcement materials uniformly in coating powders is a difficult task, owing to the difference in their densities, high surface area and high aspect ratio. Also, nano-carbonaceous materials such as graphene and carbon nanotubes tend to form bonds with each other, and form agglomerates due to van der Waals cohesive forces (London or Dispersion Forces). Atif et al. [29] and Saboori et al. [30] reported formation of agglomerates implies their nonhomogeneous dispersion in the powder matrix, which eventually may not impart the desired improvement in the properties of the coatings. The problem of this mixing issue was taken up for this study.

Bolelli et al. [31] and Matikainen et al. [32] studied HVOF sprayed Cr_3C_2-NiCr coatings as it is widely used in industries for wear and erosion resistant applications at elevated temperatures. Hence Cr_3C_2-NiCr was selected as coating powder.

2. Materials and Methods

2.1 Materials

A commercial Cr_3C_2-NiCr powder for thermal spraying (CrC-410, C&M Technologies, Germany) was used as feedstock with an average particle size 15-45 µm nominal composition of, mixed with a commercial Graphene Nanoplatelets (GNP) (Product no. 900412, Sigma Aldrich, USA) with an average particle diameter of 5 µm and surface area of 120-150 m^2/gm and 99.99% pure nano CeO_2 powders with particle size of < 25 nm for current study.

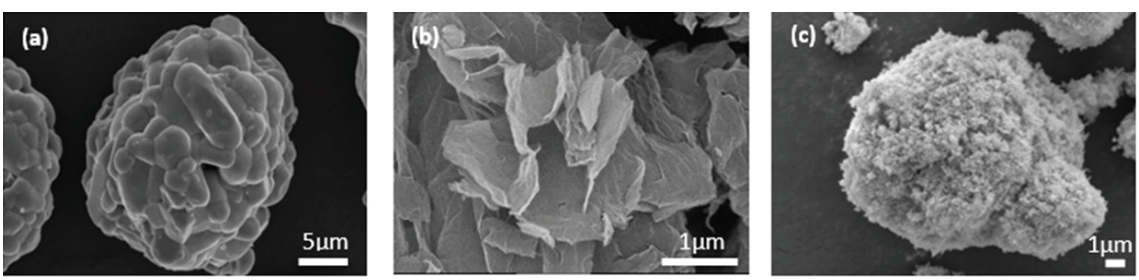

Fig. 1. FESEM micrographs of powders (a) Cr_3C_2-NiCr (b) GNP and (c) nano CeO_2

2.2 *Mixing Method*

Ultrasonication+ magnetic stirring + drying+3D tumbler mixing

Fig. 2 shows the schematic representation of the mixing method used. Ultrasonic probe sonicator (VCX500, SONICS, USA) was used to sonicate GNP and nano CeO_2 separately along with surfactant sodium dodecyl sulphate (SDS) in deionized water for 1 hour as shown in Fig. 2(a). This sonication process gives dispersed nano-suspension solution of GNP and nano CeO_2. Feedstock powder Cr_3C_2-NiCr was then added in nano-suspension solution of GNP and nano CeO_2 separately as illustrated in Fig. 2(b). after that the solutions were sonicated and simultaneously stirred with magnetic stirrer for 1 hour. The heavier Cr_3C_2-NiCr particles are kept suspended and interact more with GNP and nano CeO_2 particles due to magnetic stirring. The composite slurry was then dried in a hot air oven for 16 hours at 60°C. as shown in Fig 2(c). The dried powders are then collected in a jar. The process was carried out in batches, each batch yielding 50g of composite powder. Then the collected powders were mixed using 3D tumbler mixer, Alphie 3D, for 1 hour at 50 rpm as shown in Fig.2(d). After that the mixed powders were sieved, and the final feedstock powders were obtained. The morphology of powders Cr_3C_2-NiCr, GNP and nano CeO_2 before blending are shown in Fig. 1(a,b,c) and after blending the morphology of composite powders Cr_3C_2-NiCr + GNP and Cr_3C_2-NiCr + nano CeO2are shown in Fig.3 and Fig. 4 respectively. The novel blending methodology allows GNP and nano CeO_2 particles to uniformly disperse on the surface of Cr_3C_2-NiCr particles and enter the pores of powder particles.

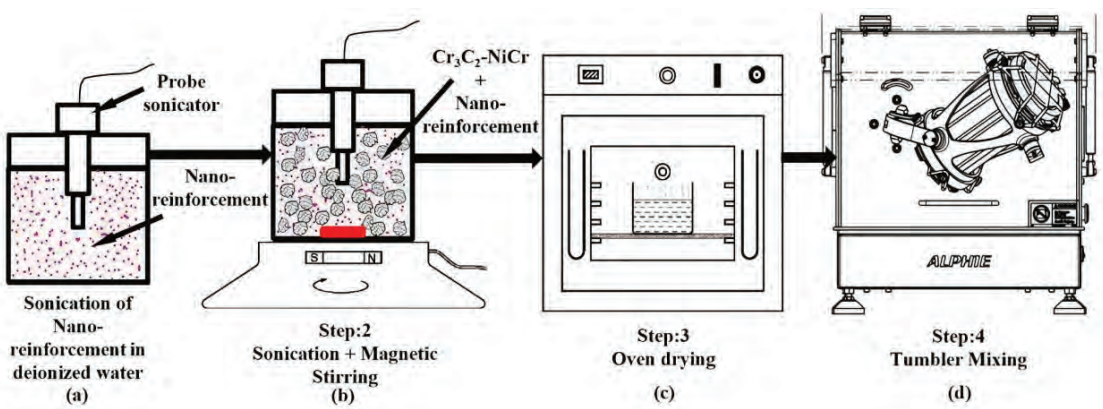

Fig.2. Mixing process of Cr_3C_2-NiCr, GNP and CeO_2 involving sonication, magnetic stirring, drying& 3D tumbler mixing

2.3 *Characterization Methods*

FE-SEM with JEOL in-lens Schottky field emissions source (JEOL 7900F, USA) equipped with an energy-dispersive x-ray (EDX) detector (Oxford Instruments, UK) was used to examine themixed powder. For phase identification, the powder samples were analyzed by X-ray diffraction (XRD) using a Bruker AXS D-8 Advance diffractometer with Cu Ka radiation. Raman Spectroscopy of the powder was carried out by Renishaw In via Raman Microscope

(Qontor with wavelength of 532 nm at 0.3 mW power) to prove the presence of GNP and nano CeO_2.

3. Results and Discussion

3.1 FE-SEM analysis and EDS mapping of powder

The FE-SEM micrographs and EDS mapping of feedstock powder Cr_3C_2-NiCr along with GNPare shown in Fig. 3 (a-g). It is evident that the particle morphology of Cr_3C_2-NiCr powder is uneven, porous, and spheroidal in shape, while the Cr_3C_2 particles are cladded to each other through the NiCr metallic binder phase. Further, the blending process did not cause any visible damage to Cr_3C_2-NiCr powders. The dispersion of GNP is homogeneous on to the surface of Cr_3C_2-NiCr powder particles. It is evident that the novel blending methodology used in the present investigation was able to disperse GNP to the interior portions of the pores present in Cr_3C_2-NiCr powder particles. The stuffing ameliorates GNP distribution in the coatings and increases GNP retention by encapsulating it in the pores and protecting it from getting blown away during high velocity spraying process. The superior dispersion of GNP can mainly be attributed to sonication (using probe sonicator) and magnetic stirring stages Fig. 2 (a&b).

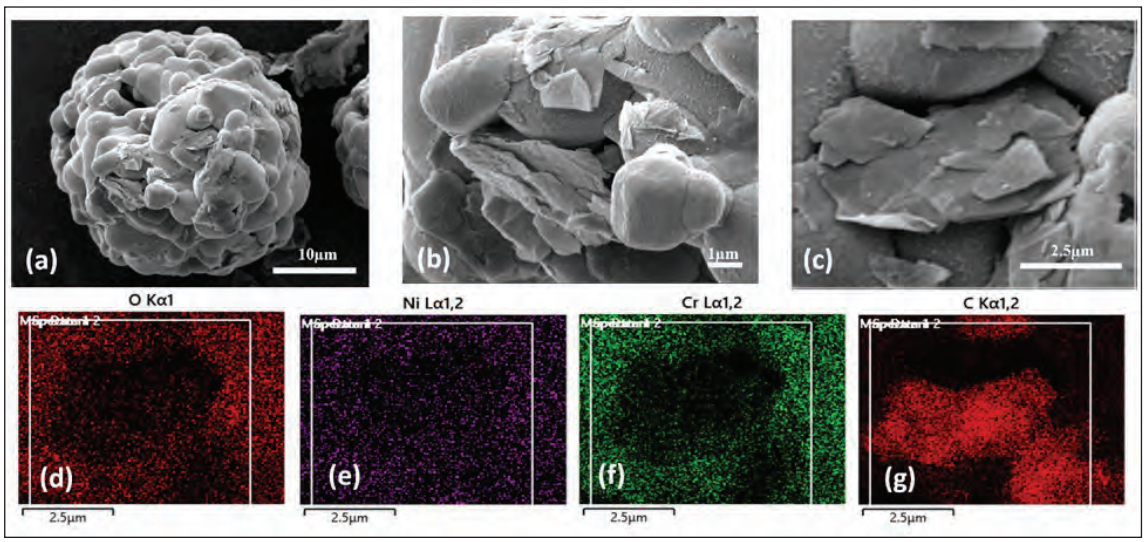

Fig. 3. FESEM micrographs and EDS mapping of blended powder Cr_3C_2-NiCr + GNP

The FE-SEM micrographs and EDS mapping of feedstock powder Cr_3C_2-NiCr along with nano CeO_2 are shown in Fig. 4(a-h). Due to particle morphology of Cr_3C_2-NiCr powder the homogeneity of dispersion is superior in the case of nano CeO_2. The nano CeO_2 particles are clinging on to the surface of Cr_3C_2-NiCr powder particles. Fig. 4(b) shows that some of the pores of Cr_3C_2-NiCr are stuffed with nano CeO_2 particles. It is evident that the novel blending methodology used in the present investigation was able to disperse nano CeO_2 to the interior portions of the pores present in Cr_3C_2-NiCr powder particles. The stuffing strengthens CeO_2 distribution and retention in coatings by enclosing it in the pores and protecting it from

being blown away during the high velocity spraying process. The superior dispersion of nano CeO_2 can mainly be attributed to sonication (using probe sonicator) and magnetic stirring stages Fig. 2 (a & b). It must be noted that the probe sonicator used in this study has superior dispersion capabilities. Therefore, the novel blending method used in this study was effective in breaking the nano particle agglomerates by overcoming Vander Walls cohesive forces and keep them dispersed throughout the powder preparation process. This method is simple, scalable and can be effectively used to produce nano-enabled thermal spray feedstock powders.

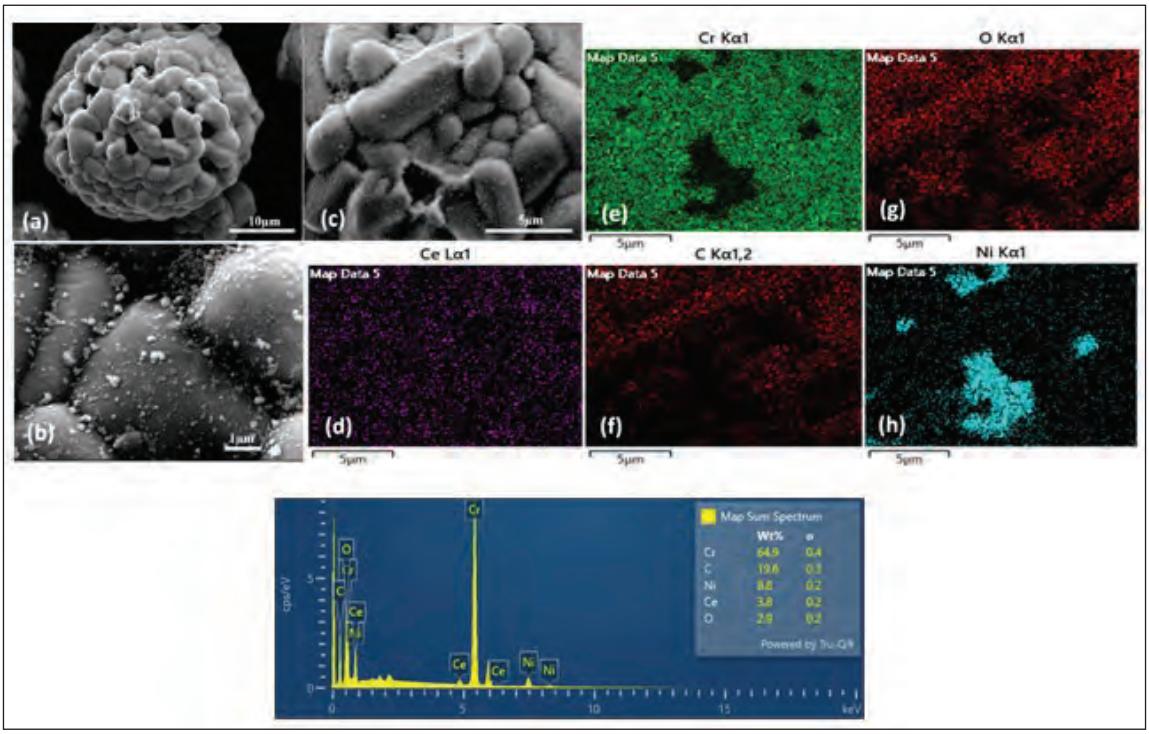

Fig. 4. FESEM micrographs and EDS mapping of blended powder Cr_3C_2-NiCr + nano CeO_2

3.2 XRD analysis of powder

TheXRD patterns of powders Cr_3C_2-NiCr, Cr_3C_2-NiCr+GNP and Cr_3C_2-NiCr+ nano CeO_2 are shown in Fig.5. Before blending two phases were identified carbide phase Cr_3C_2 and matrix phase NiCr. After blending feedstock powder Cr_3C_2-NiCr with GNP and nano CeO_2, once again XRD analysis was carried out. The presence of Cr_3C_2 and NiCr remain intact, also the presence of CeO_2 phase was identified in nano CeO_2 doped feedstock powder.It is evident that after the blending process, there are no undue phase changes in powders.

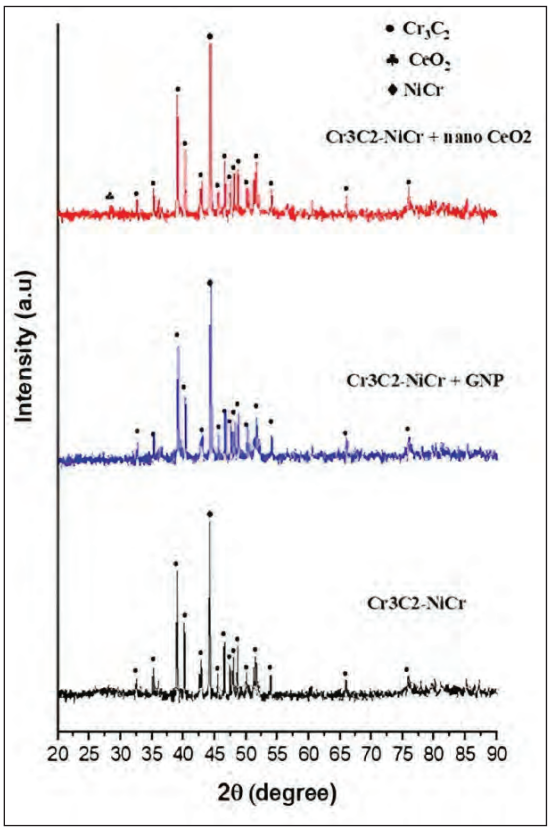

Fig. 5. XRD diffraction pattern of Cr_3C_2-NiCr, Cr_3C_2-NiCr + GNP and Cr_3C_2-NiCr + nano CeO_2 powders

3.3 Raman Spectroscopy of powder

Raman spectroscopy is an analytical tool to prove the presence of carbonaceous materials. Raman spectroscopy of GNP powder shows the typical graphene peaks at 1350 cm^{-1}, 1580 cm-1, and 2700 cm^{-1} corresponding to D-band, G-bad and 2D -band respectively [33]. The coating powder Cr_3C_2-NiCr+GNP blended with sonication, magnetic stirring, oven drying & 3D tumbler mixing shows the identical peaks in Fig. 6. This indicates that the powder mixing process has retained the graphene without significant structural damage. Also, in Fig. 6 Raman spectroscopy of nano CeO_2 powder shows the typical peak at 460 cm-1 corresponding to D-band which is identical peak to coating powder Cr_3C_2-NiCr + nano CeO_2 blended with sonication, magnetic stirring, oven drying and 3D tumbler mixing.

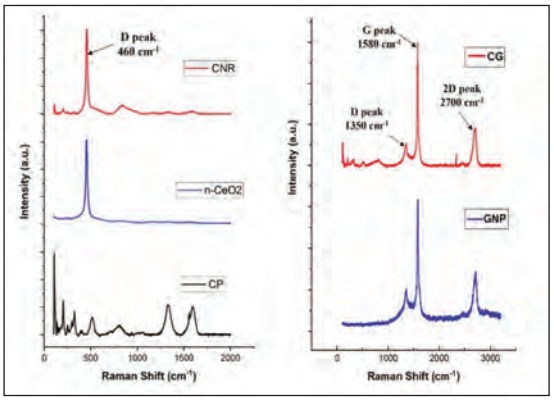

Fig. 6. Raman spectroscopy of powders (a) comparison of Cr_3C_2-NiCr, nano CeO_2 and nano reinforced feedstock powder (b) comparison of GNP and GNP reinforced feedstock powder

Conclusion

From this study authors found an appropriate method for blending cermet coating powder Cr_3C_2-NiCr with nano-carbonaceous material GNP and rare earth element CeO_2. Following conclusion can be drawn from it:

- Ultrasonication followed by magnetic stirring, drying and 3D tumbler mixing, gave coating powder with most uniformly dispersed GNP and CeO_2 which was established by FE-SEM analysis and EDS mapping.
- XRD analysis proved that no phase change of the feedstock powder occurred because of blending process hence structural integrity of the powder was maintained.
- Raman spectroscopy of GNP powder shows the typical graphene peaks at 1350 cm-1, 1580 cm-1, and 2700 cm-1 corresponding to

D-band, G-bad and 2D-band respectively. Hence proved the presence of nano carbonaceous material. Raman spectroscopy of nano CeO_2 powder shows the typical peak at 460 cm-1 corresponding to ceria. Both had identical peaks with blended powders.

Acknowledgements

The authors would like to thank ABS Fujitsu General Pvt. Ltd., Bengaluru for providing financial assistance under their CSR policy. The authors are also thankful to Mr. Jigar Talati, Hexagonal Product Development, Pvt. Ltd., Por, Gujarat for providing Alphie 3D-tumbler mixer.

References

1. B. Mellor, J. M. Guilemany, and J.Nin, "Surface Coatings for Protection Against Wear.Chapter: "Thermal Spraying Methods for Protection Against Wear"," 2006, pp. 249-301.
2. Y. Gu, K. Xia, D. Wu, J. Mou, and S. Zheng, "Technical Characteristics and Wear-Resistant Mechanism of Nano Coatings: A Review," *Coatings*, vol. 10, no. 3. doi: 10.3390/coatings10030233
3. D. L. Zhang, "Processing of advanced materials using high-energy mechanical milling," *Progress in Materials Science,* vol. 49, no. 3, pp. 537-560, 2004/01/01/ 2004.
4. A. Canakci, F. Erdemir, T. Varol, and A. Patir, "Determining the effect of process parameters on particle size in mechanical milling using the Taguchi method: Measurement and analysis," *Measurement,* vol. 46, no. 9, pp. 3532-3540, 2013/11/01/ 2013.
5. D. Ward et al., "Functional NiAl-graphene oxide composite as a model coating for aerospace component repair," *Carbon,* vol. 105, pp. 529-543, 2016/08/01/ 2016.
6. H. Li et al., "Microstructure and wear behavior of graphene nanosheets-reinforced zirconia coating," *Ceramics International*, vol. 40, no. 8, Part B, pp. 12821-12829, 2014/09/01/ 2014.
7. X. Wang, H. Tian, C. Wang, M. Guo, S. Wei, and B. Xu, "Properties of GO/WC–Co coatings prepared via different pulverisation processes," *Surface Engineering,* vol. 35, no. 11, pp. 933-946, 2019/11/02 2019.
8. Z. Shu ai, G. Xiao feng, Y. Ren ping, X. Qin, X. Ling ping, and W. Zhong xun, "Self-lubrication and wear-resistance mechanism of graphene-modified coatings," *Ceramics International*, vol. 46, no. 10, Part B, pp. 15915-15924, 2020/07/01/ 2020.
9. A. Liang, X. Jiang, X. Hong, Y. Jiang, Z. Shao, and D. Zhu, "Recent Developments Concerning the Dispersion Methods and Mechanisms of Graphene," *Coatings,* vol. 8, no. 1. doi: 10.3390/coatings8010033
10. B. Mukherjee, O. S. Asiq Rahman, A. Islam, M. Sribalaji, and A. K. Keshri, "Plasma sprayed carbon nanotube and graphene nanoplatelets reinforced alumina hybrid composite coating with outstanding toughness," *Journal of Alloys and Compounds,* vol. 727, pp. 658-670, 2017/12/15/ 2017.
11. A. Amudha, H. D. Shashikala, O. S. Asiq Rahman, A. K. Keshri, and H. S. Nagaraja, "Effect of graphene oxide loading on plasma sprayed alumina-graphene oxide composites for improved anticorrosive and hydrophobic surface," *Surface Topography: Metrology and Properties,* vol. 7, no. 2, p. 024003, 2019/06/14 2019.
12. A. Amudha, H. S. Nagaraja, and H. D. Shashikala, "Plasma-sprayed graphene oxide reinforced alumina composite coatings on low carbon steel with improved fracture toughness, brittleness index, and microhardness," *Materials Today: Proceedings*, vol. 39, pp. 1503-1508, 2021/01/01/ 2021.
13. A. Islam et al., "Role of Hybrid Reinforcement of Carbon Nanotubes and Graphene Nanoplatelets on the Electrical Conductivity of Plasma Sprayed Alumina Coating," *Ceramics International,* vol. 44, 12/05 2017.
14. S. Priyadershini, O. S. A. Rahman, K. K. Pandey, and A. K. Keshri, "Remarkable improvement in tribological behavior of plasma sprayed carbon nanotube and graphene nanoplatelates hybrid reinforced alumina nanocomposite coating," *Ceramics International,* vol. 45, no. 5, pp. 5768-5778, 2019/04/01/ 2019.
15. Y. Feng, J. Fang, J. Wu, K. Gu, and P. Liu, "Mechanical and tribological properties of plasma sprayed graphene nanosheets/Al2O3+13 wt%TiO2 composite coating," *Tribology International,* vol. 146, p. 106233, 2020/06/01/ 2020.

16. B. Mukherjee, R. Kumar, A. Islam, O. S. A. Rahman, and A. K. Keshri, "Evaluation of strength-ductility combination by in-situ tensile testing of graphene nano platelets reinforced shroud plasma sprayed Nickel-Aluminium coating," *Journal of Alloys and Compounds,* vol. 765, pp. 1082-1089, 2018/10/15/ 2018.

17. J. W. Murray, G. A. Rance, F. Xu, and T. Hussain, "Alumina-graphene nanocomposite coatings fabricated by suspension high velocity oxy-fuel thermal spraying for ultra-low-wear," *Journal of the European Ceramic Society,* vol. 38, no. 4, pp. 1819-1828, 2018/04/01/ 2018.

18. S. Mahade, A. Mulone, S. Björklund, U. Klement, and S. Joshi, "Incorporation of graphene nano platelets in suspension plasma sprayed alumina coatings for improved tribological properties," *Applied Surface Science,* vol. 570, p. 151227, 2021/12/30/ 2021.

19. F. Ghadami, A. Sabour Rouh Aghdam, A. Zakeri, B. Saeedi, and P. Tahvili, "Synergistic effect of CeO2 and Al_2O_3 nanoparticle dispersion on the oxidation behavior of MCrAlY coatings deposited by HVOF," *Ceramics International,* vol. 46, no. 4, pp. 4556-4567, 2020/03/01/ 2020.

20. A. Zakeri, E. Bahmani, A. Sabour Rouh Aghdam, B. Saeedi, and M. Bai, "A study on the effect of nano-CeO_2 dispersion on the characteristics of thermally-grown oxide (TGO) formed on NiCoCrAlY powders and coatings during isothermal oxidation," *Journal of Alloys and Compounds,* vol. 835, p. 155319, 2020/09/15/ 2020.

21. X. Sun, S. Chen, Y. Wang, Z. Pan, and L. Wang, "Mechanical Properties and Thermal Shock Resistance of HVOF Sprayed NiCrAlY Coatings Without and With Nano Ceria," *Journal of Thermal Spray Technology,* vol. 21, no. 5, pp. 818-824, 2012/09/01 2012.

22. J. Liu, T. Chen, H. Duan, C. Yuan, and X. Bai, "Mechanical Properties and Cavitation Erosion Behavior of CeO_2-Modified Dual-scale WC-10Co-4Cr Coating Prepared by HVOF," *Journal of Thermal Spray Technology,* vol. 31, no. 8, pp. 2463-2475, 2022/12/01 2022.

23. B. Yin, G. Liu, H. Zhou, J. Chen, and F. Yan, "Sliding Wear Behavior of HVOF-sprayed Cr_3C_2–NiCr/CeO_2 Composite Coatings at Elevated Temperature up to 800 °C," *Tribology Letters*, vol. 37, no. 2, pp. 463-475, 2010/02/01 2010.

24. Z. Zhang, X. Lu, and J. Luo, "Tribological properties of rare earth oxide added Cr_3C_2–NiCr coatings," *Applied Surface Science,* vol. 253, no. 9, pp. 4377-4385, 2007/02/28/ 2007.

25. J. Du et al., "The influence of nano-CeO2 on tribological properties and microstructure evolution of Cr_3C_2-NiCrCoMo composite coatings at high temperature," *Surface and Coatings Technology*, vol. 428, p. 127913, 2021/12/25/ 2021.

26. F. Ghadami, A. Zakeri, A. S. R. Aghdam, and R. Tahmasebi, "Structural characteristics and high-temperature oxidation behavior of HVOF sprayed nano-CeO_2 reinforced NiCoCrAlY nanocomposite coatings," *Surface and Coatings Technology*, vol. 373, pp. 7-16, 2019/09/15/ 2019.

27. Y. Wang and M. Yan, "The effect of CeO_2 on the erosion and abrasive wear of thermal sprayed FeAl intermetallic alloy coatings," *Wear*, vol. 261, no. 11, pp. 1201-1207, 2006/12/20/ 2006.

28. M. Vishnoi, Q. Murtaza, and P. Kumar, "Effect of rare earth elements on coatings developed by thermal spraying processes (TSP) – A brief review," *Materials Today: Proceedings,* vol. 44, pp. 4053-4058, 2021/01/01/ 2021.

29. R. Atif and F. Inam, "Reasons and remedies for the agglomeration of multilayered graphene and carbon nanotubes in polymers," *Beilstein Journal of Nanotechnology*, vol. 7, pp. 1174-1196, 2016.

30. A. Saboori, S. K. Moheimani, M. Dadkhah, M. Pavese, C. Badini, and P. Fino, "An Overview of Key Challenges in the Fabrication of Metal Matrix Nanocomposites Reinforced by Graphene Nanoplatelets," *Metals*, vol. 8, no. 3. doi: 10.3390/met8030172

31. G. Bolelli et al., "Sliding and abrasive wear behaviour of HVOF- and HVAF-sprayed Cr_3C_2–NiCr hardmetal coatings," *Wear,* vol. 358-359, pp. 32-50, 2016/07/15/ 2016.

32. V. Matikainen, G. Bolelli, H. Koivuluoto, P. Sassatelli, L. Lusvarghi, and P. Vuoristo, "Sliding wear behaviour of HVOF and HVAF sprayed Cr_3C_2-based coatings," *Wear*, vol. 388-389, pp. 57-71, 2017/10/15/ 2017.

33. I. Childres, L. Jauregui, W. Park, H. Caoa, and Y. P. Chena, "Raman Spectroscopy of Graphene and Related Materials," *New Developments in Photon and Materials Research*, pp. 403-418, 01/01 2013.

MECHANICAL ALLOYING OF EQUIATOMIC CoCrFeMnNi HIGH ENTROPY ALLOY

Pardhasaradhi DVT[1*], Subrahmanyam S[1], RVS Pranav[1] and Sunil Kumar R[1]

[1]Department of Metallurgical & Materials Engineering, NIT Andhra Pradesh, India.

Abstract: *High-entropy alloys (HEAs) have emerged as one of the most promising research areas recently. This paper discusses the phase evolution and micro structural changes of mechanically milled powders with respective to time of milling and speed. Equivalent CoCrFeMnNi high entropy alloy is produced through mechanical milling of the individual powders in a planetary ball mill at 300 rpm maintaining ball to powder ratio as 10:1. A homogeneous distribution of the powders was achieved. Micro structural studies were carried out to assess particle size and phase transformation as well as to optimise the ball mill process parameters samples with the samples drawn at successive intervals of 15 m, 1 h, 2 h, 4 h, 6 h, 8 h, 10 h, and 12 h. Optical microscopy was used to investigate particle morphology and chemical homogeneity.*

Keywords: *CoCrFeMnNi; High entropy alloys; Solid solution; Crystallite Size; Lattice Strain;*

1. Introduction

HEAs are still a relatively new and rapidly evolving field of study, and their potential applications and limitations are still being explored. Traditional alloys typically consist of one or two dominant constituents and other elements in smaller quantities to enhance specific properties. On the other hand, HEAs have multiple principal elements, which results in a highly disordered atomic structure and a high degree of configurational entropy [1-4].

HEAs were first introduced in 2004 by J.W. Yeh and his colleagues, and since then, they have developed a lot of thrust due to their unique properties [1]. HEAs have been shown to exhibit excellent mechanical, thermal, and chemical properties, as well as high corrosion resistance and low-temperature embrittlement[5,6]. However, their unique properties make them a contender in many fields such as aerospace, energy, and biomedical engineering [7]. One of the key advantages of HEAs is their ability to maintain their properties even at high temperatures, as they suit better for high-temperature applications [8, 9]. Additionally, the high degree of configurational entropy in HEAs provides a broad range of solid solution phases, which can allow researchers to develop new alloys with tailored properties.

Mechanical alloying is a process that can be used to create high-entropy alloys. This can result in several outcomes, depending on the materials being processed, the milling conditions, and the desired properties of the resulting alloys with Homogenization of the alloy, Reduction in particle size, Formation of new phases, improved chemical reactivity and production of fine grained materials [11]. The purpose of the work is to optimize the milling parameters of CoCrFeMnNi HEAs for high temperature applicatios.

2. Materials & Experimental Procedure

The high entropy alloy employed in this study is CoCrFeMnNi.In order to fabricate the CoCrFeMnNi High-Entropy Alloy (HEA), the individual elements specified in Table 1 were selected and combined in suitable proportions. The CoCrFeMnNi HEA was prepared using an equiatomic composition, ensuring that each

element was present in equal amounts. These weighed powders were first mixed manually and then milled using a planetary ball mill (PM100, RETSCH, Germany) maintaining the powder to ball ratio as 1:10 for 12 hours with a speed of 300 rpm. The balls used were made of tungsten carbide. Micro structural characterization was carried out on the samples drawn at successive time intervals of 15 m, 1 h, 2 h, 4 h, 6 h, 8 h, 10 h and 12 h to optimize the milling parameters of the alloy. XRD patterns were analyzed using X'Pert-Pro (PANalytical) to study the crystalline structure of the powder samples. Mechanically alloyed powder for 12 hours was used to consolidate the pellets using a hydraulic press applying load of 500 and 650 MPa for a dwell time of 5 mins. The pellets were then sintered using a tubular furnace for an hour at 900°C in the presence of Argon atmosphere. Furnace cooled sintered specimens have been grounded and polished using emery papers and further polished using diamond polishing up to 0.035µm. Optical microscopy was used to study the microstructure.

Table 1: Specifications of elemental metal powders

Elements	Particle size (microns)	Purity (%)
Cobalt	45-50µm	99.99
Chromium powder	45-50µm	99
Iron powder	45-50µm	99.9
Manganese	45-50µm	99.99
Nickel	45-50µm	99.99

3. Results and Discussion

3.1 Phase analysis of CoCrFeMnNi HEAs

Fig.1. presents the X-ray diffraction pattern of CoCrFeMnNi HEA powders with respective milling time. Peaks confirm that all the elements used are present after 15 min of milling time. Careful analysis of the XRD patterns of samples drawn from 1 h to 4 hr of milling time reveals that the intensity of the XRD pattern is decreased but peak position remained constant. It is observed that there is a decrement in intensity and change in peak position as well after 6 hr milling time. According to the literature, it has been observed that the decrement in intensity confirms the formation of a solid solution. Additionally, the change in peak position indicates the formation of intermetallics after 6 hours of milling time, suggesting the possible formation of MnNi3 and FeNi phases [10].

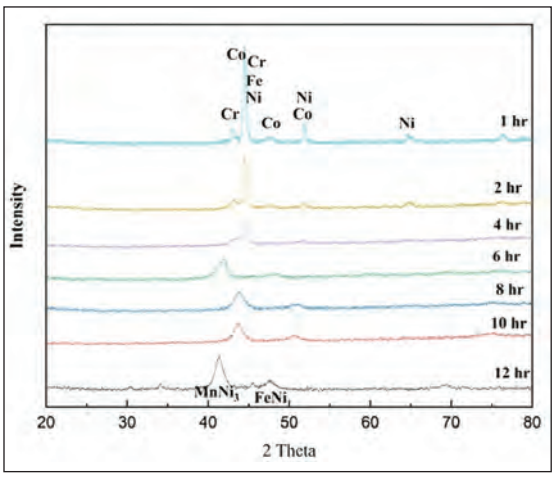

Fig.1. XRD patterns of CoCrFeMnNi HEA powders with respective to milling time;

Figure 2 and 3 represents the change in behavior of crystallite size and lattice strain of CoCrFeMnNi HEAs powders respectively. Particle size and crystallite strain calculations were done using Scherrer equation [14]. According to the literature, it is suggested that the behavior of crystallite size and lattice strain in CoCrFeMnNi HEAs powders would exhibit changes, and there is evidence to support this claim.It is observed that the Crystallite size of the powders after milling is decreased with the increase in milling time. The increment in

the crystalline strain is noticed and reported [11]. This results in solid solution hardening. Mechanical deformation during milling is also responsible for the increased crystallite strain [12, 13].

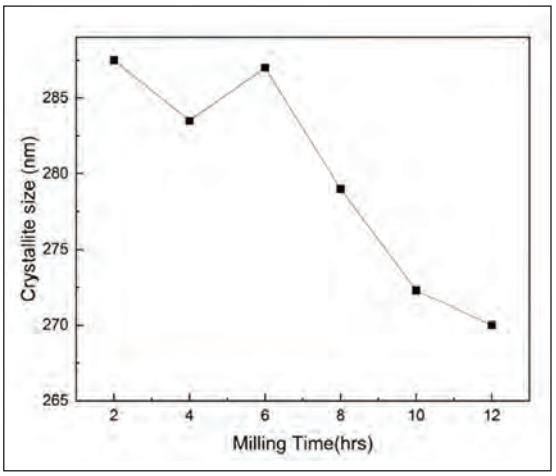

Fig 2. Variation in crystallite size of CoCrFeMnNi HEA

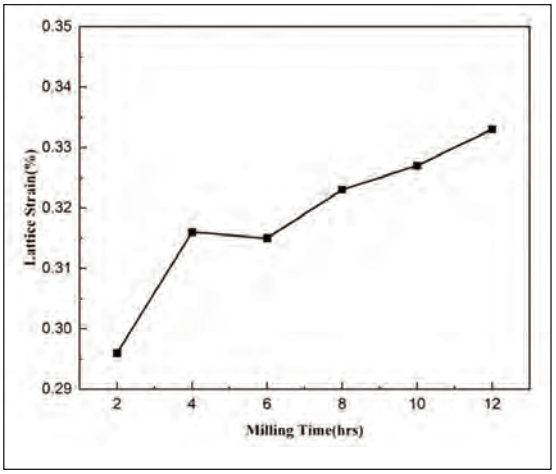

Fig 2. Variation in crystallite size of CoCrFeMnNi HEA

3.2 Micro structural evolution of CoCrFeMnNi HEAs

Fig.4 shows the micrographs of the CoCrFeMnNi alloys investigated by Optical microscopy at 100X. It is observed that the micrographs contain pores in it, which can be attributed to the process route followed by sintering. It was also observed that there is no significant change in the phases of the alloys with respective to the load applied. Based on the micrograph analysis, it can be observed that the alloys consist of multiple phases. Further analysis is needed to obtain detailed information about these phases.

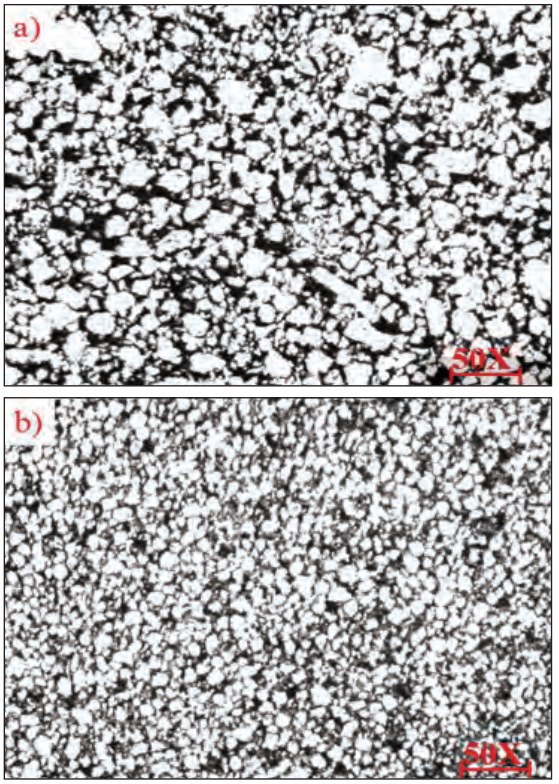

Fig. 4. Shows the optical Micrographs of the sintered pellets of CoCrFeMnNi alloys a) processed with 500 MPa load and b) processed with 650 MPa load at 100 X

3.3 Microhardness of sintered CoCrFeMnNi HEAs

The hardness values of the sintered CoCrFeMnNi HEAs are plotted and displayed in Fig.5. It is observed that the hardness values of the alloys vary with the compaction load. There is a change in hardness value of each instance of the sample with a variance of +/- 25 HV. However, average of 5 hardness values have been calculated and reported.

The hardness of the CoCrFeMnNi HEAs processed with 500 MPa shows the higher values than the HEAs processed with 650 MPa, which is attributed to the development of localized lattice Strain.

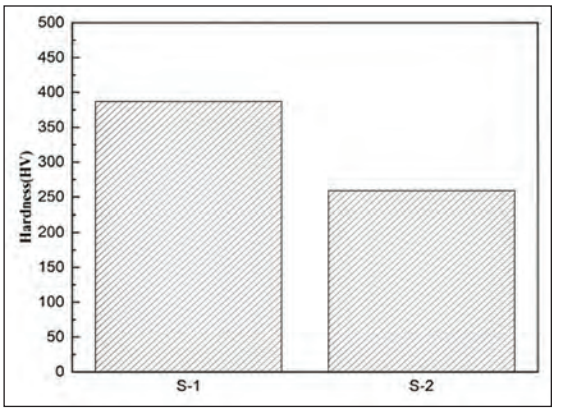

Fig.5. Hardness results of the studied CoCrFeMnNi HEAs

4. Conclusions

The micro structural and the hardness behavior of CoCrFeMnNi HEA samples prepared through conventional method were investigated and concluded the following:

- CoCrFeMnNi HEAs were successfully prepared through mechanical alloying for 12 hours followed by sintering at 900°C in the presence of Ar atmosphere for 1 hour.
- X-ray diffraction of mixed powders revealed the evolution of solid solution in HEA.
- Micro structural analysis revealed that the microstructure contains two FCC solid solution phases in it.
- Sintered HEAs processed with 500 MPa compaction load have shown greater hardness values.

Acknowledgments

The authors are thankful and acknowledge the support provided by all the working staff of the Department of Metallurgical & Materials Engineering, NIT Andhra Pradesh to carry out this work.

References

1. W. Yeh, Y. L. Chen, S. J. Lin, and S. K. Chen., "Nanostructured High-Entropy Alloys with Multiple Principal Elements: Novel Alloy Design Concepts and Outcomes," Adv. Eng. Mater., vol. 6, no. 5, pp. 299–303, 2004.
2. J. W. Yeh, Y. L. Chen, S. J. Lin, and S. K. Chen, "High-Entropy Alloys – A New Era of Exploitation," Materials Science Forum, vol. 560, pp. 1–9, 2007.
3. J. W. Yeh., "Alloy Design Strategies and Future Trends in High-Entropy Alloys"Journal of Materials, 2013. 65(12): p. 1759-1771. 30.
4. Yong Zhang, Ting Ting Zuo, ZhiTang, Michael C.Gao, Karin A.Dahmen, Peter K.Liaw and Zhao Ping Lu, "Nanostructured high-entropy alloys with multiple principal elements: Novel alloy design concepts and outcomes" Advanced Engineering Materials, 2004. 6(5): p. 299-303. 8.
5. B.CantorI.T.H.ChangP.Knight and A.J.B.Vincent, "Microstructural development in equiatomic multicomponent alloys" Materials Science and Engineering A, 375-377: p. 213-218, 2004.
6. Gali, A. and E.P. George, "Tensile properties of high- and medium-entropy alloys" Intermetallics, 2013. 39(0): p. 74-78.
7. S. Ranganathan, Alloyed pleasures: multimetallic cocktails, Curr Sci India 85(10) (2003) 1404- 1406.
8. B.S. Murty, J.-W. Yeh, S. Ranganathan, P. Bhattacharjee, High-entropy alloys, Elsevier 2019.

9. Yong Zhang, Novel microstructure and properties of multicomponent CoCrCuFeNiTi x alloys". lntermetallics, 2007. 15(3): p. 357-362.
10. B. Ren, Z.X. Liu *, D.M. Li, L. Shi, B. Cai, M.X. Wang, "Effect of elemental interaction on microstructure of CuCrFeNiMn high entropy alloy system" Journal of Alloys and Compounds 493 (2010) 148–153.
11. A. Kumar, P. Dhekne, A. Kumar, M. Kumar, "Analysis of Si addition on phase formation in AlCoCrCuFeNiSix high entropy alloys," Mater. Lett., vol. 188, pp. 73-76, 2017.
12. H.X. Sui, M. Zhu, M. Qi, G.B. Li, D.Z. Yang, "The enhancement of solid solubility limits of AlCo intermetallic compound by high-energy ball grinding," J. Appl. Phys., vol. 71, pp. 2945–2949, 1992.
13. Z. Fu, W. Chen, H. Xiao, L. Zhou, D. Zhu, S. Yang, "Fabrication and properties of nanocrystalline Co0.5FeNiCrTi0.5 high entropy alloy by MA-SPS technique," Mater. Des., vol. 44, pp. 535–539, 2013.
14. A. Kumar, A.K. Swarnakar, M. Chopkar, "Phase Evolution and Mechanical Properties of AlCoCrFeNiSi x High-Entropy Alloys Synthesized by Mechanical Alloying and Spark Plasma Sintering," J. Mater. Eng. Perform, vol. 27, pp. 3304–3314, 2018.

IMPACT OF SINTERING ON METAL - ORGANIC FRAMEWORKS: A REVIEW

Vaibhav Raibole[1], Krishnamurthy Goggi[1], Rayappa Shrinivas Mahale[1*,2], Prashant Kakkamari[3]

[1]Department of Mechanical Engineering, Jain College of Engineering and Research, Belagavi, Karnataka, India.

[2]School of Mechanical Engineering, REVA University, Bengaluru, Karnataka, India.

[3]Department of Mechanical Engineering, KLS Gogte Institute of Technology, Belagavi, Karnataka, India.

Abstract: *This study includes Metal-Organic Frameworks (MOFs) which are a type of porous materials that have advanced significantly in recent years. Due to their porous structure, they outperform traditional adsorbents in hot areas like carbon dioxide collection and dihydrogen and methane storage. Because of this, MOFs' shape presents a unique challenge compared to other conventional porous materials. Metal-organic frameworks (MOFs) have shown potential in a wide range of applications, including molecular sieving, energy storage, ion separation, and biomedicine. The production of coherent material masses is accomplished through sintering, which can occur both naturally in mineral deposits and artificially when processing metal, ceramic, and plastic materials. Sintering is a well-known and commercially available method that can be scaled up for industrial use. Pressure-assisted sintering was used to quickly create crystalline macro-porous monoliths from metal-organic framework (MOF) powders. They produce microcrystalline powders with sorption capabilities, which have been praised for their potential in massive industrial separation processes. Taking into existence the behaviour and mechanism of coordination polymer and metal-organic frameworks, consider Zn $(HPO_4)(HPO_4)_2$. $2H_2$ Imidazole (ZPI: a melting coordination polymer, (Im) imidazole) and ZIF-8 were studied. Simple compaction and subsequent sintering allowed for the creation of a bulk body of coordination polymers without sacrificing the macroscopic crystallinity. The temperature, heating rate, and physical characteristics of the coordination polymers were found to be determinants of their reliability. Both coordination polymers shrunk between 10 and 20%, while the ZPI shrunk by less than 1%. Through this study, we can understandthe thermal, mechanical, chemical, and physical properties of the sintered metal-organic frameworks.*

Keywords: *Sintering,Metal-Organic Frameworks, Coordination Polymer, Thermoluminescence, Nanoprobe Technology;*

1 Introduction

The most prevalent molding technique is the direct sintering of crystalline powder, however, only a limited amount of research has focused on the study of Crystal Powders (CPs) in their post-compaction powder state [1-5]. Melting and non-melting CPs, such as ZIF-8 and [Zn $(HPO_4)(H2PO_4)_2$] $2H_2$Im, are used in this studyand the differences between these two are studied [5-7]. MOFs were initially used as adsorbents due to their large surface area and low density [7-10]. They outperform the majority of benchmark adsorbents in gas adsorption and can change structurally by in situ or post-synthesis procedures. This allows them to be used in a range of applications, such as catalysis, drug delivery, sensing, water purification, energy storage, and more [11-13].

The research reported on the hot pressing of ZIF-4 and documented the thermal transition characteristics of various MOFs. Based on the melting point of the materials, the optimal

sintering temperature for metals and ceramics was determined [13-17]. Widmer et al. studied on hot-press approach and how the CPs behave when sintered from their powder condition following compaction.Melting and non-melting CPs, such as ZIF-8 and [Zn(HPO4)$(H_2PO_4)_2]2H_2$Im, are used in this study [17-18]. MOFs are commonly offered as powders, and their crystal sizes typically range from tens of nanometres to a few microns. Individual crystals in MOFs are commonly produced as polycrystalline powders and range in size from a few tens of nanometres to a few microns.

Powders pose several processing difficulties, making them unsuitable for use in big industrial reactors. To solve these issues, MOF powders should be produced into packed objects with certain shapes and sizes. The shape is the process of compacting individual crystallites into millimetre-scale structures, which can be used to create easily handled products for industrial processes [19-23].

The study is focused on the importance of making mechanically stable powder-based products that can withstand a variety of processing circumstances, removing mass transport constraints, and maintaining the physicochemical properties of pure powder [24-29]. MOFs are particularly vulnerable to losses in surface area and pore volume due to the formation process, and shaping techniques enable the molding of powders into shaped entities for application in different types of reactors.

Porous metals are highly desirable materials for various applications due to their unique combination of physical and mechanical properties. Their ability to absorb energy, dampen vibrations and reduce noise, their robustness at high temperatures along with excellent thermal conductivity, and their ability to be integrated into strong, stiff, and lightweight structures make them particularly attractive [30-33]. One example of this is the use of Al foams as fillers in sandwich panels.

2 Overview of Sintering Process

2.1 Hot Pressing

Vacuum sintering was used to create pellets with a 10 mm diameter, as zeolitic imidazolate frameworks (ZIFs) undergo a phase shift from a solid to a liquid upon heating. MOF melting and sintering are unknown processes, but the P-T curve for the crystalline ZIF-62 material demonstrates how the sintering process may change phase-transition behaviours, with higher pressure leading to melting and amorphization at lower temperatures [34-39]. The earliestporous metals were loose packs, pressure loss, or gravity-sintered metal powders, which are still used as filters and self-lubricating bearings. These systems have lower porosities than the majority of porous metals, with packing densities in the range of 40-60%. Only the capacity to sinter the metal in the right die can restrict the variety of metals in which porosity may be included [40-42].

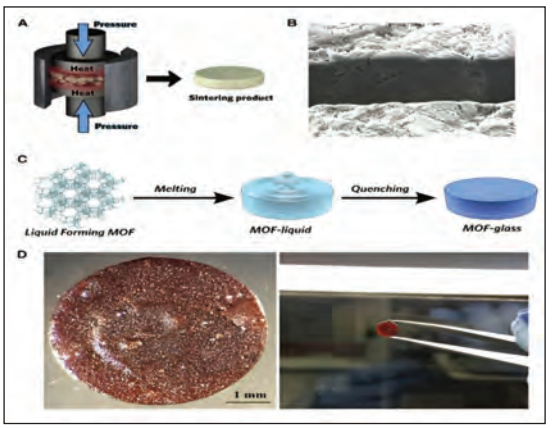

Fig.1. Hot pressing of ZIFs causes internal voids to emerge, resulting in a MOF monolith with few internal voids and high mechanical integrity [8].

2.2 Energy Field-Assisted Sintering

Spark plasma sintering (SPS) is a process that quickly densifies green-body powder materials by applying pressure, heating, and electrical current all at once. For ceramic materials, it has been extensively employed [43-44]. In the early 20th century when Taylor and colleagues coupled hot pressing with electric energy. 12 Controllable heating rates were produced by large currents given by utilizing conductive pressing tools. The applied electric field can accelerate the densification of the bulk monolith and promote phase transition [45-47].

The SPS approach is useful for creating multiphase composites due to its multidimensional parameter space and high-voltage spark, which can speed up reactions and allow for the percolation of distinct phases [48-50]. However, electrical energy has the potential to produce defects near the interface, where the metastable phases can be stabilized by the remaining energy barriers.

2.3 Liquid Phase Sintering

Meltable materials are the only ones that can be used for the method due to their high-temperature solid-liquid phase-transition behavior. Low temperature heat addition can encourage solid particle rearrangement and speed up diffusion reaction, improving densification when combined with ceramic material sintering. However, the precise procedure for metallic and/or ceramic sintering systems is still unknown.

Chemical additives can be used to lower the melting temperature of non-meltable MOFs to reach the liquid phase. The ionic liquid was combined with the archetypal with ZIF-8to aid in its melting and subsequent sintering. The thermal breakdown temperature is lower than the melting point, and the quickly dissociating ligands are stabilized by the ionic liquid. The additional ionic liquid can be extruded during the sintering process to produce bulk materials that are mechanically robust and have few voids [51].

Liquid-phase sintering of inorganic glass/indium tin oxide composites improves efficiency and uniformity of joule heat conduction and distribution, stabilizes metastable phases, and shapes microstructures, resulting in higher ionic conductivity [52-53].

Liquid-phase SPS has the potential for the production of composites due to its thermal response and joule heat, Frenkel defects, and selective interactions between solid and liquid phases [54-55]. This demonstrates the interconnectedness and complexity of the synthetic parameter space, making it a potential area of study for machine learning.

Electrowetting on dielectric conductive liquids is known as inorganic meltable materials and can be explained by the charge mobility process. This process enables quicker densification and fine-tuning of solid size-distribution profiles and offers a great deal of promise for managing the mechanical characteristics of bulk phases, stabilizing metastable phases, and influencing the interfacial properties of composite materials[56].

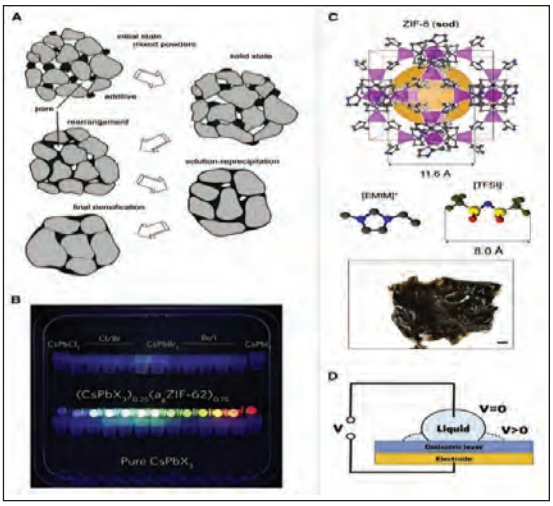

Fig. 2. Liquid-phase sintering of MOF The microstructure evolution of MOF-perovskite composites during liquid-phase sintering is illustrated by a schematic diagram, and photoluminescence enhancement [8].

2.4 Ultra-fast Sintering and Laser Sintering

The heating rate of conventional thermal sintering is important for ceramics, as the size of finer grains grows with the increased rate of heat. To take advantage of this, field-assisted sintered techniques have been developed to produce samples with a high density and tiny grain size in a matter of minutes. Laser sintering is a quick heat-rate method for sintered ceramics. When the laser pulse duration is longer than the electron-phonon thermal relaxation period, the material exposed to laser radiation will be heated by electron excitation. The ability to localize heating at specific locations is made more appealing by the laser beams ability to be concentrated within a few hundred micrometers or even less. This method can be used to create ceramic components with intricate geometries [57].

2.5 Regulation of Defect Formation

The high-temperature sintering process can result in additional defects in MOFs, which can boost ionic conductivity and catalytic efficiency. These imperfections are also related to the thermoluminescence in ceramics that possess some level of inertness.

Controlling and creating defects in a precise manner is a complex task and requires sophisticated characterization methods to fully comprehend the dynamic, chemical, and structural alterations that occur during the sintering process. Our study has shown that IR infrared spectroscopy has the potential to analyze the metal-organic bonds in Metal-Organic Frameworks (MOFs) with regard to bonding dynamics. Advanced high-energy spectroscopic imaging techniques such as X-rays and pair-distribution functions provide a deeper understanding of the short- to mid-range structures of materials created through sintering. There is a rising need for techniques that allow for spatially resolved analysis. Transmission Electron Microscopy (TEM) is used to study the distribution of crystalline and elemental phases in a composite of ZIF-8 glass and metal halide perovskite. This study could be further advanced by combining X-ray nanoprobe technology with cathodoluminescence or microscopic electron energy loss spectroscopy, though these methods are complex and require careful sample preparation, from analyzed data. Ultimately, a comprehensive perception of the relationship between the sintering state and defects will allow for the production or elimination of defects and the functionalization of the outcome is obtained [58].

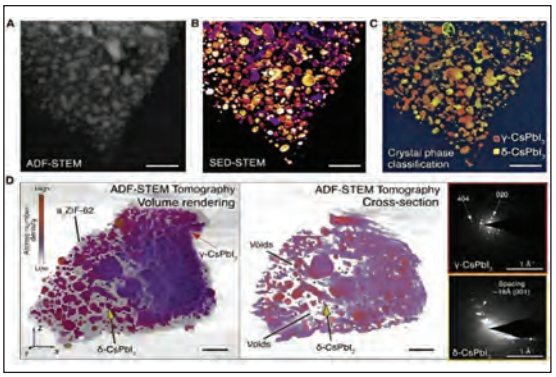

Fig. 3. Nanostructured study of composites with TEM. Scale bars are 250nm [8]

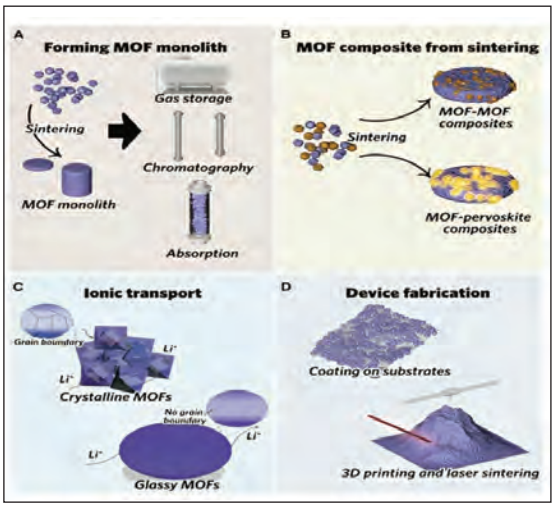

Fig. 4. MOF sintering provides application and research opportunities, such as the generation of monoliths, and new types of composite materials [8]

3 Case Studies

3.1 ZPI and ZIF-8 Powder Thermogravimetric Differential Thermal Analysis

The TG/DTA analysis revealed that ZPI has a melting point of 150°C, while thermal breakdown occurs at 160°C. A solvent release is visible in ZIF-8 between 27°C and 300°C, but the thermal breakdown is visible at temperatures of around 400°C [59-60]. The experimental findings reveal that the temperatures of sintered materials can be maintained between 110°C to 270°C, respectively.

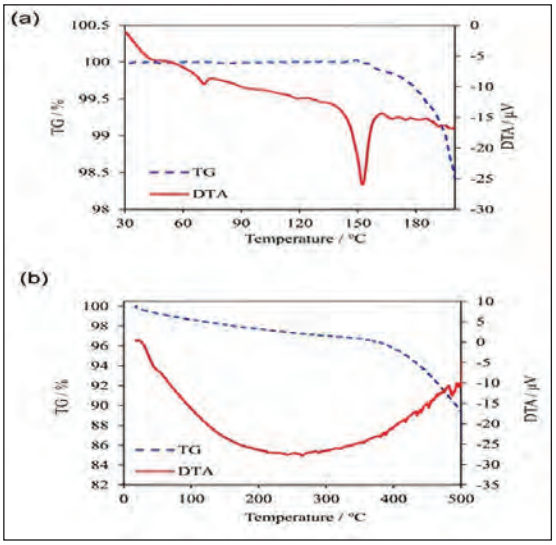

Fig. 5. The outcome for ZPI and ZIF-8 using thermogravimetric analysis (TG) and thermoanalytical technique (DTA) [22].

3.2 Displacement in ZPI and ZIF-8 Green CompactsSintering

Temperature-dependent shrinkage of ZPI is monotonic, and a final measured shrinkage of 10–20% is observed. In addition, only a slight variation in the displacement due to a change in the heating rate up to around 80°C is seen. Above 80°C, however, a quicker temperature increase causes a bigger observable shrinkage. At temperatures up to around 150°C, ZIF-8 very minimally shrinks (less than 1%), in contrast [61]. Because of thermal expansion, additional shrinking is not seen above 150°C. Additionally, the heating rate is a factor in ZIF-8's shrinkage behavior from the start of the process, with quicker heating rates showing larger shrinkage.

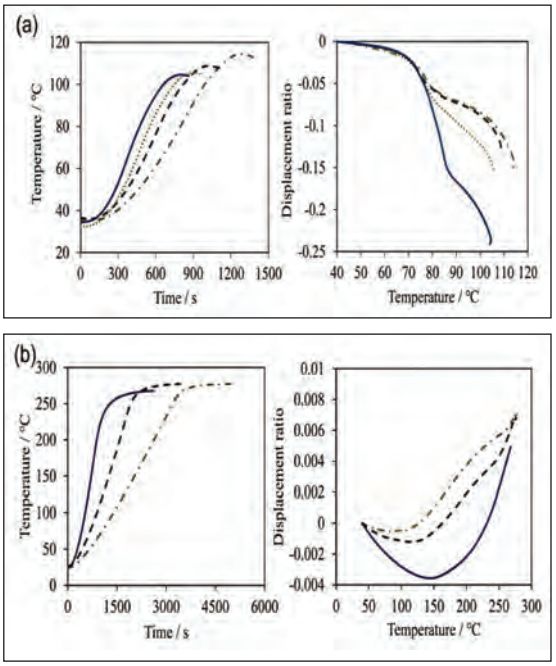

Fig. 6. ZPI and ZIF-8 shrinkage behavior and heating rate. The equivalent sample in the left and right figures, respectively, is the same line type [22].

3.3 Physical Characterization of the Sintered Compacts ZPI and ZIF-8

In ZIF-8 and ZPI, the X-ray diffraction (XRD) patterns taken of sintered MOFs at varying temperatures remain unchanged and there is no observable alteration in the XRD patterns at any temperature. Figure 7 and 8 shows The correlation between the mass and volume of the material, including its pores and water content (apparent volume), is studied. The terms "bulk density" and "bulk volume" are employed to describe the temperature dependence of granular materials [62]. In ZPI, the permeability decreases significantly as the temperatures of sintered particle process increase.

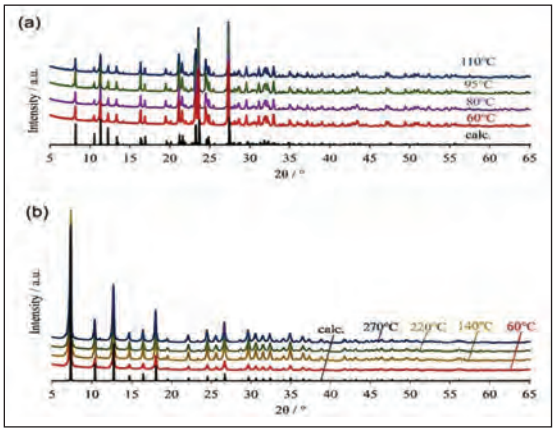

Fig. 7. ZPI and ZIF-8 bulk samplesX-ray diffraction patterns, respectively [22].

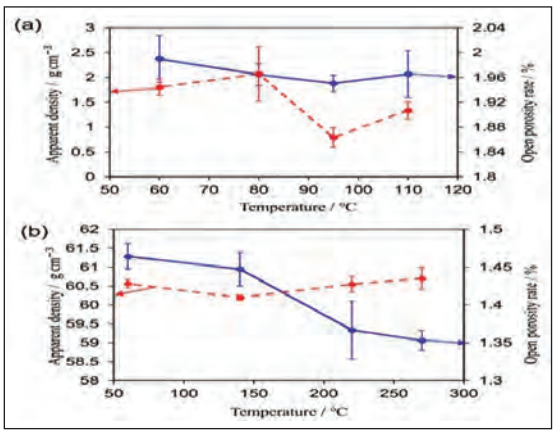

Fig. 8. Ostensible density and permeability rate of dependence on temperature for (a) ZPI and (b) ZIF-8 [22].

4 Discussions

4.1 The Mechanism of Sintering in MOFs

Metal-Organic Frameworks (MOFs) are synthesized by heating MOF precursor nanoparticles to create a solid that is thick and crystalline. The nanoparticles are heated to a temperature that is higher than the organic linker moleculesmelting point, but lower than

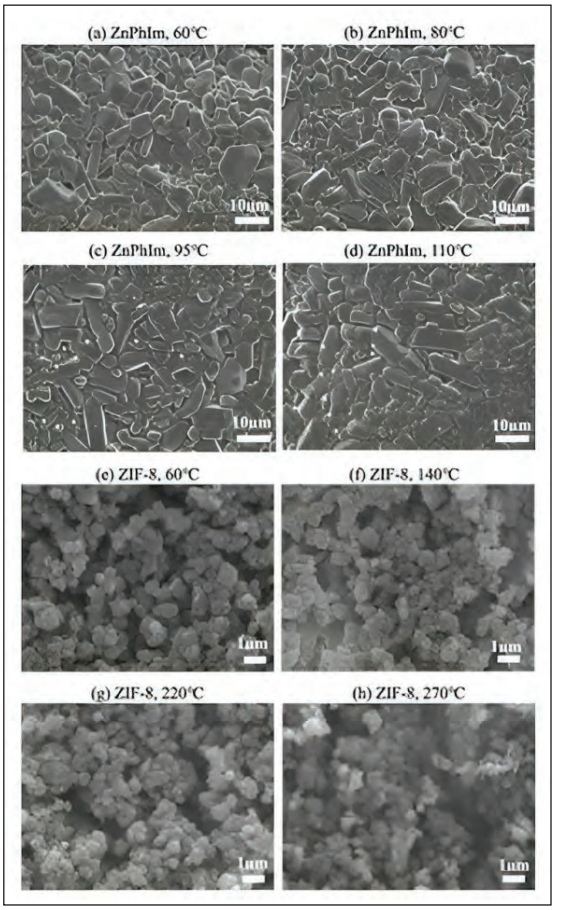

Fig. 9. ZPI and ZIF-8 images were captured using scanning electron microscopy on bulk materials [22].

the metal ions melting point. The metal ions are left behind when the organic linkers thermally degrade at high temperatures and produce volatile species.Metal ions diffuse and interact with one another, forming a network of metal-metal bonds that expand as the temperature rises [63]. This process is known as sintering and is often done in an inert environment to avoid oxidation or chemical reactions.The sintering conditions must be carefully managed to produce a dense, crystalline MOF material with a well-defined structure. If the temperature is too low, the MOF particles may not have enough energy to diffuse and connect with one another, resulting in a porous, low-density material.

Effect of Apparent Density on Sintering Temperature

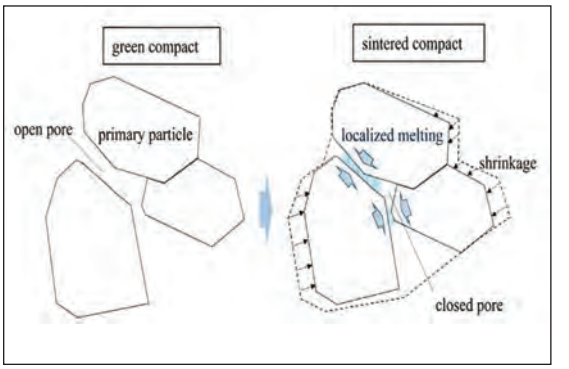

Fig. 10. Asimplified picture of the sintered process of ZPI [22].

As the temperature for sintering increases, the density of metals and ceramics appears to grow, and the porosity appears to decline, as demonstrated by the data for ZIF-8. At 95°C, the apparent density of ZPI at 95°C decreases, but there is no sign of solvent leaking [64-65]. This decrease in apparent density can be the consequence of changes to ZPI's microstructure, such as localized melting at the primary particle contact, which causes previously closed pores to open, the volume appears to increase, and the density appears to decrease.

Conclusions

The study revealed that both melting ZPI and non-melting ZIF-8 could be transformed into a bulk body through a simple process of compaction followed by sintering, without sacrificing macroscopic crystallinity. Both samples shrank during sintering, although ZPI

shrank at a rate between 10-20% and less than 1%. The study found that as the temperature for sintering was increased, the ostensible density of ZPI decreased, indicating that localized melting may have generated new closed pores.

Despite the significant advancements, MOF sintering is not used often in materials engineering applications. The modification of MOFs through amorphization has a broad range of potential applications, particularly in the vicinity of the solid-liquid phase transition. Further investigation into the relationship between kinetic amorphization and its practical capabilities should be driven by this promising area of study.

References

1. X.li, R.Lin, Sintering of Metal-Organic Frameworks – ScienceDirect (2022). https://www.sciencedirect.com/science/article/pii/S2666386422002132 (accessed February 6, 2023).
2. I.M. Hönicke, I. Senkovska, V. Bon, I.A. Baburin, N. Bönisch, S. Raschke, J.D. Evans, S. Kaskel, Balancing Mechanical Stability and Ultrahigh Porosity in Crystalline Framework Materials, Angewandte Chemie International Edition. 57 (2018) 13780–13783. https://doi.org/10.1002/anie.201808240.
3. J. Hou, A.F. Sapnik, T.D. Bennett, Metal–organic framework gels and monoliths, Chemical Science. 11 (2020) 310–323. https://doi.org/10.1039/c9sc04961d.
4. J. Hou, P. Chen, A. Shukla, A. Krajnc, T. Wang, X. Li, R. Doasa, L.H.G. Tizei, B. Chan, D.N. Johnstone, R. Lin, T.U. Schülli, I. Martens, D. Appadoo, M.S. Ari, Z. Wang, T. Wei, S.-C. Lo, M. Lu, S. Li, E.B. Namdas, G. Mali, A.K. Cheetham, S.M. Collins, V. Chen, L. Wang, T.D. Bennett, Liquid-phase sintering of lead halide perovskites and metal-organic framework glasses, Science. 374 (2021) 621–625. https://doi.org/10.1126/science.abf4460.
5. S. Li, R. Limbach, L. Longley, A.A. Shirzadi, J.C. Walmsley, D.N. Johnstone, P.A. Midgley, L. Wondraczek, T.D. Bennett, Mechanical Properties and Processing Techniques of Bulk Metal–Organic Framework Glasses, Journal of the American Chemical Society. 141 (2018) 1027–1034. https://doi.org/10.1021/jacs.8b11357.
6. R.N. Widmer, G.I. Lampronti, S. Anzellini, R. Gaillac, S. Farsang, C. Zhou, A.M. Belenguer, C.W. Wilson, H. Palmer, A.K. Kleppe, M.T. Wharmby, X. Yu, S.M. Cohen, S.G. Telfer, S.A.T. Redfern, F.-X. Coudert, S.G. MacLeod, T.D. Bennett, Pressure promoted low-temperature melting of metal–organic frameworks, Nature Materials. 18 (2019) 370–376. https://doi.org/10.1038/s41563-019-0317-4.
7. M. Suarez, A. Fernandez, J.L. Menendez, R. Torrecillas, H. U., J. Hennicke, R. Kirchner, T. Kessel, Challenges and Opportunities for Spark Plasma Sintering: A Key Technology for a New Generation of Materials, Sintering Applications. (2013). https://doi.org/10.5772/53706.
8. X. Li, R. Lin, J. Hou, L. Wang, Sintering of metal-organic frameworks, Cell Reports Physical Science. 3 (2022) 100932. https://doi.org/10.1016/j.xcrp.2022.100932.
9. T.J. Rudzik, R.A. Gerhardt, Comparison of hot pressing and spark plasma sintering in the densification behavior of indium tin oxide-borosilicate glass composites, Journal of the American Ceramic Society. 101 (2017) 577–589. https://doi.org/10.1111/jace.15254.r.
10. R.M. German, P. Suri, S.J. Park, Review: liquid phase sintering, Journal of Materials Science. 44 (2009) 1–39. https://doi.org/10.1007/s10853-008-3008-0.
11. E. Lahtinen, R.L.M. Precker, M. Lahtinen, E. Hey-Hawkins, M. Haukka, Selective Laser Sintering of Metal-Organic Frameworks: Production of Highly Porous Filters by 3D Printing onto a Polymeric Matrix, ChemPlusChem. 84 (2019) 222–225. https://doi.org/10.1002/cplu.201900081.
12. D. Schwarzbach, J. Gonzalez-Julian, O. Guillon, V. Roddatis, C.A. Volkert, Towards In-Situ Electron Microscopy Studies of Flash Sintering, Ceramics. 2 (2019) 472–487. https://doi.org/10.3390/ceramics2030036.
13. R. Serrazina, P.M. Vilarinho, A.M.O.R. Senos, L. Pereira, I.M. Reaney, J.S. Dean, Modelling the particle contact influence on the Joule heating and temperature distribution during FLASH sintering, Journal of the European Ceramic Society. 40 (2020) 1205–1211. https://doi.org/10.1016/j.jeurceramsoc.2019.12.015.

14. S. Horike, S.S. Nagarkar, T. Ogawa, S. Kitagawa, A New Dimension for Coordination Polymers and Metal–Organic Frameworks: Towards Functional Glasses and Liquids, Angewandte Chemie International Edition. 59 (2020) 6652–6664. https://doi.org/10.1002/anie.201911384.

15. C. Schmerbauch, J. Gonzalez-Julian, R. Röder, C. Ronning, O. Guillon, Flash Sintering of Nanocrystalline Zinc Oxide and its Influence on Microstructure and Defect Formation, Journal of the American Ceramic Society. 97 (2014) 1728–1735. https://doi.org/10.1111/jace.12972.

16. R. Gaillac, P. Pullumbi, K.A. Beyer, K.W. Chapman, D.A. Keen, T.D. Bennett, F.-X. Coudert, Liquid metal–organic frameworks, Nature Materials. 16 (2017) 1149–1154. https://doi.org/10.1038/nmat4998.

17. B.M. Connolly, M. Aragones-Anglada, J. Gandara-Loe, N.A. Danaf, D.C. Lamb, J.P. Mehta, D. Vulpe, S. Wuttke, J. Silvestre-Albero, P.Z. Moghadam, A.E.H. Wheatley, D. Fairen-Jimenez, Tuning porosity in macroscopic monolithic metal-organic frameworks for exceptional natural gas storage, Nature Communications. 10 (2019). https://doi.org/10.1038/s41467-019-10185-1.

18. B.M. Connolly, D.G. Madden, A.E.H. Wheatley, D. Fairen-Jimenez, Shaping the Future of Fuel: Monolithic Metal–Organic Frameworks for High-Density Gas Storage, Journal of the American Chemical Society. 142 (2020) 8541–8549. https://doi.org/10.1021/jacs.0c00270.

19. Q.-L. Zhu, Q. Xu, Metal–organic framework composites, Chem. Soc. Rev. 43 (2014) 5468–5512. https://doi.org/10.1039/c3cs60472a.

20. R. Lin, Y. Yao, M.Y.B. Zulkifli, X. Li, S. Gao, W. Huang, S. Smart, M. Lyu, L. Wang, V. Chen, J. Hou, Binder-free mechanochemical metal–organic framework nanocrystal coatings, Nanoscale. 14 (2022) 2221–2229. https://doi.org/10.1039/d1nr08377e.

21. S. Mallakpour, E. Azadi, C.M. Hussain, MOF/COF-based materials using 3D printing technology: applications in water treatment, gas removal, biomedical, and electronic industries, New Journal of Chemistry. 45 (2021) 13247–13257. https://doi.org/10.1039/d1nj02152d.

22. I. Miyazaki, Y. Masuoka, A. Suzumura, S. Moribe, M. Umehara, Direct Sintering Behavior of Metal-Organic Frameworks/Coordination Polymers, ACS Omega. 7 (2022) 47906–47911. https://doi.org/10.1021/acsomega.2c05732.

23. H. Furukawa, K.E. Cordova, M. O'Keeffe, O.M. Yaghi, The Chemistry and Applications of Metal-Organic Frameworks, Science. 341 (2013). https://doi.org/10.1126/science.1230444.

24. P. Küsgens, A. Zgaverdea, H.-G. Fritz, S. Siegle, S. Kaskel, Metal-Organic Frameworks in Monolithic Structures, Journal of the American Ceramic Society. 93 (2010) 2476–2479. https://doi.org/10.1111/j.1551-2916.2010.03824.x.

25. R.N. Widmer, G.I. Lampronti, B. Kunz, C. Battaglia, J.H. Shepherd, S.A.T. Redfern, T.D. Bennett, Manufacturing Macroporous Monoliths of Microporous Metal–Organic Frameworks, ACS Applied Nano Materials. 1 (2018) 497–500. https://doi.org/10.1021/acsanm.7b00335.

26. J. Yao, H. Wang, Zeolitic imidazolate framework composite membranes and thin films: synthesis and applications, Chem. Soc. Rev. 43 (2014) 4470–4493. https://doi.org/10.1039/c3cs60480b.

27. Y. Liu, E. Hu, E.A. Khan, Z. Lai, Synthesis and characterization of ZIF-69 membranes and separation for CO2/CO mixture, Journal of Membrane Science. 353 (2010) 36–40. https://doi.org/10.1016/j.memsci.2010.02.023.

28. H. Ji, S. Hwang, K. Kim, C. Kim, N.C. Jeong, Direct in Situ Conversion of Metals into Metal–Organic Frameworks: A Strategy for the Rapid Growth of MOF Films on Metal Substrates, ACS Applied Materials & Interfaces. 8 (2016) 32414–32420. https://doi.org/10.1021/acsami.6b12755.

29. K. Khaletskaya, S. Turner, M. Tu, S. Wannapaiboon, A. Schneemann, R. Meyer, A. Ludwig, G. Van Tendeloo, R.A. Fischer, Self-Directed Localization of ZIF-8 Thin Film Formation by Conversion of ZnO Nanolayers, Advanced Functional Materials. 24 (2014) 4804–4811. https://doi.org/10.1002/adfm.201400559.

30. A. Demessence, C. Boissière, D. Grosso, P. Horcajada, C. Serre, G. Férey, G.J.A.A. Soler-Illia, C. Sanchez, Adsorption properties in high optical quality nanoZIF-8 thin films with tunable thickness, Journal of Materials Chemistry. 20 (2010) 7676. https://doi.org/10.1039/c0jm00500b.

31. Z. Kang, L. Fan, D. Sun, Recent advances and challenges of metal–organic framework membranes for gas separation, Journal of Materials

Chemistry A. 5 (2017) 10073–10091. https://doi.org/10.1039/c7ta01142c.

32. M. Tricarico, J.-C. Tan, Mechanical properties and nanostructure of monolithic zeolitic imidazolate frameworks: a nanoindentation, nano spectroscopy, and finite element study, Materials Today Nano. 17 (2022) 100166. https://doi.org/10.1016/j.mtnano.2021.100166.
33. D. Bazer-Bachi, L. Assié, V. Lecocq, B. Harbuzaru, V. Falk, Towards industrial use of metal-organic framework: Impact of shaping on the MOF properties, Powder Technology. 255 (2014) 52–59. https://doi.org/10.1016/j.powtec.2013.09.013.
34. D. Umeyama, S. Horike, M. Inukai, T. Itakura, S. Kitagawa, Reversible Solid-to-Liquid Phase Transition of Coordination Polymer Crystals, Journal of the American Chemical Society. 137 (2015) 864–870. https://doi.org/10.1021/ja511019u.
35. J. Hou, C.W. Ashling, S.M. Collins, A. Krajnc, C. Zhou, L. Longley, D.N. Johnstone, P.A. Chater, S. Li, M.-V. Coulet, P.L. Llewellyn, F.-X. Coudert, D.A. Keen, P.A. Midgley, G. Mali, V. Chen, T.D. Bennett, Metal-organic framework crystal-glass composites, Nature Communications. 10 (2019). https://doi.org/10.1038/s41467-019-10470-z.
36. S. Horike, S.S. Nagarkar, T. Ogawa, S. Kitagawa, A New Dimension for Coordination Polymers and Metal–Organic Frameworks: Towards Functional Glasses and Liquids, Angewandte Chemie International Edition. 59 (2020) 6652–6664. https://doi.org/10.1002/anie.201911384.
37. T.D. Bennett, S. Horike, Liquid, glass and amorphous solid states of coordination polymers and metal–organic frameworks, Nature Reviews Materials. 3 (2018) 431–440. https://doi.org/10.1038/s41578-018-0054-3.
38. R.N. Widmer, G.I. Lampronti, S. Anzellini, R. Gaillac, S. Farsang, C. Zhou, A.M. Belenguer, C.W. Wilson, H. Palmer, A.K. Kleppe, M.T. Wharmby, X. Yu, S.M. Cohen, S.G. Telfer, S.A.T. Redfern, F.-X. Coudert, S.G. MacLeod, T.D. Bennett, Pressure promoted low-temperature melting of metal–organic frameworks, Nature Materials. 18 (2019) 370–376. https://doi.org/10.1038/s41563-019-0317-4.
39. R.N. Widmer, G.I. Lampronti, S. Chibani, C.W. Wilson, S. Anzellini, S. Farsang, A.K. Kleppe, N.P.M. Casati, S.G. MacLeod, S.A.T. Redfern, F.-X. Coudert, T.D. Bennett, Rich Polymorphism of a Metal–Organic Framework in Pressure–Temperature Space, Journal of the American Chemical Society. 141 (2019) 9330–9337. https://doi.org/10.1021/jacs.9b03234.
40. K.S. Park, Z. Ni, A.P. Côté, J.Y. Choi, R. Huang, F.J. Uribe-Romo, H.K. Chae, M. O'Keeffe, O.M. Yaghi, Exceptional chemical and thermal stability of zeolitic imidazolate frameworks, Proceedings of the National Academy of Sciences. 103 (2006) 10186–10191. https://doi.org/10.1073/pnas.0602439103.
41. K.H. Brosnan, G.L. Messing, D.K. Agrawal, Microwave Sintering of Alumina at 2.45 GHz, Journal of the American Ceramic Society. 86 (2003) 1307–1312. https://doi.org/10.1111/j.1151-2916.2003.tb03467.x.
42. Rayappa Shrinivas Mahale, V. Shamanth, P.C. Sharath, R. Shashanka, K. Hemanth, A review on spark plasma sintering of duplex stainless steels, Materials Today: Proceedings. 45 (2021) 138–144. https://doi.org/10.1016/j.matpr.2020.10.357.
43. R.S. Mahale, Shamanth V, Hemanth K, Sharath P C, R. Shashanka, Mechanical testing of spark plasma sintered materials: A reviewon Recent Developments In Mechanical Engineering [RDME-2021]. (2022). https://doi.org/10.1063/5.0080183.
44. R. Shashanka, D. Chaira, Optimization of milling parameters for the synthesis of nano-structured duplex and ferritic stainless-steel powders by high energy planetary milling, Powder Technology. 278 (2015) 35–45. https://doi.org/10.1016/j.powtec.2015.03.007.
45. Shashanka. R, D. Chaira, Development of nano-structured duplex and ferritic stainless steels by pulverisette planetary milling followed by pressureless sintering, Materials Characterization. 99 (2015) 220–229. https://doi.org/10.1016/j.matchar.2014.11.030.
46. Shashanka. R, D. Chaira, Phase transformation and microstructure study of nano-structured austenitic and ferritic stainless-steel powders prepared by planetary milling, Powder Technology. 259 (2014) 125–136. https://doi.org/10.1016/j.powtec.2014.03.061.
47. R. Shashanka, D. Chaira, Effects of Nano-Y2O3 and Sintering Parameters on the Fabrication of PM Duplex and Ferritic Stainless Steels, Acta Metallurgica Sinica (English Letters). 29 (2016) 58–

71. https://doi.org/10.1007/s40195-015-0362-1.

48. C. Suryanarayana, Mechanical alloying and milling, Progress in Materials Science. 46 (2001) 1–184. https://doi.org/10.1016/s0079-6425(99)00010-9.

49. C. Suryanarayana, E. Ivanov, V.V. Boldyrev, The science and technology of mechanical alloying, Materials Science and Engineering: A. 304–306 (2001) 151–158. https://doi.org/10.1016/s0921-5093(00)01465-9.

50. C. Suryanarayana, N. Al-Aqeeli, Mechanically alloyed nanocomposites, Progress in Materials Science. 58 (2013) 383–502. https://doi.org/10.1016/j.pmatsci.2012.10.001.

51. C. Suryanarayana, D. Mukhopadhyay, S.N. Patankar, F.H. Froes, Grain size effects in nanocrystalline materials, Journal of Materials Research. 7 (1992) 2114–2118. https://doi.org/10.1557/jmr.1992.2114.

52. ms el kandrani, Mechanical Alloying, n.d. https://books.google.com/books/about/Mechanical_Alloying.html?id=28NMb5SizbsC.

53. D. ms el kandrani, Mechanical Alloying, n.d. https://books.google.com/books/about/Mechanical_Alloying.html?id=kwjGAgAAQBAJ.

54. M.B. Shongwe, S. Diouf, M.O. Durowoju, P.A. Olubambi, Effect of sintering temperature on the microstructure and mechanical properties of Fe–30%Ni alloys produced by spark plasma sintering, Journal of Alloys and Compounds. 649 (2015) 824–832. https://doi.org/10.1016/j.jallcom.2015.07.223.

55. B.A. Obadele, O.O. Ige, P.A. Olubambi, Fabrication and characterization of titanium-nickel-zirconia matrix composites prepared by spark plasma sintering, Journal of Alloys and Compounds. 710 (2017) 825–830. https://doi.org/10.1016/j.jallcom.2017.03.340.

56. O.E. Falodun, B.A. Obadele, S.R. Oke, M.E. Maja, P.A. Olubambi, Effect of sintering parameters on densification and microstructural evolution of nano-sized titanium nitride reinforced titanium alloys, Journal of Alloys and Compounds. 736 (2018) 202–210. https://doi.org/10.1016/j.jallcom.2017.11.140.

57. M.A. Awotunde, A.O. Adegbenjo, B.A. Obadele, M. Okoro, B.M. Shongwe, P.A. Olubambi, Influence of sintering methods on the mechanical properties of aluminum nanocomposites reinforced with carbonaceous compounds: A review, Journal of Materials Research and Technology. 8 (2019) 2432–2449. https://doi.org/10.1016/j.jmrt.2019.01.026.

58. A.O. Adegbenjo, P.A. Olubambi, J.H. Potgieter, M.B. Shongwe, M. Ramakokovhu, Spark plasma sintering of graphitized multi-walled carbon nanotube reinforced Ti6Al4V, Materials & Design. 128 (2017) 119–129. https://doi.org/10.1016/j.matdes.2017.05.003.

59. N.B. Pradeep, M.M.R. Hegde, S. Rajendrachari, A.O. Surendranathan, Investigation of microstructure and mechanical properties of microwave consolidated TiMgSr alloy prepared by high energy ball milling, Powder Technology. 408 (2022) 117715. https://doi.org/10.1016/j.powtec.2022.117715.

60. N.B. Pradeep, M.M.R. Hegde, G.C. Manjunath Patel, K. Giasin, D.Y. Pimenov, S. Wojciechowski, Synthesis and characterization of mechanically alloyed nanostructured ternary titanium-based alloy for bio-medical applications, Journal of Materials Research and Technology. 16 (2022) 88–101. https://doi.org/10.1016/j.jmrt.2021.11.101.

61. S. Pasebani, A.K. Dutt, J. Burns, I. Charit, R.S. Mishra, Oxide dispersion strengthened nickel based alloys via spark plasma sintering, Materials Science and Engineering: A. 630 (2015) 155–169. https://doi.org/10.1016/j.msea.2015.01.066.

62. S. Pasebani, I. Charit, Effect of alloying elements on the microstructure and mechanical properties of nanostructured ferritic steels produced by spark plasma sintering, Journal of Alloys and Compounds. 599 (2014) 206–211. https://doi.org/10.1016/j.jallcom.2014.01.243.

63. Y.Q. Wu, K.N. Allahar, J. Burns, B. Jaques, I. Charit, D.P. Butt, J.I. Cole, Fe-Cr-Mo based ODS alloys via spark plasma sintering: A combinational characterization study by TEM and APT, Crystal Research and Technology. 49 (2013) 645–652. https://doi.org/10.1002/crat.201300173.

64. A. Mondal, D. Agrawal, A. Upadhyaya, Microwave Heating of Pure Copper Powder with Varying Particle Size and Porosity, Journal of Microwave Power and Electromagnetic Energy. 43 (2008) 5–10. https://doi.org/10.1080/08327823.2008.11688599.

65. R.M. German, B.H. Rabin, Enhanced Sintering Through Second Phase Additions, Powder Metallurgy. 28 (1985) 7–12. https://doi.org/10.1179/pom.1985.28.1.7.

A COMPARATIVE EVALUATION OF LUMINESCENT ZnO NANOPOWDERS SYNTHESIZED BY BATCH, MICROWAVE-ASSISTED AND CONTINUOUS FLOW PROCESSES - CONNECTING THE VOIDS

Sayoni Sarkar [a], Rohit Srivastava [b], Ajit R. Kulkarni [a,c*]

[a] Centre for Research in Nano Technology and Science, IIT-Bombay, Mumbai, India

[b] Department of Biosciences and Bioengineering, IIT-Bombay, Mumbai, India

[c] Department of Metallurgical Engineering and Materials Science, IIT-Bombay, Mumbai, India

Abstract: *Luminescent ZnO nanopowders (NPs) were prepared by three synthesis protocols — batch reactor assembly, microwave (MW)-assisted method, and a novel continuous flow platform (CFP) equipped with a helical coil reactor. The reaction milieu was made thermodynamically favorable for accelerating oxygen vacancy promotion to engineer the bandgap. The synthesis routes were evaluated and compared based on the quality of the nanopowders in terms of size distribution, photoluminescence quantum yield (PLQY), and specific surface area. The results elucidated that the batch and MW-assisted strategies were plagued by inefficient mixing and limited yield. Thus, to overcome these drawbacks, a scalable yet affordable route for producing these NPs in larger quantity while ensuring superior material properties was designed and implemented. The crux of this flow platform lies in accurate control of nucleation events through improved fluid dynamics and heat transport enabled by the reactor's configuration. The NPs fabricated using this CFP manifested monodispersity, superior PLQY and yield. Due to these lucrative characteristics, the flow platform hold potential as a viable and encouraging alternative to the traditional nanopowder synthesis approaches.*

Keywords: *Luminescent ZnO nanopowders, oxygen vacancies, batch process, microwave-assisted method, continuous flow platform, scalable*

1. Introduction

The primary impetus driving technological innovations of nanoscale metal oxides is the ability to modulate physical and chemical characteristics by precisely controlling size and morphology. Although conventional batch processes have demonstrated efficacy, they are often limited by poor process reliability, yield, and cost-effectiveness. In recent times, microwave-assisted (MW) methods have been representing novel nanoparticle synthesis strategies that are proficient (energy saving and high heating rate) and flexible. Despite the benefits, there exist bottlenecks associated with the difficulty of scaling up from lab-scale to large-scale production [1,2,3]. To address this, we designed a pilot-scale continuous flow reactor prototype for the synthesis of defect-engineered ZnO nanocrystals (NCs) on a gram-scale and compared the structural and optical properties of the NCs with the batch and MW methods.

The size-tailored defect emission of ZnO NCs has profound implications in value added-products, namely, paints, bio-imaging, sunscreens, anti-counterfeit inks, and other applications of socio-economic importance [5,6]. Alteration of the bandgap through deliberate incorporation of oxygen vacancies during the synthesis by creating a minimal oxygen milieu makes these nanostructures versatile and synergistically enhances their functionalities. Therefore, it is vital to understand the role of the batch, MW, and continuous flow syntheses (CFS) on the

structure and properties of the as-synthesized ZnO.

In this work, we present the luminescent ZnO nanopowder synthesis by batch, MW, and continuous flow route. Some encouraging results have been demonstrated here that compare the photoluminescent characteristics of the NCs obtained from the different synthesis strategies. Further, to understand the effect

of the synthesis process on the structure, size distribution, bandgap, defect emission characteristics, and colloidal stability, x-ray diffraction (XRD), high resolution transmission electron microscopy (HR-TEM), UV-visible (UV), and photoluminescence spectroscopy, and dynamic light scattering, respectively, were employed.

2. Experimental procedure

2.1 Chemicals

Zinc acetate dihydrate ($Zn(CH_3COO)_2$) (99.99%), lithium hydroxide (LiOH) (analytical grade), and cis-9-octadecenoic acid (oleic acid Pure) were procured from Sigma Aldrich and used as received.

2.2 Methodology

Our endeavors commenced by fabricating oxygen vacancy engineered ZnO NCs in batch and microwave-assisted process as a preliminary step. Absolute ethanol was used as the solvent medium for preparing Zn(CH3COO)2.H2O and LiOH solutions by magnetic stirring. For the conventional batch process, the $Zn(CH_3COO)_2$. H_2O solution was heated to 75˚C and the ethanolic LiOH was poured at a rapid rate to initiate the reaction. The reaction took place for 75s, following which, the round bottomed flask was quenched to room temperature. In case of the MW synthesis, the precursor solutions were poured in a glass vial and sealed to create an oxygen deficient atmosphere. An Anton Paar Monowave reactor (operating frequency ~ 2.45 GHz) was employed for the synthesis. The reaction temperature and time were same as the batch mode to facilitate easy comparison between the protocols.

Consequently, the quality and yield of the nanopowders obtained from the batch and microwave were assessed. Agglomeration among the particles was noticeable in the batch synthesized-nanostructures. We confirmed that despite the advantages of volumetric heating in MW-assisted synthesis, which aids in quickly overcoming the energy barrier for activation and nucleation events for forming uniform sized NCs, the process is unamenable for industrial-scale production.

This issue was resolved by translating the batch protocol to the continuous flow platform (CFP) for gram-scale synthesis of ZnO NPs. Peristaltic pumps were used to feed the precursor solutions which were separately prepared by dissolving $Zn(CH_3COO)_2$. H_2O and LiOH through magnetic stirring. The solutions were allowed to pass through the designed helical coil reactor and collected in a bottle placed in an ice-bath to rapidly quench the NCs formed. The water bath in which the helical coil reactor was placed was maintained at 75˚C, similar to the batch and MW processes [4]. The product at the output end was collected and then subjected to centrifugation to obtain the ZnO nanopowders.

The photoluminescence of the samples was characterized using HORIBA Jobin Yvon Fluorolog 3 spectrofluorometer. For estimating

the bandgap of the as-synthesized nanocrystals, a JASCO V-570 UV-Vis Spectrophotometer was employed. The HR-TEM images were recorded with a Tecnai G2, F30 transmission electron microscope (300 kV). X-ray diffraction patterns were acquired with Cu Kα radiation using a PANalytical Empyrean powder diffractometer. ZetaSizer Nano- ZS, Malvern Instruments, was used for the colloidal stability measurements by examining the hydrodynamic sizes of the NCs obtained from the batch (ZnO_B-NCs), MW (ZnO_{MW}-NCs), and flow process (ZnO_{CFS}-NCs). Brunauer–Emmett–Teller (BET) surface area measurement was performed for the powder quality assessment.

3. Results and discussion

PL spectroscopy was carried out for the as-prepared ZnO_B-NCs, ZnO_{MW}-NCs, and ZnO_{CFS}-NCs to analyze the formation of maximum concentration of oxygen vacancy defects under kinetically favourable conditions and the role of molar concentration on enhancing the luminescence. The appreciable changes were denoted from the full-width half maxima (FWHM) and PL quantum yield (PLQY) enlisted in Table 1. Fig 1. demonstrates the comparison of the luminescent characteristics of the three different ZnO NCs. The advantage of CFP is that the helical nature of the reactor expedites

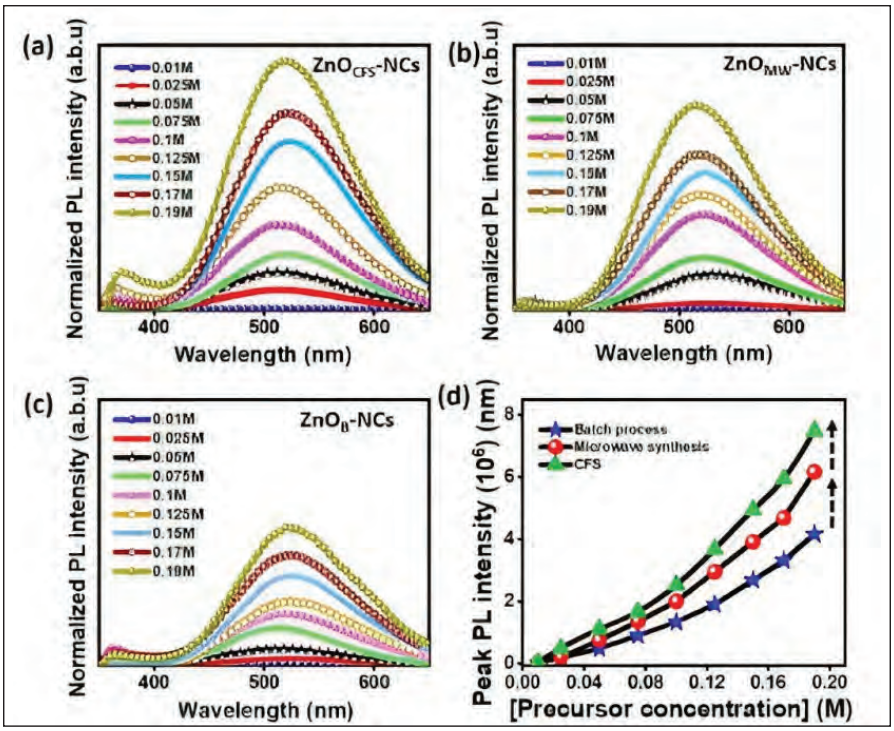

Fig. 1. Effect of molar concentration of precursors on the photoluminescent characteristics are presented though the PL spectra recorded for ZnO NCs prepared by (a) continuous flow platform (b) microwave-assisted method (c) batch reactor, under identical synthesis conditions – temperature of 75°C and reaction time of 75s (d) Variation of peak PL intensity with precursor molar concentrations for the three processes denoting the influence of intrinsic reactor characteristics - mixing and heat transport on enhancing the luminescence.

the heat transfer, therefore, eliminating the generation of localized "hot spots" or temperature gradients. This high heating rate (2.5˚C/s) of CFP is most conducive for oxygen vacancy generation and led to the highest PL intensity with increasing molar concentration of [Zn^{2+}]/[OH-], among the three processes. On the other hand, MW-assisted method comprises of volumetric heating that augments the heating rate with homogenous temperature distribution throughout the reactor. For our MW-synthesis the heating rate was 1.7˚C/s (50W power) and that of batch was 0.18˚C/s. Although the performance of MW reactors is commensurable to CFP, yet the mixing and yield are limited. To make the luminescent NPs industrially viable, it was crucial to maximize the yield with simultaneous enhancement of defect emission. Hence, for improving the yield, the molarity of the precursors was increased till the precursor salts did not dissolve further. For the highest molarity of 0.19M, the PL intensity was found to be maximum for CFP. The concentration dependent-increment in luminescence is due to the presence of highest number of oxygen vacancies at 0.19M. The nanopowder synthesized by CFP also exhibited a prolonged photostability for over 330 days. A (5.79%) reduction in FWHM was noted for ZnO_{CFS}-NCs, and (5.07%) for ZnO_{MW}-NCs. Moreover, the PLQY estimated for 0.19M ZnO_B-NCs, ZnO_{MW}-NCs, and ZnO_{CFS}-NCs with rhodamine 6G as the standard was in the following order: ZnO_B-NCs (0.40) < ZnO_{MW}-NCs (0.61) < ZnO_{CFS}-NCs (0.89). These results hold evidence of how accurately governed reaction environment favours the kinetics of nanopowder formation and boosts their desired characteristics.

Table 1. Comparison of the photoluminescent characteristics of the as-synthesized ZnO nanopowders

Samples	PLQY[b*]	FWHM[a*] (nm)
ZnOB-NCs	0.40	138
ZnOMW-NCs	0.61	131
ZnOCFS-NCs	0.89	130

[a]FWHM is estimated from PL spectra (Fig 1a; 1b; 1c), bQY is determined from PL spectra (Fig 1a; 1b; 1c), *The FWHM and PLQY have been estimated for samples prepared with precursors having molar concentration of 0.1M

Fig 2. presents the the UV-visible absorption spectra of the engineered ZnO nanopowders obtained at identical reaction conditions of temperature (75˚C) and reaction time (75s). The ZnO_{CFS} NPs exhibited an absorption maximum at 345 nm, while that of nano-ZnO_{MW} and ZnO_B were 349 nm and 358 nm, respectively. This distinct blueshift in the band edge corresponds well with the wider bandgap of ~ 3.48 eV compared to ZnO_{MW} (~ 3.44 eV) and ZnO_B (3.36 eV) NPs. These spectral changes are attributed to the size-dependent quantum confinement effects. Based on the Tauc's plot approach, the absorption spectra were re-plotted to estimate the optical bandgap. Upon extrapolating the linear segment of the curves plotted using equation (1), till the straight line intersects the hv axis. The value of the intercept gives the estimated bandgap (E_{ZnO}).

$$(\alpha h\nu)^2 = A\,(h\nu - E_{ZnO}) \quad \ldots\ldots (1)$$

In the above equation, hv is the photon energy necessary to excite an electron. The particle sizes calculated for the three samples by considering their bandgaps denoted that ZnO_{CFS} NPs were the smallest ~ 5.2 nm, followed by ZnO_{MW} ~ 6.4 nm, and ZnO_B ~ 8.8 nm. Thus, it is inferred

that the shifts observed in the PL spectra of the samples synthesized by the three processes are because of the quantum size effects.

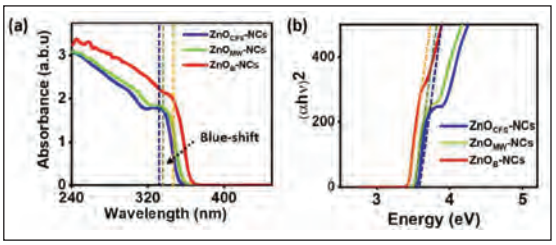

Fig. 2. (a) UV-visible absorption spectra of ethanolic solutions of ZnOCFS-NCs, ZnOMW-NCs, and ZnOB-NCs representing the blue-shift of the band edge from 358 nm to 345 nm. (b) Tauc's plot obtained by re-plotting (a) by using equation (1) to calculate the bandgap of the samples.

The spherical morphology and size distribution of the NCs are observed from the HR-TEM images (Fig 3.). The images denoted good crystalline quality and non-agglomeration that the material system exhibited, particularly ZnO_{CFS}-NCs. ZnO_B-NCs, ZnO_{MW}-NCs, and ZnO_{CFS}-NCs were prepared under identical conditions of temperatures and residence times to understand how the intrinsic reactor properties like mixing and heat distribution influences the reaction kinetics and Lamer-mediated nucleation-growth phenomena. The average particle sizes deduced from the TEM micrographs of ZnO_B-NCs, ZnO_{MW}-NCs, and ZnO_{CFS}-NCs are 6.1 nm, 5.7 nm, and 4.5 nm. Homogeneity in morphology and size are clearly evident in flow synthesized-NCs, however, slight increment in size with polydispersity is seen for the other two samples. The distance between the lattice planes of ZnO NCs was ascertained to be 0.26 nm, which is in relation to the (101) plane. We envisage that the secondary flow formation in the helical coil reactor, accelerates the nucleation of the NCs leading to the highly monodispersed nature, in comparison with ZnO_B-NCs and ZnO_{MW}-NCs. It is important to note that although the rapid dielectric heating employed in the MW-assisted protocol expedited the nucleation-growth kinetics, however, the mixing efficiency was not as high as CFP, leading to a marginal increase in size. Interestingly, the batch reactor led to somewhat broader size distribution which can be attributed to i) the generation of temperature gradients because of the small surface-to-volume ratio of the reactor compared to the MW and CFP and ii) the classical stirring speed used in the batch reactor drives the diffusion-mediated mixing which hampers the reaction efficiency.

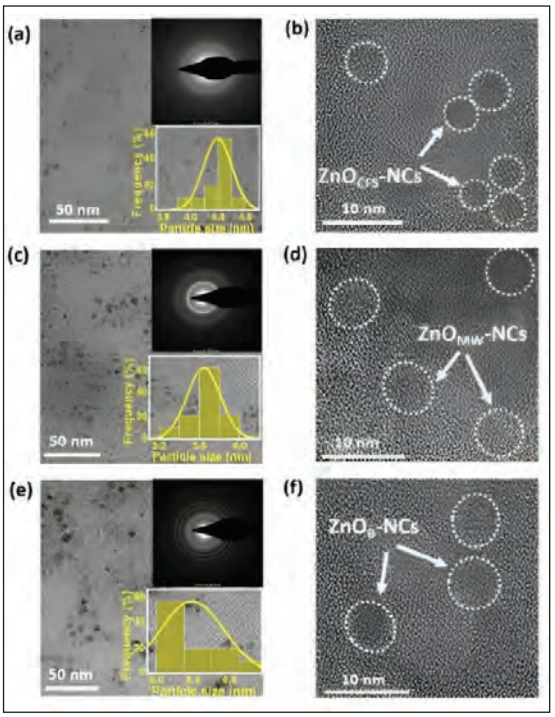

Fig. 3. TEM and HR-TEM micrographs of engineered ZnO nanopowders obtained through (a-b) CFP; (c-d) MW-assisted method, and (e-f) batch synthesis, respectively. Histograms at the lower right insets of the images ((a), (c), and (e)) show the corresponding particle size distributions. The selected area diffraction patterns are depicted in the upper right inset in each of ((a), (c), and (e)). The dotted ovals marked in ((b), (d), and (f)) are for eye guide and show the spherical ZnO NPs formed.

XRD patterns of the nanopowders indicated the formation of phase pure ZnO with wurtzite crystal structure, in accordance with JCPDS-ICDD index card no. 36–1451, as shown in Fig 4. The crystallite sizes obtained from (101) peak of the nanocrystals using Debye-Scherrer equation was in the following order: ZnO_{CFS} NPs ~ 3.7 nm < ZnO_{MW} NPs ~ 4.6 nm < ZnO_B NPs ~ 5.2 nm, in consonance with the average particle sizes obtained from TEM. The diffraction maxima exhibited broadening which can be ascribed to the presence of oxygen vacancy defects that enhance the lattice strain and the small dimensions of the particles (nano-size effects). This feature was present in the spectra of all the three samples.

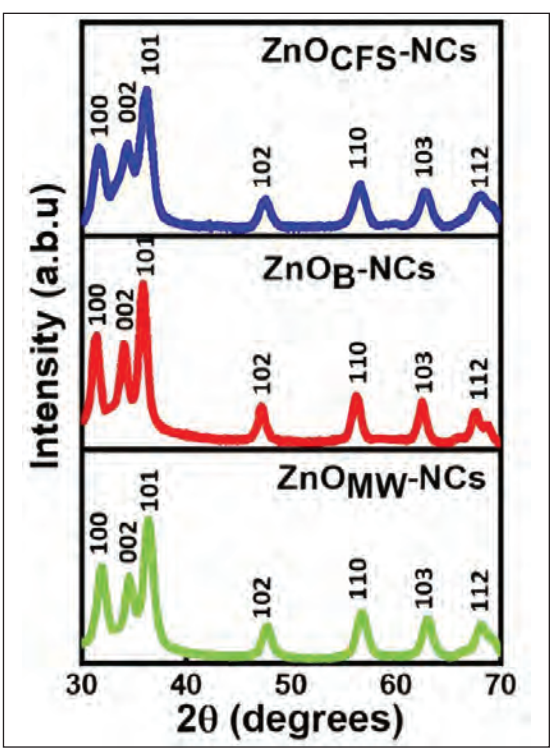

Fig. 4. Powder x-ray diffraction patterns of ZnOCFS NCs, ZnOmw NCs, and ZnOB NCs indicating a Wurtzite crystal structure.

The BET surface area analysis was performed to contrast the quality of the luminescent nanopowders obtained from the batch, MW-assisted method and check for particle agglomeration, if any. Determination of the specific surface areas involves taking into account the nitrogen physisorption isotherm. The BET surface area (SA) of ZnO_{CFS} NPs was measured to be ~247 ± 6 m^2/g, which is roughly 1.4 times higher than ZnO_B NPs (SA ~ 174 ± 2 m^2/g), while 1.2 times more than ZnO_{MW} NPs (SA ~ 206± 5 m^2/g). The decrease in specific surface area underlines the increase in particle agglomeration and reduction in powder quality. The findings suggest that the synthesis process largely influences the powder quality. Rapid molecular mixing enabled by the helical coil due to secondary flows aid in negating particle aggregation, thereby enhancing the BET-surface area. However, the local inhomogeneities that are predominant in the batch synthesis, slow down the nucleation phenomena and make it difficult to regulate. This result in increased agglomeration and lowers the surface area of the nanopowders.

Table 2. denotes the results of six independent experiments carried out to determine the colloidal stability of the ZnOCFS, ZnOMW and ZnOB nanostructures by measuring their hydrodynamic size and polydispersity index. In case of nano-ZnOCFS a monomodal distribution was measured by DLS, illustrating the effect of regulated mixing and uniform temperature distribution achieved in CFP. An increase in polydispersity index of 52% was observed for the batch process, while that of MW method was 37%, compared to CFP. The reproducibility was significantly improved for CFP and MW synthesis than batch mode. The standard

deviations of the average hydrodynamic size obtained from the experimental values, indicate drastic difference for batch (9.64) and MW-assisted process (3.37) than CFP (0.18). These observations imply that even minor variations in mixing and heat distribution can make one synthesis protocol more favourable than the other. This also impacts the properties of the end products akin to particle size distribution. The fast heating and mixing in CFP result in short nucleation events and prevents any unwanted nucleation-growth leading to the superior monodispersity.

Table 2. Hydrodynamic diameters and polydispersity index (PDI) of the ethanolic dispersions of ZnOCFS, ZnOB, and ZnOMW nanopowders

	CFP		Batch		MW-assisted synthesis	
	Hydrodynamic size (nm)	PDI	Hydrodynamic size (nm)	PDI	Hydrodynamic size (nm)	PDI
Run 1	7.62	0.22	87.34	0.41	26.18	0.29
Run 2	7.66	0.19	73.91	0.50	18.52	0.31
Run 3	8.03	0.21	89.62	0.33	20.84	0.26
Run 4	7.61	0.15	95.74	0.47	24.02	0.28
Run 5	7.85	0.16	77.28	0.45	26.94	0.26
Run 6	7.97	0.21	71.80	0.39	20.60	0.32

4. Conclusions

- The luminescent defect-engineered ZnO nanopowders obtained by CFP, MW-assisted synthesis and batch approach, exhibit Wurtzite crystal structure, phase purity, spherical morphology and uniform size of 4.5 nm, 5.7 nm, and 6.1 nm, respectively. However, the size distribution is narrowest for ZnO_{CFS} NPs, while slight polydispersity is prevalent for ZnO_B.
- The NPs exhibit quantum size effects, pronounced from their blue shifted peak in the absorption spectra. This subsequently resulted in intense yellow-green emission in the visible regime. The peak intensity and the PLQY associated with this oxygen vacancy-mediated emission is the highest for ZnO_{CFS} NPs followed by ZnO_{MW} and ZnO_B NPs.
- A remarkably high BET-specific surface area is determined for ZnO_{CFS} NPs (~247 ± 6 m^2/g). The reduction in the surface area of ZnO_{MW} and ZnO_B NPs depicted agglomeration among the particles in the material systems.
- The stringent regulation on synthesis conditions in CFP resulted in monodispersed particles and lower standard deviations compared to the MW and batch reactors. This signified the enhanced colloidal stability and inter-run reproducibility of nano- ZnO_{CFS}.
- The outcomes elucidated that improved mixing and surface-to-volume ratio in helical coil reactors lead to homogenous heat distribution and shorter nucleation times, facilitating precise nanocrystal size control for scalable production.

Thus, investigation of these concerted effects of varied synthesis processes on defect engineering in functional nanopowders is anticipated to pave newer avenues in the rational design of smart nanostructures.

Acknowledgements

The authors would like to thank SAIF and Department of MEMS, IIT Bombay for providing access to some of the instrumentation facilities. SS acknowledges financial support from the Prime Minister's Research Fellowship scheme (PMRF), Ministry of Higher Education, Government of India.

References

1. Adhikari L, Larm NE, Baker GA. Batch and Flow Nanomanufacturing of Large Quantities of Colloidal Silver and Gold Nanocrystals Using Deep Eutectic Solvents. *ACS Sustainable Chemistry & Engineering;* 2020;8(39):14679-89.
2. Fernández-Maza C, Fallanza M, Gómez-Coma L, Ortiz I. Performance of continuous-flow micro-reactors with curved geometries. Experimental and numerical analysis. *Chemical Engineering Journal;* 2022;437:135192.

3. Zhang K, Gao Y, Pinho B, Hoye RL, Stranks SD, Torrente-Murciano L. The importance of transport phenomena on the flow synthesis of monodispersed sharp blue-emitting perovskite CsPbBr3 nanoplatelets. *Chemical Engineering Journal;* 2023;451:138752.
4. Sarkar S, Debnath SK, Srivastava R, Kulkarni AR. Continuous flow scale-up of biofunctionalized defective ZnO quantum dots: A safer inorganic ingredient for skin UV protection. *Acta Biomaterialia;* 2022;147:377-90.
5. Ngoensawat U, Parnsubsakul A, Kaitphaiboonwet S, Wutikhun T, Sapcharoenkun C, Pienpinijtham P, Ekgasit S. Luminescent nanohybrid of ZnO quantum dot and cellulose nanocrystal as anti-counterfeiting ink. *Carbohydrate Polymers;* 2021;262:117864.
6. Asok A, Deshlahra P, Ramachandran AM, Kulkarni AR. Multifunctional Photostable Nanocomplex of ZnO Quantum Dots and Avobenzone via the Promotion of Enolate Tautomer. *Global Challenges;* 2018;2(11):1800025.

EFFECT OF PREHEAT TEMPERATURE ON COMPACTION OF MACHINED AA2024 SWARF

N S Anas[a,*], K N Ramteke[a], R Anil Kumar[a], K I Raju[a], VNSUV Ammu[a], R N Chouhan[a], A Agnihotri[a], R Radhakrishnan[b]

[a]Jawaharlal Nehru Aluminium Research Development and Design Centre (JNARDDC), Nagpur, India.

[b] Tata Advanced Systems Limited (TASL), MIHAN, Nagpur, India.

Abstract: *Machining of aluminium components generates huge volume of swarf in aerospace and automotive industries. When swarf is recycled via conventional method of remelting, the melt losses are relatively higher, i.e., approximately 10-20 % of aluminium is lost due to oxidation, splashes etc. As an alternative, solid-state or direct recycling of aluminium swarf (chips, turnings, borings etc.) is being developed at JNARDDC, which includes cleaning, compaction of chips and extrusion of compacted billets. The present study investigates the effect of solvents on cleaning of AA2024 machining swarf and the effect of preheat temperature on the density and macrostructure of its compacted specimen. The as-received swarf, collected from an aerospace component manufacturing company, was cleaned in an ultrasonic cleaner for 30 min using different solvents like de-mineralized water, acetone and ethanol to remove coolant, lubricant oil and dirt residue from surface of chips. Based on the analysis of the residue content in the cleaned solutions, it is observed that acetone cleans better than the other two solutions. Compaction of cleaned chips was carried out at preheat temperatures ranging from 250 to 400˚C to evaluate the percentage densification and the mechanical swarf-swarf bonding among chips. The density increased from 54 to 77% as that of the density of AA2024 with increase in temperature. Further studies are in progress to improve the densification of compacted specimens.*

Keywords: *Solid state recycling; Aluminium swarf recycling; Solid waste management; Machined chips; Microstructure.*

1. Introduction

Aluminium and its alloys are being extensively used in various sectors including power transmission, automotive,aerospace, defence, medical and construction industries. Owing to its increased usage andon account of the properties of aluminiumsuch as high specific strength, corrosion resistance, conductivity, non-magnetic, formability and excellentrecyclability the average consumption of aluminium is projected to increase 4% per year over the coming decades [1,2]. It is well-known that the production of primary aluminium is by the Hall-Heroult process, which is highlyenergy-intensive. On the other hand, the energy required for aluminium recycling and corresponding GHG emissions are estimated to be 95% lesser when compared to primary aluminium production[3]. The present industrial practice in aluminium recycling consists of cleaning, drying,compaction, melting, molten metal treatment and ingot production. However, there are relatively higher melt lossesduring conventional recycling of aluminium swarf/chips as nearly 10-20% of aluminium is lost due to oxidation,splashes, being trapped in the filtration system etc. Even with all possible efforts, this melt lossduring the aluminium swarf could not be completely avoided. As an alternative, solid-state or direct recycling of aluminium swarf (chips,turnings, borings etc.) is economical and leaves a lower carbonfootprint as compared to the conventional melting of aluminium chips.

The solid-state conversion of aluminium alloy machining chips into products by hot extrusion was first patented by Stern, as a method to address the issue of melt loss during remelting of aluminium chips. Since aluminium chips are naturally covered by an oxide layer, plastic deformation and compressive stresses should be high enough to break the oxide layers and to enable contact between surfaces of pure metal[4,5]. Wojciech et al., compacted AA6060 aluminiumalloy chips into billets using three techniques for powder extrusion and found that the higher density is obtained for compacts prepared by multi-layer compaction technique[6].Kadir et al., produced AA6061 alloy matrix composites from AA6061 chips, SiC particles (2.5, 5 and 7.5 wt.%) and Alpowder (10, 30 and 50 wt.%) by the cold pressing and sintering. They could attain the density of sample AA6061/10Al powder near totheoretical at 2.43 g/cm^3 and highest hardness of 61.0 HV [7].

Even though thecompaction and consolidation of aluminium alloy powders are available in the existing literature[8–10], extensive studies on the compaction of aluminium alloy machined swarf are scarce. The present study investigates the effect of solvents on the cleaning of AA2024 machining swarf and the effect of preheat temperature on the AA2024 machining swarf compaction.

2. Experimental procedure

AA2024 swarf generated during the lathe machining of components was collected from Tata Advanced Systems Ltd., India,an aerospace production shop floor.Fig. 1 shows the swarf in as-received condition, whichwas long and non-uniform in size. The swarf was subjected to crushing and grinding to make a uniform size that can sieve through standard US Mesh 3. Since lubricants and coolants are used for machining the components, these oils and dirt residues mightalso have adhered to the generated swarf. To clean the swarf, three different solutions i.e., de-mineralized (DM) water (Commercial grade with pH 6.90), ethanol (AR grade)and acetone(AR grade) were utilized for agitation in a 50 L ultrasonic cleaner. To optimise the cleaning solvent, 100 grams of AA2024 swarfimmersed in 200 ml of each of the cleaning solvents and ultrasonicated for 30 mins. After ultrasonication,

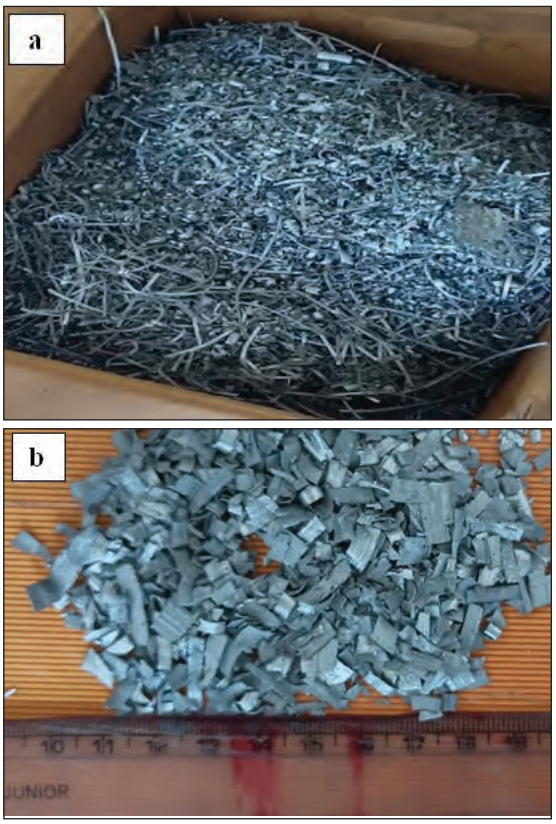

Fig. 1 (a) As-received AA2024 swarf (b) Crushed AA2024 swarf

the AA2024 swarf was filtered out, and the residue solid content analysis was carried out as per IS 82 standard. The cleaned AA2024 swarf was also analysed using ICP-OES (Thermo scientific, ICAP 7000, USA) to determine the elemental composition.

Cleaned and dried AA2024 swarf was filled in a cast iron mould as shown in Fig. 2.The outer dimension of the mould is 80 X 80 mm X 250mm and the inner diameter is 60mm, while the MS plate of 120 X 120 X 30mm is fastened to the base of the mould.A round bar of 59 mm in diameter and 270 mm long made from EN 24 was used as a punch for compaction. AA2024 swarf was compacted at ambient temperature as well as different preheat temperatures ranging from 250-400°C for a duration of 1 hand bulk density was determined. Compacted specimens were characterized using scanning electron microscope(SEM: IT-300, JEOL, USA).

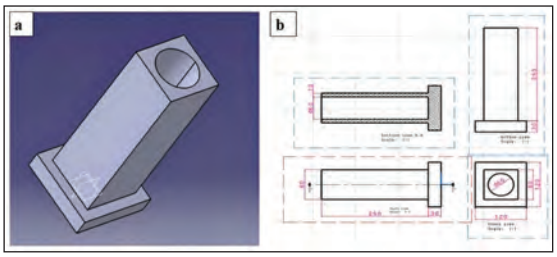

Fig. 2 CAD model of mould (a) 3D and (2) 2D projections

3. Results and discussion

3.1 Swarf characterisation

The chemical composition analysis is given in Table 1. It is clear that the elemental composition is within the range and conformance with standard AA2024. The morphology of AA2024 swarf is shown in Fig. 3(a-b). It is observed that the surface of the swarf exhibited a striation-like structure due to plastic deformation, strain hardening and subsequent breakage of the layer during machining. When observed at a higher magnification, Fig. 3(b), it can be understood these are the severely deformed areas that lead to initiating points for the swarfbreakage to smaller pieces.

Table. 1. Chemical composition of cleaned AA2024 swarf.

Al alloy grade	Cu (%)	Mg (%)	Mn (%)	Fe (%)	Al (%)
Standard AA2024	3.80-4.90	1.20-1.80	0.30-0.90	0.50	Rem.
Analyzed AA2024 chips	4.14 ± 0.07	1.8 ± 0.04	0.63 ± 0.01	0.19 ± 0.04	Rem.

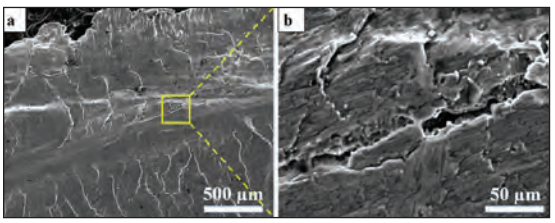

Fig. 3 Morphology of swarf (a) 50 X and (b) 450 X magnifications

3.2 Cleaning solvent optimisation

De-mineralized (DM) water, ethanol and acetone were taken as cleaning solvents ofswarf, which was ultrasonicated.Due to the cleaning action, the initially transparent solutions changed to dark colour. It was visually observed that the swarf-cleaned acetone is darkest among the three solvents, followed by ethanol and DM water. Residue solid content analysis in the cleaned solventsis shown in Fig. 5. Based on the analysis, residue content present in DM water, ethanol and acetone werefoundto be 178, 3620,and 3714mg/L respectively. This indicatesthat acetone cleans better than the other two solutions.

The carbon content present in each solution is analyzed to understand acetone's slightly better performance than ethanol. Clearly, the carbon content in acetone (62%) is higher than that of ethanol (52%). Hence for the same volume taken, acetone cleans swarf better than ethanol. To optimize the soaking duration for cleaning, swarf was immersed in acetone ranging from 10 to 120 mins. By observing Fig. 6, it is understood that the cleaning of swarf in acetone is optimized for 30 mins as a higher duration will not have any significant change and moreover, it will lead to longer processing time.

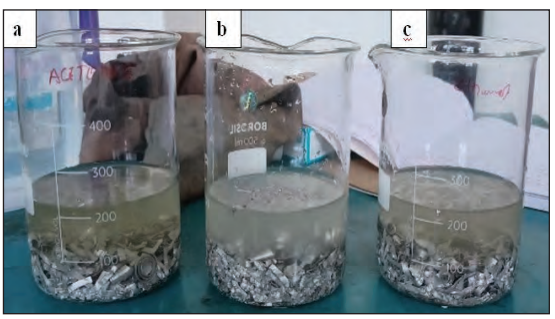

Fig. 4 After cleaning in ultrasonic cleaner (a) Acetone, (b) DM water and (c) Ethanol

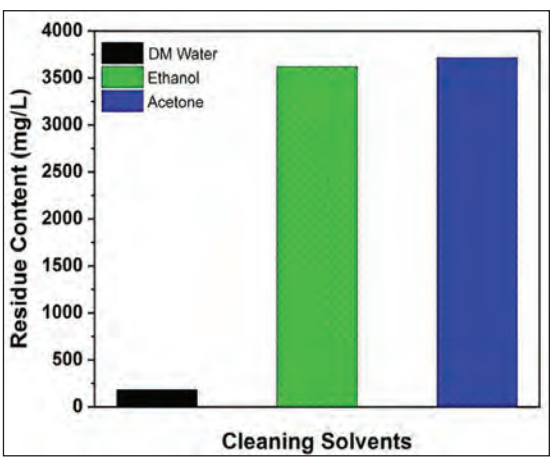

Fig. 5 Residue content analysis of cleaning solvents

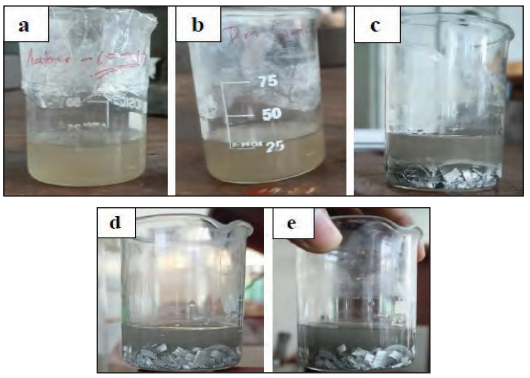

Fig. 6 Soaking of AA2024 swarf for durations: (a) 10 mins, (b) 20 mins, (c) 30 mins, (d) 60 mins and (e) 120 mins

3.3 Compaction of AA2024 swarf

Initially, the acetone-cleaned as-received AA2024 swarf was attempted for compaction at room temperature. No bonding between the swarf was observed as the swarf got disintegrated during handling. Hence, heating of the swarf was employed at 250 °C to soften it and to have a bonding of the swarf. A sample of 60 mm diameter and 48 mm long was obtained. A briquette-kind of bonding between the swarfthat corresponds to 47% density as that of standard AA2024 was obtained. In this specimen, porosity is observed mainly due to non-uniform size of machining chips. Hence, it was understood that the uniform size and shape of the machining swarf playan important role in the compaction process. Subsequently, another compaction at 250°C was attempted using crushed swarf instead of the as-received swarf. This led to improved densification (Fig. 7) asthe particle size of the swarf was maintained nearly uniform prior to compaction.

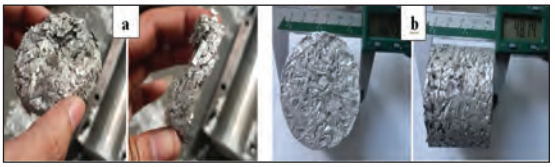

Fig. 7 Compaction of swarf in as-received condition (a) without heating and (b)with preheat at 250 ˚C

Subsequent compactions were carried out on crushed swarf at different temperatures ranging from 250 – 400 °C and the as-compacted bulk specimens are shown in Fig. 8. It was observed that the densification of compacted specimensincreased with an increase in temperature.During compaction, the distance between the adjacent swarf particles reduces as the swarf tries to occupy the vacant spaces. Once the swarf particles come in contact during compaction, the surface oxide layer of the swarf gets broken due to friction at the interface. Simultaneously, metal surfaces get exposed and resulting in the mechanical bonding between swarf particles. Even though at a higher temperature the oxide layer would be thicker than the cold condition, the softening and severe plastic deformation of swarf particles are higher and correspondingly the metal-to-metal contact surface area is also higher. This leads to the increased bulk density at 400 ˚C. The calculated densities of compacts are tabulated in Table 2.

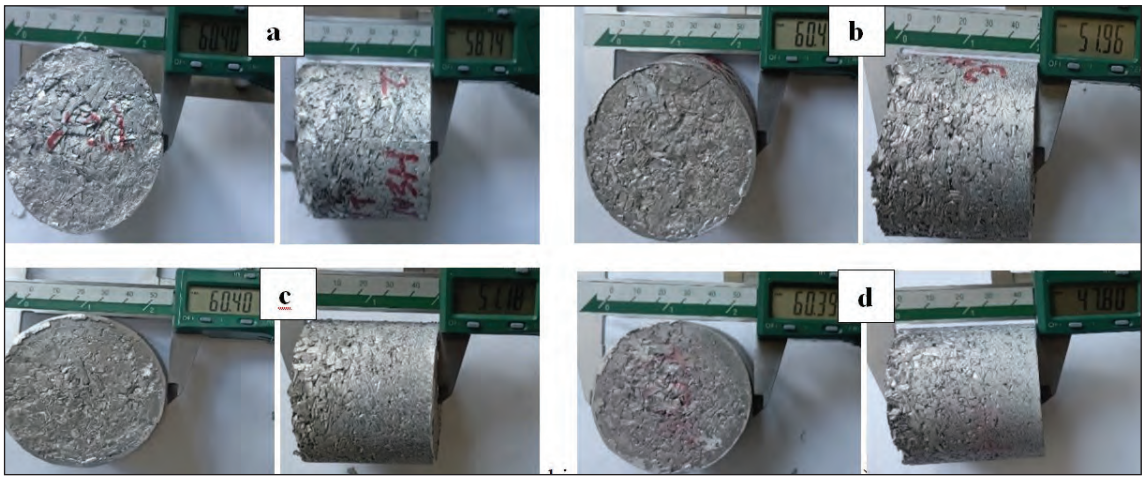

Fig. 8 Compacted specimens using crushed & cleaned chips at preheat temperatures: (a) 250 °C, (b)300 °C, (c) 350 °C and (d) 400 °C, in top and side views.

Sl. No.	Condition of AA 2024 swarf	Preheat temp.	Compacted density, g/cc	% Compacted density w.r.t AA2024
1	As-received & cleaned chips	No preheat	Not compacted	--
2	As-received & cleaned chips	250 ˚C	1.30	47%
3	Crushed & cleaned chips	250 ˚C	1.59	55%
4	Crushed & cleaned chips	300 ˚C	1.66	59%
5	Crushed & cleaned chips	350 ˚C	1.93	69%
6	Crushed & cleaned chips	400 ˚C	2.14	77%

Table 2. Compacted specimen density with respect to preheat temperature

To understand the macrostructure of compacted specimenspreheated at 350 ˚C and 400 ˚C, the morphology at the entire diameter was analysed across thecross-sectionalarea of the specimen segment, Fig. 9. It was observed that the compaction is not homogenous and samples exhibited similar compaction behaviour for both the conditions i.e., higher compaction at both the edges and poor at the centre portion. This can be attributed to the difference in restriction offered to swarf particles at the edges and centre portions. At the edge, the movement of swarf particles is completely restricted by the die wallon one side. This leads to more friction between the swarf particles resulting in more rupturing of oxide layer and metal-to-metal bonding. However, in the case of swarf particles at the centre, the restriction offered to swarf particles' movement during compaction is much less, hence lead to lesser bonding. Delamination of swarf particles was also observed only at the centre but not on edges due to the same reason.

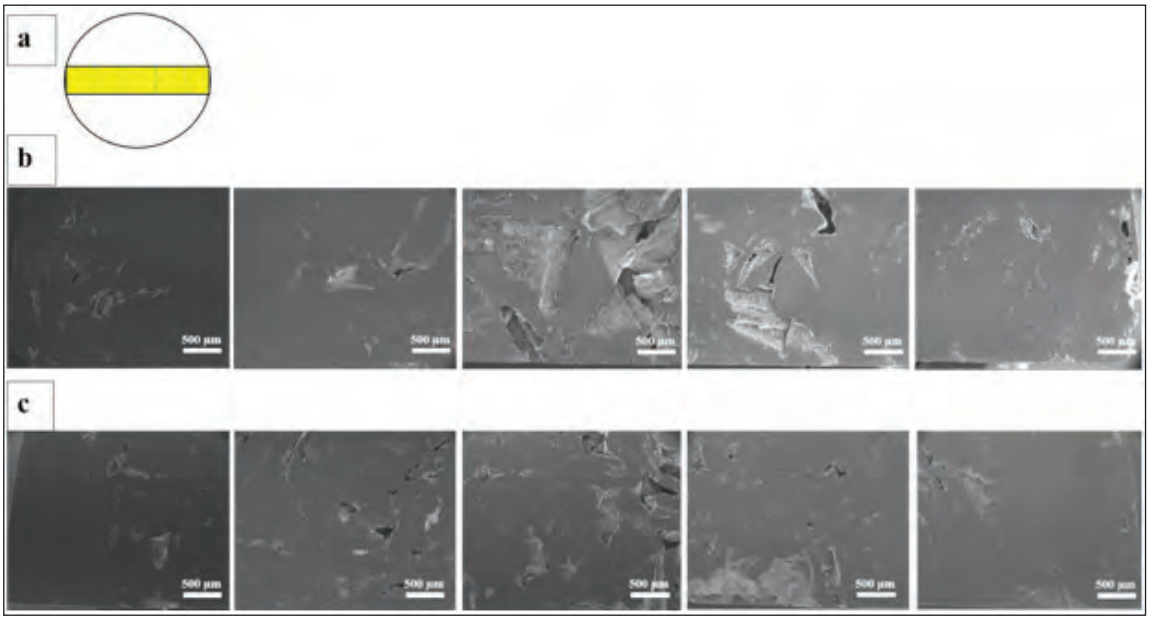

Fig. 9(a) Schematic of sample segments used for SEM, (b) SEM images of compaction at preheat temperature of (b)350 ˚C and (c) 400 ˚C, in cross-section as per schematic (a).

4. Conclusions

The study investigated two aspects of solid state recycling of machined AA2024 swarf. Firstly, the effect of cleaning solvents i.e., DM water, ethanol and acetone on cleansing action of swarf were investigated or anlaysed. Based on the residue content analysis, acetone was found to be the best cleaning solvent among the three solvents attempted in this study. Also, the time duration for cleaning of swarf with acetone was found to be optimum at 30 mins. Secondly, the compaction of swarf was carried out at room temperature and various preheat temperatures ranging from 250-400 ˚C. Compaction attempt on as-received

swarf at room temperature did not show any bonding as it was completely disintegrated; but at a preheat temperature of 250 ˚C, the swarf was slightly better compacted. The density of swarf was further increased from 54% to 77% when the swarf was crushed to a uniform size and compacted from 250-400 ˚C. From the macro and microstructural details, the compaction was observed to be inhomogeneous and the edges of the samples exhibited better compaction than that of the centre. Further studies are required to improve the compaction density to use the compacted swarf for extrusion applications.

5. Acknowledgements

The authors would like to thank the Science and Technology Division, Ministry of Mines for funding the project. Support received from Mr Pravin, Mr Dilip and Mr Vijay in carrying out compaction trials was acknowledged.

6. References:

1. I. Polmear, D. St. John, J.-F. Nie, M. Qian, Light Alloys, in: 5th ed., Butterworth-Heinemann, Boston, 2017: pp. 1–29. https://doi.org/https://doi.org/10.1016/B978-0-08-099431-4.00001-4.
2. J.R. Davis, Aluminum and aluminum alloys,ASM International handbook committee, ASM International, Materials Park, OH, USA, 1993.
3. M.E. Schlesinger, Aluminum Recycling, CRC Press, Taylor & Francis Group, New York, 2007.
4. W. Chmura, Z. Gronostajski, Bearing composites made from aluminium and aluminium bronze chips, J. Mater. Process. Technol. 178 (2006) 188–193. https://doi.org/https://doi.org/10.1016/j.jmatprotec.2006.03.156.
5. J. Gronostajski, W. Chmura, Z. Gronostajski, Phases created during diffusion bonding of aluminium and aluminium bronze chips, J. Achiev. Mater. Manuf. Eng. 19 (2006) 32–37.
6. W.Z. Misiolek, M. Haase, N. Ben Khalifa, A.E. Tekkaya, M. Kleiner, High quality extrudates from aluminum chips by new billet compaction and deformation routes, CIRP Ann. 61 (2012) 239–242. https://doi.org/https://doi.org/10.1016/j.cirp.2012.03.113.
7. M.I.A. Kadir, M.S. Mustapa, M.R. Ibrahim, M.A. Samsi, A.S. Mahdi, Microstructures and characteristics of solid state recycling aluminium chips AA6061/Al-SiC composites fabricated by cold compaction method, AIP Conf. Proc. 1846 (2017) 20005. https://doi.org/10.1063/1.4983586.
8. N.S. Anas, M. Ramakrishna, R.K. Dash, T.N. Rao, R. Vijay, Influence of process control agents on microstructure and mechanical properties of Al alloy produced by mechanical alloying, Mater. Sci. Eng. A. 751 (2019) 171–182. https://doi.org/10.1016/j.msea.2019.02.060.
9. D. Jeyasimman, K. Sivaprasad, S. Sivasankaran, R. Narayanasamy, Fabrication and consolidation behavior of Al 6061 nanocomposite powders reinforced by multi-walled carbon nanotubes, Powder Technol. 258 (2014) 189–197. https://doi.org/10.1016/J.POWTEC.2014.03.039.
10. M. Bhouri, F. Mzali, Study of Al 2017 Alloy Prepared by Recycling Method via Powder Metallurgy Route, in: F. Chaari, M. Barkallah, A. Bouguecha, B. Zouari, M.T. Khabou, M. Kchaou, M. Haddar (Eds.), Adv. Mater. Mech. Manuf., Springer International Publishing, Cham, 2020: pp. 9–16.

POWDER METALLURGICAL PROCESSING OF ALUMINIUM REINFORCED WITH NOVEL W-BASED DISPERSOIDS

Debashish Mohanta[a], Manas Mukherjee[b], Srikant Gollapudi[a*]

[a]School of Minerals, Metallurgical and Materials Engineering, IIT Bhubaneswar, India.

[b]Metal Foams and Porous Materials Lab, Department of Metallurgical and Materials Engineering, Indian Institute of Technology Madras, Chennai, India.

Abstract: *Powders of W mixed with Ti were ball milled for 6 hours in a hardened steel vial. Contamination with Fe from the milling media resulted in a W-Ti-Fe alloy instead of the desired W-20 at.% Ti alloy.The as-milled powder bearing a grain size of 7 nm was used for reinforcing aluminium using the cold pressing and sintering method. For comparison purposes,Al composites containing Was reinforcement were also prepared. Analysis of the sintered compacts using SEM-EDS and XRD revealed that W particles reacted with Al to form $Al_{12}W$ intermetallic compound in the case of the Al-W composite. However, in the case of the Al-WTiFe composite, not all of the W-Ti-Fe particles got converted into the $Al_{12}W$ intermetallics. This was attributed to the difference in average particle size of W andW-Ti-Fepowders.Additionally, the hardness of the Al rich regions in Al-WTiFe and Al-W composites were observed to be 102 and 84 VHN respectively which is higher than that of pure Al at 30 VHN.*

Keywords: *Aluminium composites; Mechanical alloying; W-based reinforcements; Sintering; Hardness.*

1. Introduction

Aluminium alloys are widely used in aerospace, automobileand defence applications due to their high strength-to-weight ratio[1]–[3]. As pure aluminium is soft and cannot be directly used for structural purposes, it is strengthened by alloying additions and in certain cases by the addition of hard ceramic reinforcements such asSiC [4], TiB_2 [5], TiC[6], Al_2O_3 [7], Al_3Zr [8], etc. to the aluminium matrix [9]. These aluminium metal matrix composites (MMCs) are synthesized through conventional stir casting[10], centrifugal casting[11], squeeze casting[12], and in-situ processes[8], [13]. In conventional melt casting route of fabrication, issues like the non-uniform distribution of reinforcements, chemical reaction between reinforcement and matrix material, wettability etc., are experienced, which adversely affect the mechanical properties of the composite[10], [14], [15].These issues can be overcome in the powder metallurgy route wherein the composite has a homogenous distribution of matrix and reinforcement particles and exhibits high bulk densities after cold compaction and sintering[8], [16]–[19].

Tungsten is an excellent reinforcement because of its high hardness, melting point, stiffness, good chemical stability, corrosion resistance and electrical conductivity[20], [21]. Huang etal. [21] fabricated Al composite with W as reinforcement through friction stir processing (FSP) route. The composite's hardness and strength increased with the number of FSP passes. Feng etal. [22]introduced Al12W as reinforcement in aluminium matrix using in-situ processes. The Al12W was well distributed within the Al matrix and the bonding between Al12W and matrix was also very good. The tensile strength of the Al/ Al12W composite was observed to be greater than that of the pure Al.

Strength of a composite is usually a function of the strength of the reinforcement. The

strength of the metallic reinforcement usually increases with adecrease in the grain size in accordance with the Hall-Petch equation[23]–[26].Nanocrystalline tungsten could be used as a reinforcement for aluminium subject to thermal stability of the nanograined structure during high temperature processing of the composite. Chookajorn and Schuh[27]reported extremely high stability of the nanostructure of W-20 at.%Ti,bearing a grain size of 20 nm. The use of W-Ti system as a reinforcement for aluminium has not been reported before. Hence this work attempts to develop Al composites reinforced with nanostructured W alloy using the powder metallurgy route.

2. Methodology

Elemental powders of aluminium (particle size 15-20 µm, purity > 99.9 %), tungsten (particle size 1-2 µm, purity > 99 %), titanium (particle size 100-150 µm, purity > 99.9 %) as shown in Figure 1a, 1b and 1c respectively were procured from M/s Alfa Aesar.

Ball milling of elemental W and Ti powders mixed in the desired proportion to yield W-20at.% Ti was carried out in a hardened steel (HS) vial with HS balls as the milling media. Prior to milling, the powders were loaded into the vial and sealed under a high-purity argon atmosphere provided by the glove box. For the milling, the ball-to-powder ratio was kept at 5:1. The ball-milling was carried out on the SPEX 8000D high-energy ball mill for a duration of 6 hours. Grain size and phase analysis of milled powders were carried out using the X-ray diffractograms obtained with Cu Kα (λ= 1.54 A˚) radiation usinga Bruker D8 Advance X-ray powder diffractometer (Billerica, United States) operating with a 40 kV voltage and 30 mA current. The diffractograms were analyzed using the X'PertHighscore Plus software. The chemical composition of the milled powders was evaluated through Energy Dispersive Spectroscopy (EDS) technique on

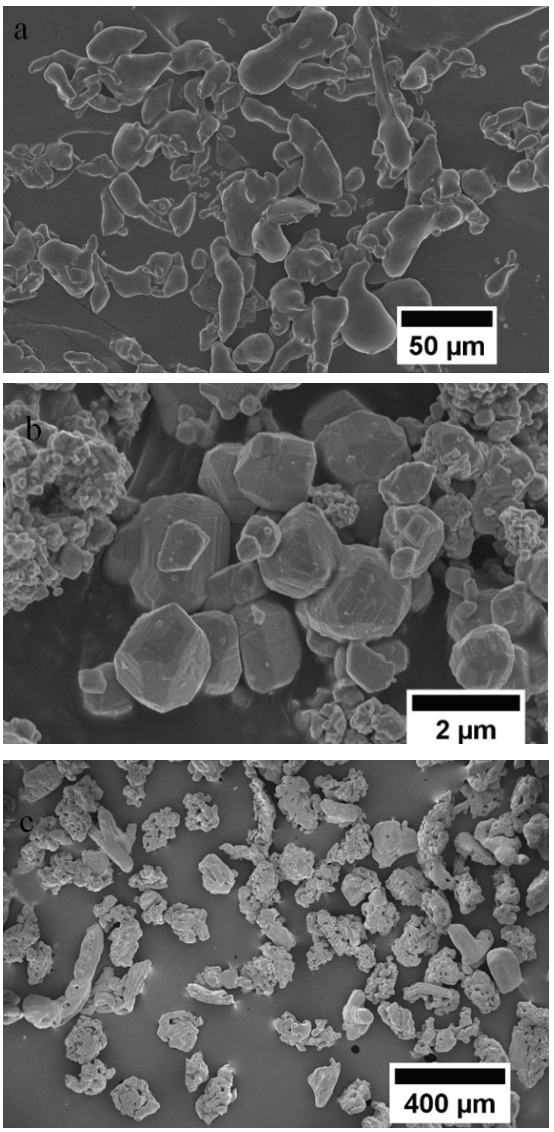

Fig. 1.SEM image of as-received particles of (a) Al, (b) Wand (c) Ti.

a ZEISS Field Emission Scanning Electron Microscope (FESEM). Composite of aluminium and 20 wt.% of the milled powderswas prepared by mixing the individual powders followed by cold compaction at 80 kg/cm^2 pressure in a 10 mm die and sintering at 650 °C for 1 hour in a vacuum atmosphere. For comparison purposes,

a composite of aluminium and pure tungsten was also produced in a similar fashion and this composite is hereafter referred to as Al-20W. The density of the sintered composite pellets was determined and compared to the densities of their respective green counterparts. The sintered pellets were then sequentially ground with grinding papers (600 to 2000 grit size) followed by polishing with diamond paste and colloidal silica to obtain a mirror finish. Subsequently, the samples were studied using a Leica DM I3000M inverted metallurgical microscope to determine the distribution of the reinforcement particles within the aluminium matrix. The phase and microstructural analysis of the sintered composites was also conducted using X-Ray Diffraction and scanning electron microscopy techniques. Hardness measurements were carried out on pure aluminium and the aluminium composite pelletsat a load of 50 gf with a dwell time of 10 seconds using the Zwick-Roell (Indentec) microhardness testing equipment.

3. Results and Discussion

3.1 Characterization of high-energy ball-milled powders

Although our intent was to synthesize W-20at.% Ti powders, the milled powders were found to be heavily contaminated with Fe introduced by the milling media during the high energy ball milling process. The energy dispersive spectroscopy (EDS) analysis of the milled powders suggested the presence of 29.4 at.% Fe in addition to 57.1 at.% W and 13.5 at.% Ti. Hence the ball milled powders are hereafter addressed as W-Ti-Fe powders. Figure 2 provides the

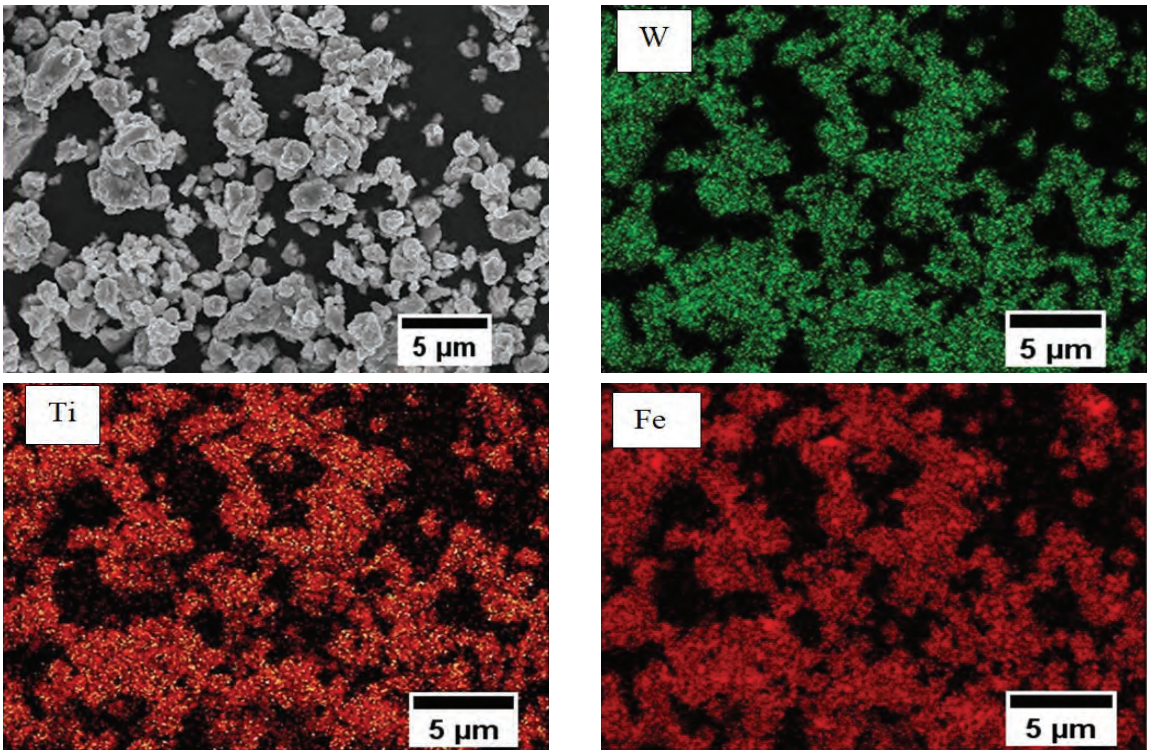

Fig. 2. SEM micrograph andelemental mapping of high energy ball milled W-Ti-Fe.

elemental distribution maps of W, Ti and Fe in the ball milled powders which clearly reveal the presence of a large amount of Fe alloyed with W and Ti.Figure 3 (a) and (b) provides SEM micrographs of the ball milled W-Ti-Fe powders. For comparison sake, we have included the SEM micrograph of the W powders in Figure 3 (c). The SEM micrographs of W and W-Ti-Fe reveal that the W-Ti-Fe powder particles have a mix of coarse and fine particles whereas the W particles are by and large fine. The larger size of the particles of W-Ti-Fe are probably due to cold welding of powder particles brought about by the high energy ball milling process.

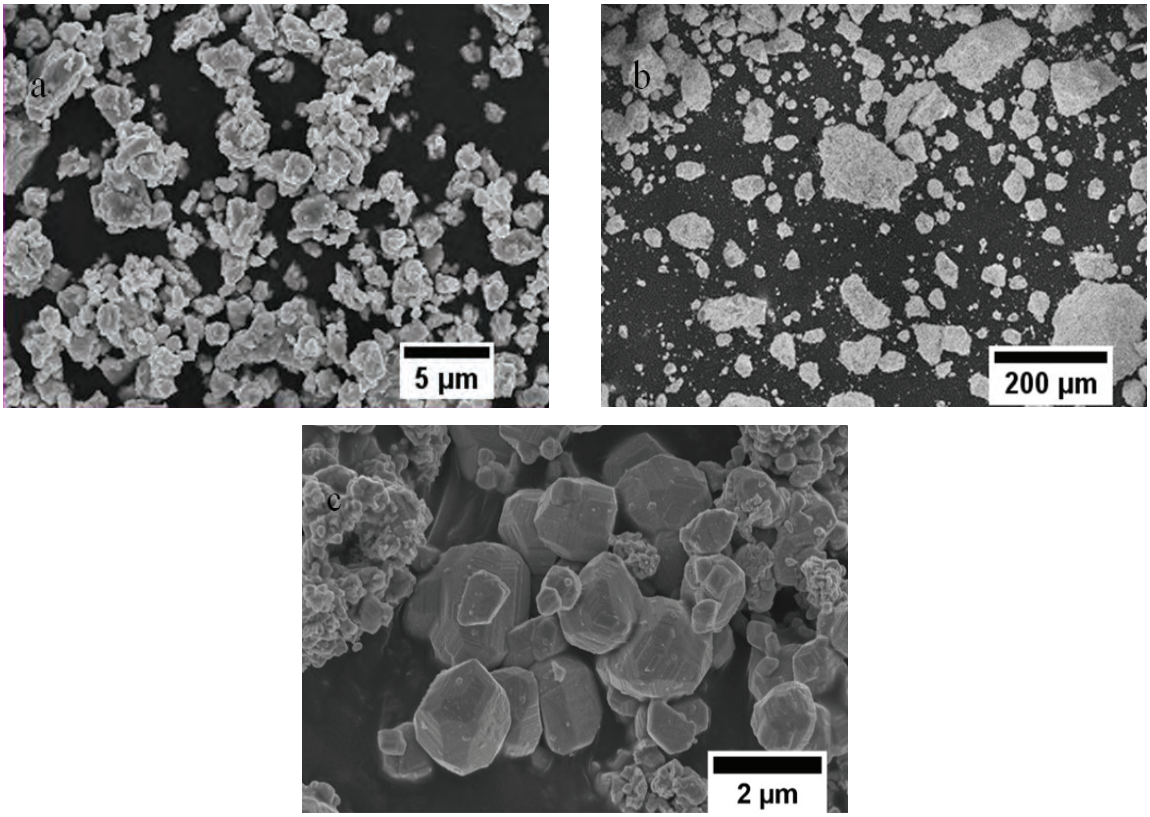

Fig. 3. SEM micrograph of (a) finer and (b) coarser ball milled W-Ti-Fe particles (c) SEM micrograph of unmilledW particles.

The XRD pattern obtained from W-Ti-Fe is shown in Figure 4. The XRD pattern suggests that Ti and Fe are dissolved in the W matrix to form a single phase solid solution. The Williamson-Hall method was used to evaluate the grain size of the W-Ti-Fe and the same was found to be 7nm. For comparison sake, the XRD pattern captured from W powders is also included in Figure 4. The sharp peaks of W in its XRD pattern suggests that the powder does not have a nanocrystalline structure.

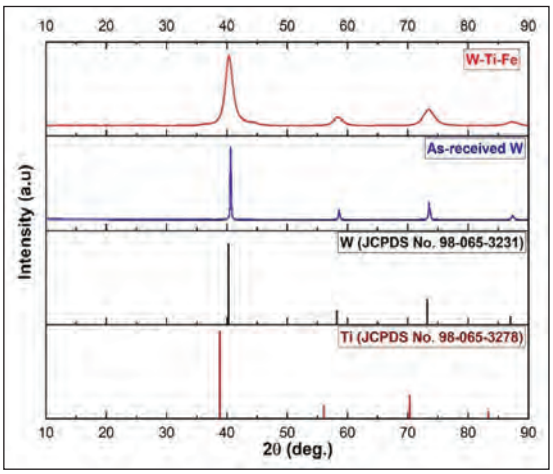

Fig. 4. XRD patterns of high energy ball-milled W-Ti-Fe and as-received W.

3.2 Characterization of sintered composites

The green and sintered densities of the composites of Al-20W and Al reinforced with 20 wt.% of W-Ti-Fe (hereafter referred to as Al-20WTiFe)were determined and the same is reported in Table 1. As shown in Table 1, there is an increase in the density of the compacts following sintering. However, near theoretical densities were not achieved. This implies that the sintering temperature and duration was not sufficient to ensure complete densification.

Table 1. Green and sintered density of Al-20W and Al-20WTiFe

Al-composites	Green Density (%)	Sintered Density (%)
Al-20W	87 ± 1.5	94 ± 3
Al-20WTiFe	87 ± 4	95 ± 1

Optical micrographs of the Al-20W and Al-20W TiFe composites are shown in Figure 5a and 5b, respectively. In Al-20W, the brighter regions belong to the aluminium and the grey regions are the tungsten rich reinforcement regions. The black spots are the pores. Similarly, in the case of Al-20WTiFe, the bright and grey regions correspond to aluminium rich and reinforcement rich regions respectively. The XRD patterns obtained from Al-20W and Al-20WTiFe sintered composites are shown in Figure6a and 6b. Phase analysis reveals that in the case of Al-20W, the W reinforcement has reacted with the Al matrix to form $Al_{12}W$ intermetallic compound. Also, in the case of Al-20WTiFe, the small-sized W-Ti-Fe particles have reacted with the Al matrix to form $Al_{12}W$. However, the larger particles of W-Ti-Fe seem to have not converted fully into $Al_{12}W$ as is evident from the XRD peaks of the residual W-Ti-Fe seen in Figure 6b.

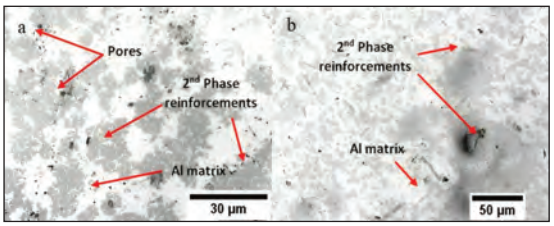

Fig. 5. Optical micrograph of (a) Al-20W and (b) Al-20WTiFe composites.

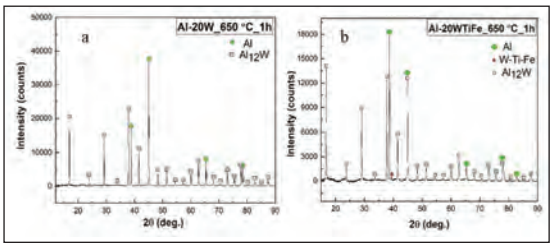

Fig. 6. XRD graphs of (a) Al-20W and (b) Al-20WTiFe composites.

SEM-EDS analysis of Al-20W and Al-20W TiFe composites was carried out to understand the distribution of elements within the composite. The SEM image of Al-20W shown in Figure 7 (a) shows darker regions (Region-1) and bright cluster regions (Region-2). Region-1 is pure-

Alandregion-2 corresponds to Al12W. All the W particles were found to convert into $Al_{12}W$ during sintering at 650°C. Chen et al. [28] and Zhang et al. [29] respectively reported formation of $Al_{12}W$ at 560°C and 550°C for sintering carried out for a duration of 1 hour. Similarly, Ding et al. [30] reported its formation at 680°C during solid-liquid reaction millingof Al and W powders for 24 hours.

In Figure 7 (b) the backscattered electron image (BSE) of Al-20WTiFe is provided. The SEM micrograph depicts bright regions bearing an elemental composition of 56.54 at.% W, 13.30 at.% Ti and 21.48 at.% Fe. These regions basically correspond to unreacted W-Ti-Fe. On the other hand, the greyish regions are Al12W intermetallic compounds bearing an elemental composition of

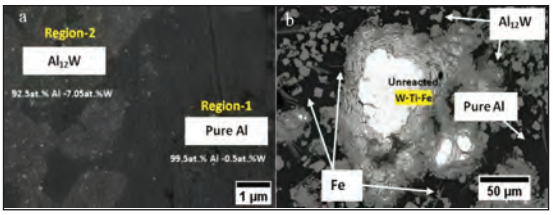

Fig. 7. SEM images of (a) Al-20W and (b) Al-20WTiFe composites.

92.12 at. % Al and 6.89 at. % W. The dark regions belong to the Al matrix. A few needle-like structures,distributed within the matrix, are also observed and these are primarily Ti rich and Fe rich regions. This is validated from the elemental maps shown in Figure 8. This implies that these elements have diffused out of the W-Ti-Fe system during the sintering process. The outward diffusion of Ti and Fe is particularly higher in the case of smaller particles of W-Ti-Fe. Some of the larger particles of W-Ti-Fe had an unreacted core which indicates that the duration chosen for sintering was not sufficient for complete reaction of Al with W-Ti-Fe particles. In the case of the Al-20W composite,the smaller W particles with a higher specific surface area cause rapid reaction between the Al and W particles leading to the formation of $Al_{12}W$.

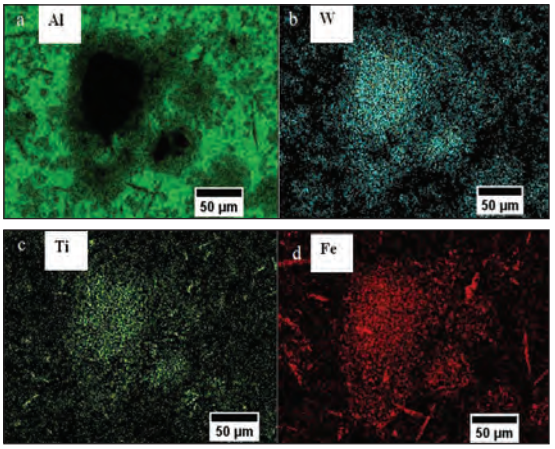

Fig. 8. Elemental mapping of (a) Al, (b) W, (c) Ti and (d) Fe in Al-20WTiFe composite.

Microhardness values of Al rich region in Al-20W and Al-20W TiFe were found to be 84 ± 20VHN and 102 ± 18VHN respectively, which is much higher than the average hardness of nominally pure Alat 30 ± 3 VHN asshown in Figure 9.In the case of the Al-20W composite, the high hardness of the Al rich region is primarily due to the formation of the hard $Al_{12}W$ intermetallic which is known to exhibit a hardness of about 800 VHN. On the other hand, the higher hardness of the Al rich region in the Al-20WTiFe matrix could be due to the presence of the hard W-Ti-Fe reinforcement in addition to the formation of the hard $Al_{12}W$ intermetallic. Future work can focus on studying the characteristics of the W-Ti-Fe phase and the phase transformations the system is undergoing during sintering.

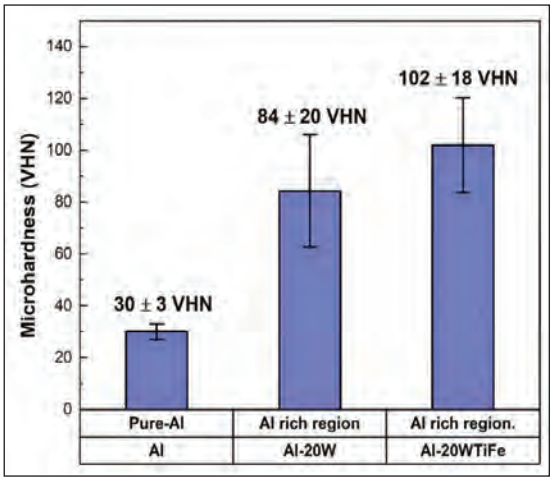

Fig. 9. Microhardness values with indentation images of Al-20W and Al-20WTiFe composites.

4. Conclusion

- Nanocrystalline W-20 at.% Ti was attempted to produce in a high energy ball mill for a duration of 6 hours. However, due to contamination of Fe from milling media, we ended up with nanocrystalline W-Ti-Fe powder with a grain size of 7 nm.
- Al-20W and Al-20WTiFe metal matrix composites weredeveloped using the conventional press and sinter method.
- In both the composites upon sintering at 650°C for 1h, Al12W intermetallic compound wasfound to form.
- In Al-20W, all W was converted to Al12W intermetallic compound. However, in Al-20WTiFe, unreacted W-Ti-Fewas observed in the core of the particles. This was due to the coarser particle size of W-Ti-Fe vis-à-vis the W particles.
- The hardness of the Al rich regions in Al-WTiFe and Al-W composites were observed to be 102 and 84 VHN respectively which is higher than that of pure Al at 30 VHN.

Reference

1. A. Bouzekova-Penkova and A. Miteva, "Some Aerospace Applications of 7075 (B95) Aluminium Alloy," *Aerosp. Res. Bulg.*, vol. 34, pp. 165–179, 2022, doi: 10.3897/arb.v34.e15.
2. S. T. Mavhungu, E. T. Akinlabi, M. . Onitiri, and F. M. Varachia, "Aluminum Matrix Composites for Industrial Use: Advances and Trends," *Procedia Manuf.*, vol. 7, pp. 178–182, 2017, doi: 10.1016/j.promfg.2016.12.045.
3. P. V. Kumar, G. M. Reddy, and K. S. Rao, "Microstructure, mechanical and corrosion behavior of high strength AA7075 aluminium alloy friction stir welds e Effect of post weld heat treatment," *Def. Technol.*, pp. 4–11, 2015, doi: 10.1016/j.dt.2015.04.003.
4. M. H. Rahman and H. M. M. Al Rashed, "Characterization of silicon carbide reinforced aluminum matrix Composites," *Procedia Eng.*, vol. 90, pp. 103–109, 2014, doi: 10.1016/j.proeng.2014.11.821.
5. S. Natarajan, R. Narayanasamy, S. P. K. Babu, G. Dinesh, B. A. Kumar, and K. Sivaprasad, "Sliding wear behaviour of Al 6063 / TiB 2 in situ composites at elevated temperatures," *Mater. Des.*, vol. 30, no. 7, pp. 2521–2531, 2009, doi: 10.1016/j.matdes.2008.09.037.
6. P. Li, E. G. Kandalova, and V. I. Nikitin, "In situ synthesis of Al-TiC in aluminum melt," *Mater. Lett.*, vol. 59, no. 19–20, pp. 2545–2548, 2005, doi: 10.1016/j.matlet.2005.03.043.
7. M. F. Zawrah and M. H. Aly, "In situ formation of Al_2O_3-SiC-mullite from Al-matrix composites," *Ceram. Int.*, vol. 32, no. 1, pp. 21–28, 2006, doi: 10.1016/j.ceramint.2004.12.005.
8. B. Kaveendran, G. S. Wang, L. J. Huang, L. Geng, and H. X. Peng, "In situ (Al_3Zr + Al_2O_3np)/2024Al metal matrix composite with novel reinforcement distributions fabricated by reaction hot pressing," *J. Alloys Compd.*, vol. 581, pp. 16–22, 2013, doi: 10.1016/j.jallcom.2013.06.143.
9. P. Mukhopadhyay, "Alloy Designation, Processing, and Use of AA6XXX Series Aluminium Alloys," *Int. Sch. Res. Netw. Metall.*, vol. 2012, no. Table 1, pp. 1–15, 2012, doi: 10.5402/2012/165082.

10. H. Kala, K. K. S. Mer, and S. Kumar, "A Review on Mechanical and Tribological Behaviors of Stir Cast Aluminum Matrix Composites.," *Procedia Mater. Sci.*, vol. 6, no. Icmpc, pp. 1951–1960, 2014, doi: 10.1016/j.mspro.2014.07.229.

11. J. Zhang, Y. Wang, B. Zhou, and X.-Q. Wu, "Functionally graded Al/Mg2Si in-situ composites, prepared by centrifugal casting," *J. Mater. Sci. Lett.*, vol. 17, pp. 1677–1679, 1998.

12. C. Kaynak and S. Boylu, "Effects of SiC particulates on the fatigue behaviour of an Al-alloy matrix composite," *Mater. Des.*, vol. 27, no. 9, pp. 776–782, 2006, doi: 10.1016/j.matdes.2005.01.009.

13. S. L. Zhang et al., "A novel fabrication technology of in situ TiB2/6063Al composites: High energy ball milling and melt in situ reaction," *J. Alloys Compd.*, vol. 639, pp. 215–223, 2015, doi: 10.1016/j.jallcom.2015.03.156.

14. R. Sharma, S. Jha, K. Kakkar, K. Kamboj, and P. Sharma, "A Review of the Aluminium Metal Matrix Composite and its Properties," *Int. Res. J. Eng. Technol.*, pp. 832–842, 2017.

15. P. Sahoo and M. J. Koczak, "Analysis of in situ formation of titanium carbide in aluminum alloys," *Mater. Sci. Eng. A*, vol. 144, no. 1–2, pp. 37–44, 1991, doi: 10.1016/0921-5093(91)90207-4.

16. G. Manohar, A. Dey, K. M. Pandey, and S. R. Maity, "Fabrication of Metal Matrix Composites by Powder Metallurgy : A Review," *Am. Inst. Phys.*, 2018, doi: 10.1063/1.5032003.

17. C. Nazık, N. Tarakçıoğlu, S. Özkaya, F. Erdemır, and A. Çanakçı, "Investigation and Testing of Mechanical Properties of Al-Nano SiC Composites through Cold Isostatic Compaction Process," *Int. J. Mater. Mech. Manuf.*, vol. 4, no. 4, pp. 251–254, 2016, doi: 10.18178/ijmmm.2016.4.4.266.

18. D. Wang, H. Wang, S. Sun, X. Zhu, and G. Tu, "Fabrication and characterization of TiB2/TiC composites," *Int. J. Refract. Met. Hard Mater.*, vol. 45, pp. 95–101, 2014, doi: 10.1016/j.ijrmhm.2014.03.004.

19. E. Mohammad Sharifi, F. Karimzadeh, and M. H. Enayati, "Synthesis of titanium diboride reinforced alumina matrix nanocomposite by mechanochemical reaction of Al-TiO2-B2O3," *J. Alloys Compd.*, vol. 502, no. 2, pp. 508–512, 2010, doi: 10.1016/j.jallcom.2010.04.207.

20. C. Y. Liu et al., "Effect of W particles on the properties of accumulatively roll-bonded Al / W composites," vol. 547, pp. 120–124, 2012, doi: 10.1016/j.msea.2012.03.095.

21. G. Huang, Y. Shen, R. Guo, and W. Guan, "Fabrication of tungsten particles reinforced aluminum matrix composites using multi-pass friction stir processing: Evaluation of microstructural, mechanical and electrical behavior," *Mater. Sci. Eng. A*, vol. 674, pp. 504–513, 2016, doi: 10.1016/j.msea.2016.07.124.

22. Y. C. Feng, L. Geng, A. B. Li, and Z. Z. Zheng, "Fabrication and characteristics of in situ Al12W particles reinforced aluminum matrix composites by reaction sintering," *Mater. Des.*, vol. 31, no. 2, pp. 965–967, 2010, doi: 10.1016/j.matdes.2009.08.021.

23. S. Cheng, J. A. Spencer, and W. W. Milligan, "Strength and tension / compression asymmetry in nanostructured and ultrafine-grain metals," *Acta Mater.*, vol. 51, pp. 4505–4518, 2003, doi: 10.1016/S1359-6454(03)00286-6.

24. M. Dao, L.Lu, R. J. Asaro, J. T. M. De Hosson, and E.Ma, "Toward a quantitative understanding of mechanical behavior of nanocrystalline metals," *Acta Mater.*, vol. 55, no. 143, pp. 4041–4065, 2007, doi: 10.1016/j.actamat.2007.01.038.

25. F. D. Di Tolla and K. W. Jacobsen, "Softening of nanocrystalline metals at very small grain sizes," *Nature*, vol. 391, pp. 561–563, 1998.

26. K. V. Rajulapati, R. O. Scattergood, K. L. Murty, Z. Horita, T. G. Langdon, and C. C. Koch, "Mechanical properties of bulk nanocrystalline aluminum-tungsten alloys," *Metall. Mater. Trans. A Phys. Metall. Mater. Sci.*, vol. 39, no. 10, pp. 2528–2534, 2008, doi: 10.1007/s11661-008-9593-3.

27. T. Chookajorn and C. A. Schuh, "Nanoscale segregation behavior and high-temperature stability of nanocrystalline W-20 at.% Ti," *Acta Mater.*, vol. 73, pp. 128–138, 2014, doi: 10.1016/j.actamat.2014.03.039.

28. P. Chen, G. Luo, Y. Liu, Q. Shen, and L. Zhang, "Fabrication of Al-W functionally graded impact material via vacuum hot-pressing sintering method," *J. Phys. Conf. Ser.*, vol. 419, no. 1, 2013, doi: 10.1088/1742-6596/419/1/012010.

29. H. Zhang, P. Feng, and F. Akhtar, "Aluminium matrix tungsten aluminide and tungsten reinforced composites by solid-state diffusion mechanism," *Sci. Rep.*, vol. 7, no. May, pp. 1–8, 2017, doi: 10.1038/s41598-017-12302-w.

30. C. Ding, C. Zhang, C. Jianguo, and C. Zhenhua, "Preparation of W – Al intermetallic compound powders by a mechanochemical approach," vol. 461, pp. 2007–2009, 2008, doi: 10.1016/j.jallcom.2007.07.058.

31. H. X. Xue et al., "Bulk nanocrystalline W-Ti alloys with exceptional mechanical properties and thermal stability," *J. Mater. Sci. Technol.*, vol. 114, pp. 16–28, 2022, doi: 10.1016/j.jmst.2021.11.015.

32. R. O. Scattergood, C. C. Koch, K. L. Murty, and D. Brenner, "Strengthening mechanisms in nanocrystalline alloys," *Mater. Sci. Eng. A*, vol. 493, pp. 3–11, 2008, doi: 10.1016/j.msea.2007.04.132.

33. B. B. Q. Han and E. J. Lavernia, "Deformation Mechanisms of Nanostructured Al Alloys **," *Adv. Eng. Mater.*, vol. 7, no. 6, pp. 457–465, 2005, doi: 10.1002/adem.200400219.

34. T. J. Rupert, J. C. Trenkle, and C. A. Schuh, "Enhanced solid solution effects on the strength of nanocrystalline alloys," *Acta Mater.*, vol. 59, no. 4, pp. 1619–1631, 2011, doi: 10.1016/j.actamat.2010.11.026.

35. C. A. Schuh, T. G. Nieh, and H. Iwasaki, "The effect of solid solution W additions on the mechanical properties of nanocrystalline Ni," *Acta Mater.*, vol. 51, pp. 431–443, 2003, doi: 10.1016/S1359-6454(02)00427-5.

THERMAL CONDUCTIVITY OF ALUMINA - ZIRCONIUM DIBORIDE COMPOSITE

Jyothi Sharma[*1,2], P.K. Patro[1,2], Deep Prakash[1,2], Amit Sinha[1,2], T. Mahata[1,2]

[1]Powder Metallurgy Division, Bhabha Atomic Research Centre,Vashi Complex, Navi Mumbai, India.

[2]Homi Bhabha National Institute, Anushaktinagar, Mumbai, India.

Email Id: jyothis@barc.gov.in

Abstract: *In this work, the effect of ZrB_2 addition on thermal conductivity of alumina ceramic has been studied. The dispersing phase ZrB_2 has been varied from 5wt% to 30wt% in alumina matrix. All composition has been densified by vacuum hot pressing. ZrB_2 powder was prepared inhouse by carbothermic reduction of ZrB_2 in presence of B_4C. The median particle sizes of Al_2O_3 and ZrB_2 were 4.4 µm and 12 µm respectively. For all compositions, powders were wet mixed in planetary ball mill using alumina balls and ethanol. The powder mixture was hot pressed simultaneously in multi-cavity die under vacuum at 1600°C,1h. Thedensityof the hot-pressed blocks was measured by water displacement method and the sintered density was measured to be in range of 92 to 96% of the theoretical density. No significant weight loss was observed even after hot pressing indicating stability of the diboride phase after the consolidation in vacuum. XRD analysis also confirmed stability of ZrB_2 phase in the hot-pressed composite. Thermal diffusivity was measured by laser flash method and thermal conductivity was evaluated from this.The microstructural features were investigated by SEM-EDS. The thermal conductivity variation as a function of ZrB_2 content have been investigated and correlated to microstructural data.*

Keywords: *Alumina, Zirconium Diboride, Composite, Thermal Conductivity, Laser flash method.*

I. Introduction:

Alumina ceramic powder is one of the most commonly used ceramic in various application for example in grinding media, in cutting tools, in crucibles owing to itsattractive properties like high melting point, high wear and corrosion resistance, high mechanical strength and reasonably high thermal conductivity. Though, it is avery cost effective commercially available ceramics; nevertheless, for most industrial application, the strength, toughness and hardness of alumina are not sufficient. Enormous efforts have been made by researchers to enhance these properties by dispersion of hard particulatessuch as borides and carbides inside alumina matrix [1,2]. Moreover, addition of these hard particulates having high thermal conductivity can influence the thermal conductivity of alumina also along with the mechanical properties [4,5]. In the present paper, the effect of ZrB_2 addition on thermal conductivity of Alumina ceramic has been studied. ZrB_2 is a leading UHTC material due to its unique combination of properties viz. high melting temperature, chemical stability, high electrical and thermal conductivity, high hardness and high corrosion resistance [3,6]. The aim of the study is to overview the effect of different weight percent of ZrB_2 on thermal conductivity of composite and its correlation with microstructural data.

II. Experimental Procedure:

1. Staring powder:

The composite powder sample was prepared from commercially available Al_2O_3 powder (purity 99.9%) and in house prepared ZrB_2 powder (Purity 99.5%). ZrB_2 powder was

prepared by carbothermic reduction of ZrO_2 in presence of B_4C [8,9]. The median particle sizes of Al_2O_3 and ZrB_2 were measured by laser diffraction method and was found to be 4.4 µm and 12 µm respectively.

2. Sample Preparation and Hot-pressing:

3. In order to prepare the composite mixture, the stochiometric amount of the powders were mixed on roller mill in polypropylene bottles for 6 hrs using alumina grinding media. The mixed powders were then hot pressed in multi-cavity graphite die at 1600°C for 1h. The X-ray diffraction pattern of the hot-pressed pellets were taken using XRD(INEL XRG3000, France). The X-ray source was CuKα radiation having λ=1.54Ao and the data was acquired at 30mA current and 40 KV voltage.

4. Sample Characterization:

4.1 Density and microstructure:

The bulk density of the composites was measured using Archimedes fluid displacement method and water was used as the fluid for displacement. Theoretical density of each composite was estimated by rule of mixture approach using densities of pure components $\rho(Al_2O_3)$ =3.99g/cm^3 CC and $\rho(ZrB_2)$ =6.09g/CCcm^3.

$$\rho_{(Composite)} = w(Al_2O_3)\,.\rho(Al_2O_3)\; w(ZrB_2)\,.\rho(ZrB_2) \quad \ldots\ldots(1)$$

Where, w=weight fraction

Microstructure and distribution of second phase ZrB2 in alumina matrix was studied using SEM (Zeiss EVO 18 MA) coupled with EDS (Oxford Xmas80)system .system. All the samples were coated with gold using a sputter coated to make the sample surface conducting.

4.2 Specific Heat:

The temperature dependent specific heat capacity data of the staring powders were taken from NIST JANAF thermochemical tables[13]. The specific heat capacity of the composites was calculated by mass averaging the specific heat capacity data of the starting powders following the kopp-Neuman rule [10].

$$C_p = w(Al_2O_3).C_p(Al_2O_3) + w(ZrB_2).C_p(ZrB_2) \quad \ldots\ldots(2)$$

Where, w= weight fraction

4.3 Thermal Diffusivity:

Thermal diffusivity of the samples ~10mm in diameter and thickness between 1 to 2 mm was measured using laser flash method (Lensies Laser Flash Thermal ConstantAnalyzer LFA1000). Both sides of the samples were coated with thin layer of graphite before the experiment in order to enhance the laser absorption on the front surface and improve the detection from the back surface of sample.Further in this method, the sample of ~10 mm diameter disc was subjected to a specific power pulse from a Nd:YAG laser in vacuum. The energy absorbed by the specimen on the front surface results in temperature rise of the rear surface of the sample. The resulting rise in temperature on the rear surface is recorded by apeltier cooled IR detector.

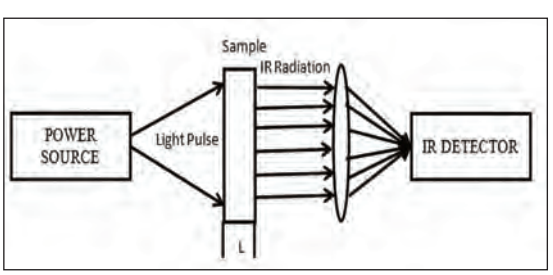

Fig. 1 : Laser Flash method scheme.

The thermal diffusivity values were calculated using following formula:

$$\alpha = \frac{0.13879L^2}{t_{1/2}} \quad \text{.....(3)}$$

Here, α is thermal diffusivity, L is thickness of specimen, and $t_{1/2}$ is the half time required to reach the maximum rise in temperature.

Thermal diffusivity measurement was done from RT to 600°C, at 50°C interval. At each temperature three consecutive measurements were done and average value was calculated.

4.4 Thermal Conductivity:

Thermal conductivity,λ was calculated using the following formula:

$$\lambda = a \cdot \rho \cdot C_{\rho} \quad \text{.....(4)}$$

Where, α is measured thermal diffusivity, ρ is measured density of composite and Cpis calculatedspecific heat capacity data of the composites.

III. Result and Discussion:

1. Phase stability: Figure 2 shows theX-ray diffraction pattern corresponding to all the composites corresponds to alumina and zirconium diboride phase and hence confirms the phase purity of the composites. X-ray peak intensity is decreasing with increasing the ZrB_2 content, this may be an indication of porous microstructure.

2. Density and microstructure:

The composition of all the composites, their measured and relative density is listed in Table 1. Density of composites was found to be decreasing with increasing weight percent of the ZrB_2 phase.

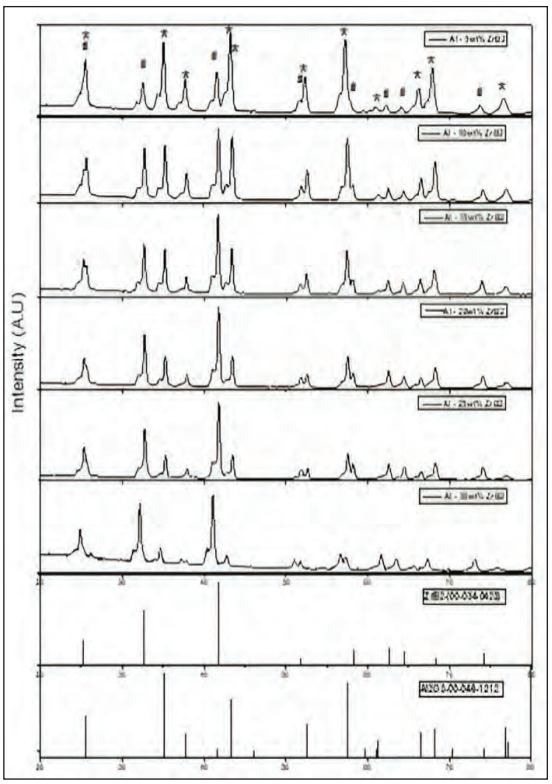

Fig.2: XRD patterns of Al_2O_3-(5-30) wt% ZrB_2 composites hot pressed @1600°C,1h.
*(Here, * is Al_2O_3 phase and # is ZrB_2 phase)*

Table 1: Composition and density of hot pressed Al_2O_3-ZrB_2 composite pellets.

Sample ID	Compositions		Theoretical Density (g/cm³)	Density(g/cm³)	Relative Density (%)
	Al_2O_3	ZrB_2			
Al_2O_3	100	0	3.99	3.88	97%
Al-5ZB	95	05	4.09	3.98	97.2%
Al-10Zb	90	10	4.20	4.06	96.6%
Al-15Zb	85	15	4.30	4.04	94.5%
Al-20Zb	80	20	4.41	4.01	91%
Al-25Zb	75	25	4.51	4.00	88.6%
Al-30Zb	70	30	4.62	4.18	90.5%

Fig 3 is showing the microstructure of the composite and distribution of the ZrB2 phase in alumina matrix. The microstructure data corroborate with the density data and porosity can observed in microstructure. The back scattered electron micrographs (BSE) of the

composite samples showed homogenous distribution of the ZrB_2 phase in alumina matrix. Here the bright phase corresponds to the ZrB_2 phase and dark phase corresponds to the Al_2O_3. The ZrB_2 particlesize has decreased from the staring initial particle size of 14μm to ~2-3μm. As the ZrB_2 weight percent was increased in the composite, the interconnectivity between the ZrB_2 particles was increased resulting in good networking.

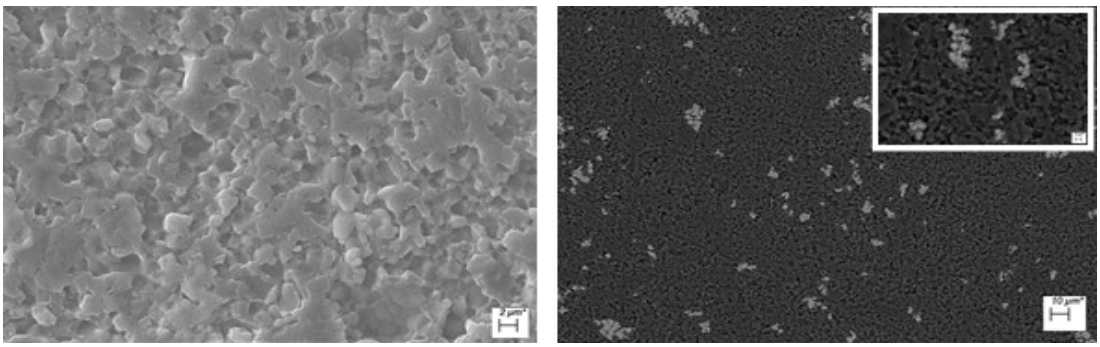

Fig. 3A:(a) SEM and (b) Electron back scattered image of Al_2O_3-5wt%ZrB_2 compact hot-pressed in vacuum at 1600°C, 1 h.

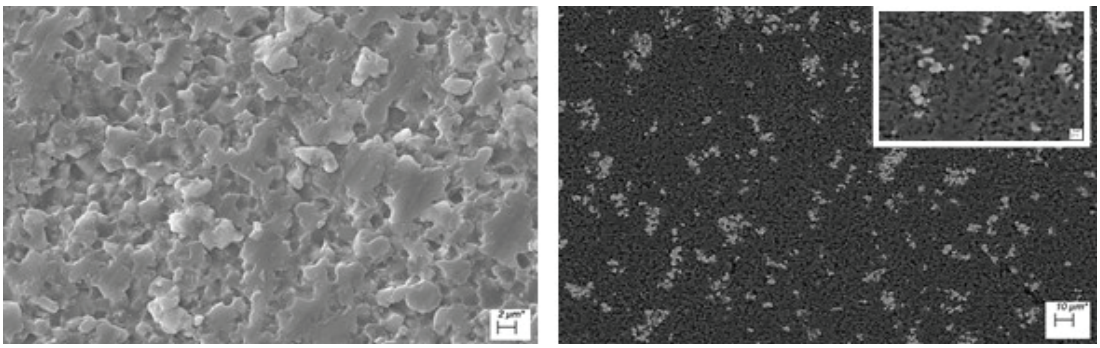

Fig. 3B:(a) SEM and (b) Electron back scattered image of Al_2O_3-10wt% ZrB_2compact hot-pressed vacuum at 1600°C, 1 h.

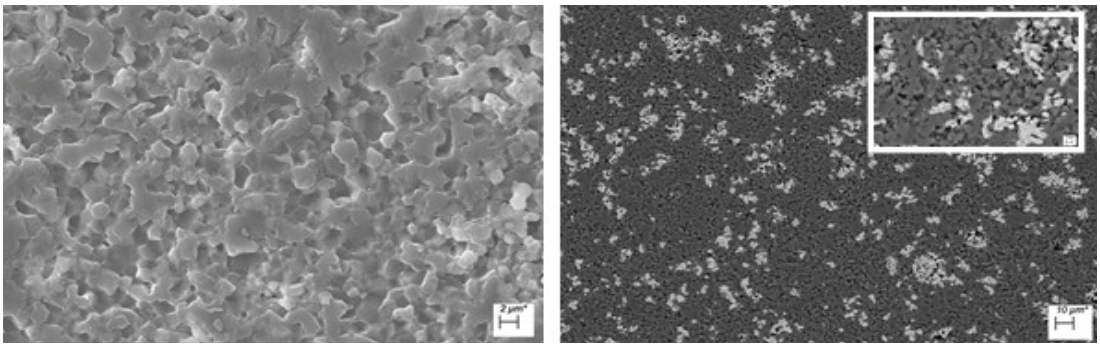

Fig. 3C:(a) SEM and (b) Electron back scattered image of Al_2O_3-15wt%ZrB_2compact hot-pressed vacuum at 1600°C, 1 h.

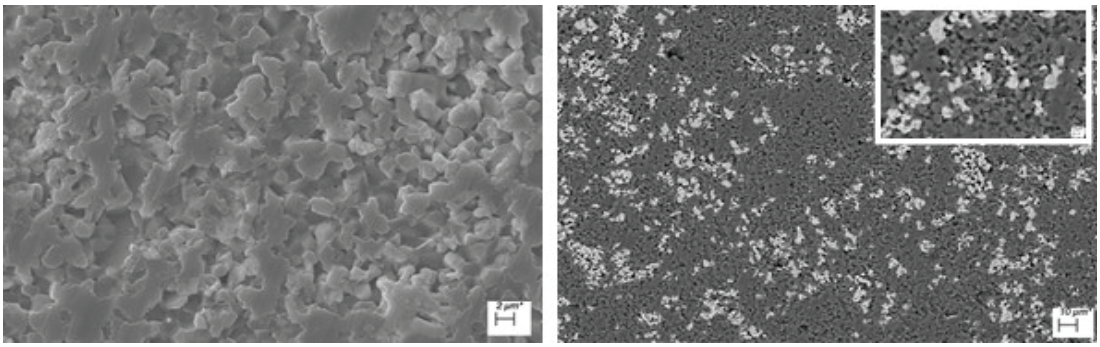

Fig. 3D:(a) SEM and (b) Electron back scattered image of Al_2O_3-20wt%ZrB_2compact hot-pressed vacuum at 1600°C, 1 h.

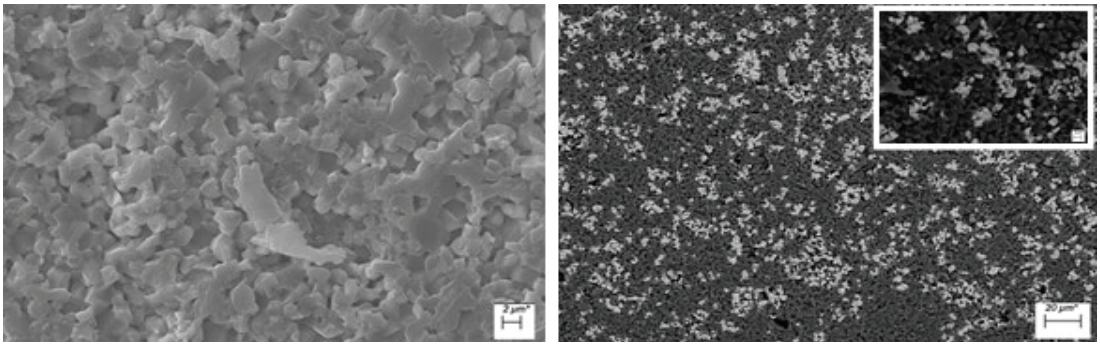

Fig. 3E:(a) SEM and (b) Electron back scattered image of Al_2O_3-25wt%ZrB_2compact hot-pressed vacuum at 1600°C, 1 h.

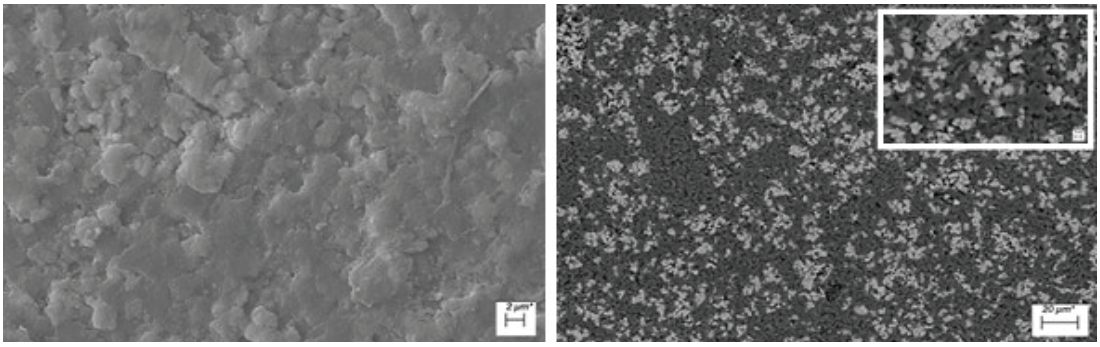

Fig. 3F:(a) SEM and (b) Electron back scattered image of Al_2O_3-30wt%ZrB_2compact hot-pressed vacuum at 1600°C, 1 h.

3. Thermal Conductivity:

Figure 4 shows the thermal conductivity variation in Al_2O_3-ZrB_2 composites with varying the ZrB_2 weight percent. ZrB_2 is high thermal conducting ceramic known for UHTC applications and its addition should enhance the thermal conductivity of the alumina matrix composite and clearly it can be seen that all

composites have thermal conductivity values more than that of pure alumina.

But the thermal conductivity data of the composites does not follow the expected trend with increasing the concentration of ZrB_2. This can be explained based on the role of three factors, which are, role of high thermal conductive phase addition, role of porosity and role of percolation effect.

Role of high thermal conductive phase addition in all the composites and role of percolation effect with high quality networking of ZrB_2 phase in composites with 25-30 wt% ZrB_2 can be clearly seen in increasing the thermal conductivity of the composites. But since all the composites are not equally dense, role of porosity can be commented only after porosity correction in next section.

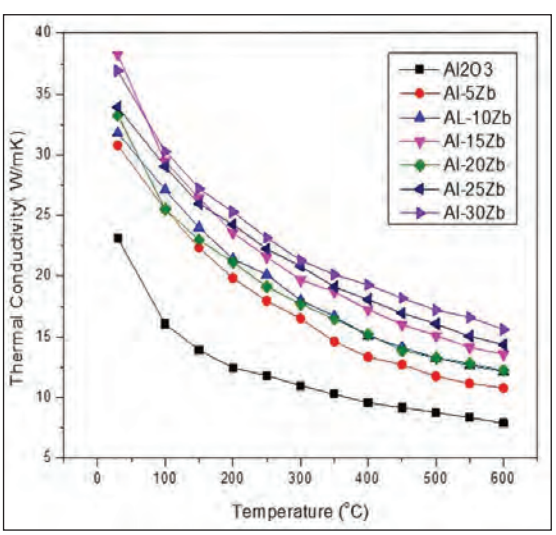

Fig 4A: Thermal Conductivity variation in Al_2O_3-ZrB_2 composites with varying the ZrB_2 weight percent.

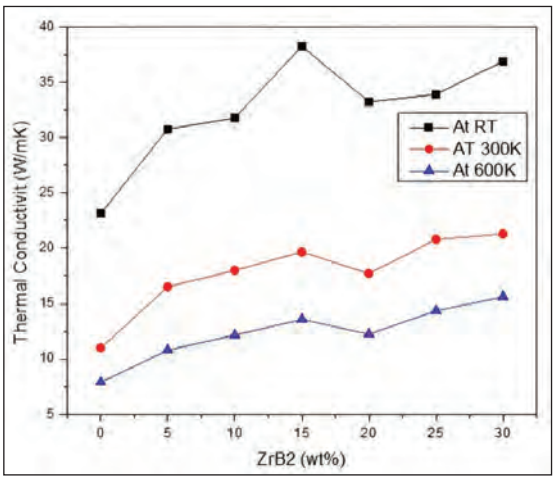

Fig 4B: Thermal Conductivity variation in Al_2O_3-ZrB_2 composites at RT, 300°C and 600°C

4. Porosity Correction:

Since all the composites presented here in the study are not fully dense and porosity ranges from 3% to 11%, therefore, the thermal conductivity data does not reflect the trend in the increase in thermal conductivity values with the increase in high thermal conducting ZrB2 phase. Therefore, all thermal conductivity data presented here were corrected with respected to porosity via the following exponential relation [11]:

$$\frac{k}{k_o} = \exp\left(\frac{-1.5\varphi}{1-\varphi}\right) \quad \text{.....(5)}$$

Here, k is thermal conductivity of the porous material, kois thermal conductivityof dense material and φ is percent porosity in the sample. This exponential factor has been derived by a functional equation approach and shows full analogy in elastic properties [12].

Figure 5A is showing the thermal conductivity data of the composites after the porosity

correction using the above exponential correction factor. The trend in thermal conductivity data is same as the data without correction and but the values have increased. After correction, the overlapping data for the composite with 10wt% and 20wt% ZrB_2 has got separated and is following the expected increasing trend in thermal conductivity with increase in weight % of high thermal conductive phase in matrix.

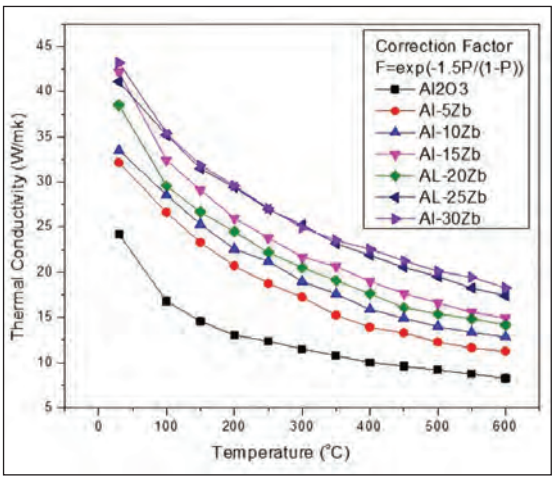

Fig 5A: Thermal Conductivity variation in Al_2O_3-(0-30wt%)ZrB_2 composites considering porosity correction.

Figure 5B is showing the porosity corrected thermal conductivitydata of the Al_2O_3-(0-30wt %) ZrB_2 composites at RT, 300°C and 600°C. This figure is showing that the data corresponding to composite with 15wt% ZrB_2 is still following the same trend as before. This can be due to the reason that upto this composition the porosity values are in the range from 97% to 94.5%, that is within 2.5% and role of porosity is dominated by the role of high thermal conductive phase addition. But in later composition with 20wt% ZrB_2, role of porosity is observed, but it is again surmounted by the percolation effect of second phase in the matrix and hence enhancing the thermal conductivity of the samplesfurther with even higher porosity values.

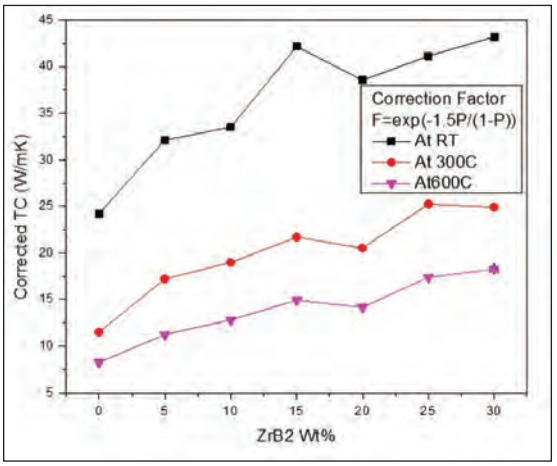

Fig 5B: Porosity corrected TC variation in Al_2O_3-(0-30wt %) ZrB_2 composites at RT, 300$_o$C and 600$_o$C.

IV. Conclusion:

Al_2O_3-ZrB_2 composites with varying ZrB_2 wt% have been synthesized by vacuum hot pressing @1600°C, 1h. Uniform distribution of ZrB_2 phase in alumina matrix have been obtained in all composites. In BSE image, high networking of ZrB_2 particles was observed. Thermal conductivity of all composite compositions was found higher than the thermal conductivity of alumina. The thermal conductivity values of the composite have first increased with increase in high thermal conductive ZrB_2 wt% phase addition then decreased following the role of porosity and finally increased due to high networking of ZrB_2 particles resulting in thermal percolation behavior.Porosity correction using the exponential correction factor has shown increase in thermal conductivity values following the same trend as before correction.

References:

1. B Li, J.X.Deng, Y.S.Li, , International Journal of Refractory Metals and Hard Materials 27 (2009) 747-753.
2. C.L.Yeh, R.F.Li, ,Chemical engineering journal, 147 (2009) 405-411.
3. C.L.Yan, R.J.Liu, C.R.Zang, , RSC Adv, 5 (2015) 78606-78616.
4. J. Liu, P.DOwnby, J. Am.Ceram.Soc.74 (1991) 241.
5. V.Sundaram,K.V.Logan, R.F.Speyer, J. Mater. Res. 12 (1997) 1681.
6. Fahrenholtz W G, Hilmas GE, Talmy IG. J. Am. Ceram Soc. 90 (2007) 1347-64.
7. Jan Hostasa, Willi Pabst, Jiri Matejicek, J. Am. Ceram. Soc. 94[12] (2011) 4404-4409.
8. Wei-Ming Guo and Guo-Jun Zhang, J. Am. Ceram. Soc., 92 [1] (2009)264–267.
9. Hui-Yu Qiu, Wei-Ming Guo, Ji Zou, Guo-Jun Zhang, Powder Technology 217 (2012) 462–466.
10. J. Leitner, P. Vonka, D. Sedmidubsky, P. Svoboda, Thermochimica Acta, 497 (2010) 7–13.
11. G.Ticha, W. Pabst and D.S Smith, J. Mat. Sci. 40[18] (2005) 5045-5047.
12. W. Pabst,and E. Gregorova, J. Mat. Sci. 39[9] (2004) 3213-5045.
13. https://webbook.nist.gov/

IMPROVING THE WEAR PERFORMANCE OF PA-6 BY REINFORCING GRAPHITE AND SUBSEQUENT CRYOGENIC TREATMENT

Swamini Chopra[1*], Tushar S. Walwekar[2], Ganesh M. Surushe[2], Kavita Pande[3*], G. M. Kotiye[4], V. S. Damdhar[4], S. R. Kulkarni[2]

[1]Centre of Excellence in Materials and Metallurgy, Mechanical Engineering Department, Maharashtra Institute of Technology, Aurangabad

[2]Mechanical Engineering Department, Maharashtra Institute of Technology, Aurangabad

[3]Director, Matverse Vision Pvt. Ltd., Nagpur

[4]Center for Engineering Exploration, Maharashtra Institute of Technology, Aurangabad

Abstract: *The aim of present work is to improve the wear performance of virgin PA6 polymer by two different approaches; one is by reinforcing graphite into the matrix and other is by cryogenically treating the material. The graphite contentreinforced in the PA6 matrix is initially optimized for maximum improvement in wear performance. From 1, 2, 5, 10 and 15 wt.%, it is observed that PA6 composite reinforced with 5 wt.% graphite gives maximum wear enhancement of ~18%. The increasing graphite content tends to deteriorate the wear performance owing to agglomeration and subsequent rapid removal of material. Moreover, virgin PA6 and PA6 composite reinforced with 5 wt.% graphite is cryogenically treated at -185°C for 12 hours and their wear performance comparedin both untreated and cryo-treated conditions. When virgin PA6 is cryo-treated, the specific wear rate improved by ~14%, while the PA6/graphite compositereflects ~31% improvement. This can be attributed to the densification of polymeric chains after cryogenic treatment which helps to arrest the tearing of material from the surface during abrasive wear conditions. FTIR analysis confirms this claim byreflecting the restriction of PA6 chain ends and branching groups after cryogenic treatment as well as after addition of graphite, thereby making the matrix dense. It is summarized from FTIR that the changes experienced by PA6 matrix after the treatment are dominant and thus, both cryo-treated virgin PA6 and its composite exhibit similar cryo-structural modifications. The SEM analysis of the worn-out surface also supports the specific wear rate results and provides a visual indication of reduction in the severity of wear before and after the treatment.Thus, it is concluded here that graphite reinforced PA6 gives better wear performance as compared to virgin PA6 and thus, it can be advocated as its replacement in wear prone applications. An added benefit, not only in the terms of enhanced wear performance but also with an aim of getting a durable material with good structural integrity, can be achieved by cryogenically treating the PA6/graphite composite, which shows ~44% better wear than untreated virgin PA6 polymer. The present manuscript concludes by superimposing the cryo-treated PA6/graphite composite on the Ashby diagram for better understanding.*

Keywords: *Cryogenic treatment; Polyamide 6; Graphite; Wear performance; Ashby diagram.*

Graphical Abstract:

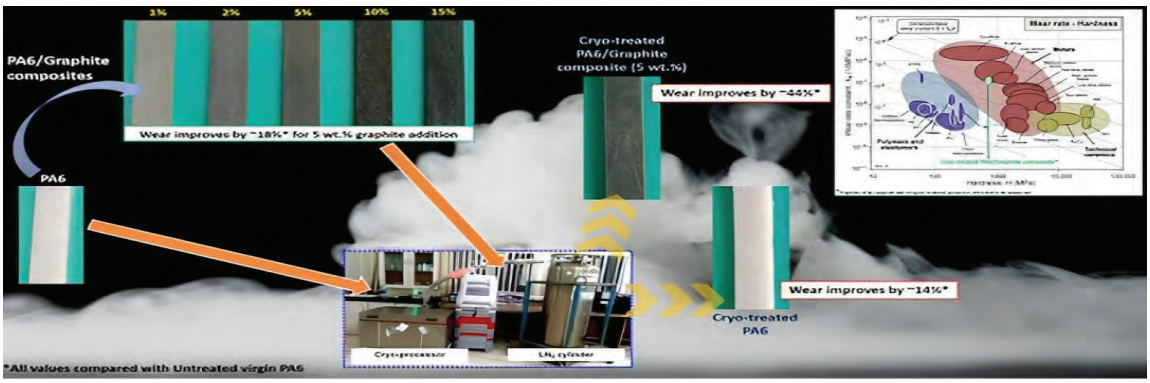

1. Introduction

Polyamide 6 (PA6, also known as Nylon 6) is a popular engineering polymer having high strength, good durability and mechanical damping capacity. PA6 also exhibits good wear performance and is widely used in wear prone applications like gears, bearings, screws, shaft sleeves, machine guards, seals, chain guards, rotor slot wedges, track plates, etc. [1]. However, under extensive mechanistic situations, PA6 loses its structural integrity and this can lead to rapid wear of the component. It is well-known that reinforcing a high strength filler into the polymer matrix imparts good mechanical properties to the composite. The use of graphite as filler is very common. Even for PA-6, graphite has proven to be a beneficial filler. Srinivas et al. [2] reported the fabrication of graphite reinforced PA6 composite by melt-compounding technique. From graphite weight contents of 10, 15, 20, 25 and 30 %, they report maximum improvement in the wear resistance and coefficient friction for 25 wt.% graphite. This reduction in specific wear rate and coefficient of friction is by ~80% and ~20%, respectively. Satheeskumar and Kanagaraj[3] explored the mechanical properties of graphite reinforced PA6 with additions from 5 to 40 wt.%. With 20 wt.% graphite, the impact strength of the composites increased by ~35%, wear rate by ~76% and tensile strength by ~16%. This was attributed to uniform distribution of the filler and strong bonding between filler and matrix. Additionally, it was observed for this composite that the elongation decreased marginally owing to the hardening of the matrix due to the presence of graphite particles. The strong filler tends to reinforce into the matrix well, but due to good interfacial interaction between the filler and matrix, the crystallinity of the composite increases and leads to an increase in hardness [3]. This collectively improves mechanical strength and wear resistance, however, at the expense of the elasticity of the material.

In another study, Satheeskumar and Kanagaraj[4] again explored the wear performance of graphite reinforced PA6 composite. They report maximum improvement in the wear arte for 20 wt.% graphite addition. Furthermore, they also highlight the effect of filler loading on the surface roughness of the worn-out sample. They observed that after the addition of graphite the roughness of the composite worn-out surface is less than virgin PA6 surface by ~15%. This was credited to the formation of a wear layer that lowers the abrasive action of the counter face during wear testing. The graphite is a well-known dry lubricant and, hence, as the wear layer is formed on the counter face, the good lubricity effect will ultimately reduce the severity of the abrasive conditions and lead to reduced surface roughness[4]. Thus, owing to its lubricating properties, graphite reinforced polymer composites are good candidates for tribological applications.

Furthermore, in order to improve the wear performance, cryogenic treatment has also proven to be an effective technique for various polymers and composites. It has gradually been established as a process to enhance the mechanical properties, specifically wear resistance, of polymeric materials by incorporating positive bulk structural changes. Pande et al. [5] explored the cryogenic treatment of Polytetrafluoroethylene (PTFE) at -80, -140 and -185°C for various soaking periods of 4, 8, 12, 16, 20 and 24 h. The change in % crystallinity and crystallite size was found to be the most influential parameter resulting in improved wear performance of PTFE. In another study,

Pande et al. [6]reported the cryogenic treatment of PA6 to improve its mechanical properties. Similar to PTFE, increase in % crystallinity was found to be the most important parameter. Modifications in the structure, conversion of less stable phases into more stable phases and formation of complex phases was reported to be other influencing parameters for enhancement in the wear properties. In both the studies, cryogenic treatment at -185°C for 12 h of soaking period was found to be optimum. A recent work by our team on the cryogenic treatment of Ultra-high Molecular Weight Poly-ethylene (UHMWPE)[7] reports that the cryogenic treatment temperature and time is significantly dependant on the polymer chemistry and structure. For UHMWPE, instead of -185°C, the optimum process temperature was found to be -140°C for 12 h of soaking period.

There are many reports that prove cryogenic treatment to be equally effective in improving the mechanical properties of polymer composites. Damdhar et al. [8] explored the possibility of cryogenically treating the PTFE-Mica composite coatings used in cookware. They report ~40% improvement in the wear resistance of the composite coating after treatment at -185°C for 12 h. When field tested, the same cryo-treated cookware performed better in the non-stick test and adhesion test for utensils. In a different study by our team, the fibre and particulate reinforced Polybutylene terephthalate (PBT) composites were cryogenically treated at different temperatures and soaking period [9]. The wear performance of both glass-fibre reinforced and wollastonite reinforced PBT composites increased by ~84% and ~96%, respectively for cryogenic treatment at -185°C for 8 h. Another work by our team reported similar findings for polymer nano-composites[10], wherein the enhancement in the structure and properties is largely governed by the polymer matrix and the interfacial interaction between the filler and the matrix. This behaviour was observed in both PBT and PA6 reinforced with Multi-walled Carbon nanotubes (MWCNTs).

Thus, with numerous successful studies by our team on the cryogenic treatment of different polymeric materials, the aim of present work is to improve the wear performance of PA6 by two different approaches; one is by reinforcing graphite and other is by cryogenically treating the material. With reference to previous reports on enhancements in the mechanical properties of cryo-treated PA6 and composites [6,10]; the same treatment parameters of -185°C and 12 h are explored herein for graphite reinforced composites.

2. Experimental Details

2.1 Materials and Sample Fabrication

The PA6 polymer was procured in the form of granules (Grade: Gujlon M28RC, Density: 1.13 g/cm3) from GSFC, Gujarat. The graphite was received from Matverse Vision Pvt. Ltd., Nagpur in powder form (Degree of graphitization: min. 96% C, Moisture content: 0.5-1%, Mean particle size d50 ~ 4-10 µm, Density: 2.2 g/cm^3). The graphite powder was mixed with PA6 granules in fixed amounts of 1, 2, 5, 10 and 15 wt% by melt-compounding technique.

Prior to compounding, the graphite powder was mixed with PA6 in required quantities and the mixture dried at 80°C in an air oven for 4 h to minimize the effects of moisture. Only PA6 granules was also subjected to the same procedure to ensure similar thermal history. The melt compounding was done with a 25 mm single screw extruder (Make: M/s Boolani Engineering Corporation) with four heating zones set at 210,

230, 240 and 250°C. The extruded strands from the extruder were then allowed to cool in a water bath and palletized by the wire cutting unit (Make: M/s Boolani Engineering Corporation). Thepellets were then injection moulded as per ASTM specifications in a hydraulic injection moulding machine (Make: Electronica, Model: Optima 75–128) at a constant injection pressure of 90 bar and injection temperature of 250-260°C. The samples fabricated by this process are listed in Table 1 along with their used nomenclature.

Table 1 Sample details and Sample codes used

Sr. No.	Sample composition	Cryogenic treatment parameters	Sample Code
1	Virgin PA6	Untreated	P
2	PA6 + 1 wt.% graphite		G1
3	PA6 + 2 wt.% graphite		G2
4	PA6 + 5 wt.% graphite		G5
5	PA6 + 10 wt.% graphite		G10
6	PA6 + 15 wt.% graphite		G15
7	Virgin PA6	Treated at -185°C for 12 h	PC
8	PA6 + 5 wt.% graphite		G5C

2.2 Cryogenic Treatment

Based on the pilot experimentation, the graphite content was finalized to 5 wt.%. Both virgin PA6 and 5 wt.% graphite reinforced composite were then cryogenically treated using liquid nitrogen at -185°Cfor a soaking period of 12 h in the cryostat (Self-fabricated, Cooling rate: 2°C/min, Max. temperature capacity: -196°C). The treated samples were then allowed to attain room temperature gradually in an insulated box. The structural and mechanical properties of all the untreated and cryo-treated samples were then compared for further study.

2.3 Mechanical and Structural Characterization

The wear performance of the samples was evaluated on a pin-on-disc wear tester (Make: Magnum Engineers, Bangalore) using load: 40N, track diameter: 80 mm, speed: 300 RPM and time: 10 min. The pins with dimension 10 mm × 10 mm × 30 mm were used for experimentation purpose and abraded against SiC paper(grade 320) as counter-face. Three test results were averaged for each type of sample and then reported. The hardness of the samples was measured in Shore D hardness scale using a Shore hardness tester (Make: STECH Engineers) according to ASTM standard D-2240 at test load of 4.5 kgs. Ten hardness values were averaged and then reported. The changes in the structure of PA6and its composite, before and after cryogenic treatment, was determined using FTIR spectrometer (Make: Shimadzu, Model: FTIR 1-S Affinity) for wavenumber range 400-4000 cm-1. The samples were scanned with an attenuated total reflection (ATR) unit using single crystal Diamond probe with 45 runs.The morphology of the graphite powder and the worn-out surfaces of the samples were investigated by FE-SEM (Make:JEOL, Model: JSM-7610F). Prior to electronmicroscopy; the sample surfaces were sputter-coated with a thin platinum layerusing auto-fine coater (Make: JEOL, Model: JEC-3000FC) to make thesurfaces conducting for obtaining images.

3. Results & Discussion

3.1 Pilot Experimentation

The pilot experimentation was carried out to optimize the graphite content reinforced in PA6 matrix for achieving enhanced wear performance. Fig. 1(a)shows the graphs of specific wear rate (SWR) and Shore D hardness of all the PA6/graphite composites, while Fig. 1(b) and (c) shows the graphite flakes used to prepare the composite in powder form.It is clear from the SWR values that the reinforcement of graphite into the PA6 matrix has a positive effect. The wear of the composites reduces with the incorporation of graphite, however, till 5 wt.% only. This reduction is ~18% for G5

composite. Further, as the graphite content increases to 10 and 15 wt.%, the SWR increases marginally and is similar to that of virgin PA6. Similar behaviour is reported in many studies as well [11,12]. This behaviour of the composites has been credited to the interaction between graphite and PA6 matrix. For lower loadings, the graphite is dispersed uniformly throughout the PA6 matrix. However, as the graphite content increases, the agglomeration of graphite particles into the matrix increases. During abrasive wear of the samples, as the large sized chunk of the agglomerates is pulled out of the sample surface, it tears out more material from the surface [13]. This reflects as increased wear in the samples. The Shore D hardness of the composites was also evaluated and found to be in the range of 84±1.2 for samples P, G1, G2 and G5. However, it was noteworthy to see that the hardness increase lightly to 86±0.7 Shore D for G10 and G15 composites. This indicates towards the fact that incorporation of graphite in small quantities does not affect the hardness of the composites significantly, however, as the graphite content increases to 10 wt.% and then to 15 wt.%, there is a marginal increment in hardness. This can be credited to the presence of hard graphite particles and the agglomerates present in the composite. Thus, it is concluded from pilot experimentation that 5 wt.% graphite is advantageous in increasing the wear performance of PA6 polymer and G5 composite is considered for further studies on cryogenic treatment.

3.2 Cryogenic Treatment of PA6 and Graphite Composites

The samples P and G5 were cryogenically treated at -185°C for 12 h and their SWR and Shore D hardness are illustrated in Fig. 2(a) and (b), respectively.It is clear from Fig. 2(a) that

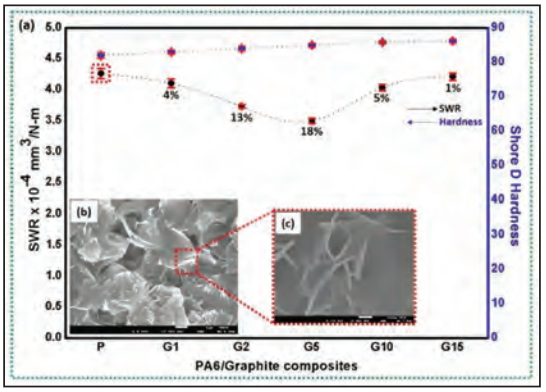

Fig. 1 (a) Specific wear rate of PA6/graphite composites, (b) SEM image of graphite flakes used, (c) Magnified image of graphite flakes

the wear performance of the material improves on cryogenic treatment, as reported by many [7–10,14–17].In case of virgin PA6, the SWR reduces from 4.26x10-4 mm^3/N-m to 3.65x10-4 mm^3/N-m. While, for G5 it goes from 3.49x10-4 mm^3/N-m to 2.4x10-4 mm^3/N-m after cryogenic treatment at -185°C for 12 h of soaking period. The objective of present work was to explore ways to enhance the wear performance of PA6 polymer. Thus, it can be seen here that when the virgin PA6 is reinforced with 5 wt.% of graphite, the wear performance enhances by ~18% (P to G5), whereas, when it is cryogenically treated, the wear of virgin PA6 improves by ~14% (P to PC). On the other hand, while incorporation of graphite imparts good wear performance to PA6, the cryogenic treatment of the PA6/graphite composite itself reflects an increment of ~31%(G5 to G5C), which is approx. ~44% more than untreated virgin PA6 (P to G5C). Thus, the sample G5C can be advocated to replace virgin PA6 where superior wear performance is desired, as the synergistic advantage of reinforcing graphite in the PA6 matrix and then cryogenically treating the composite is evident from Fig. 2(a).

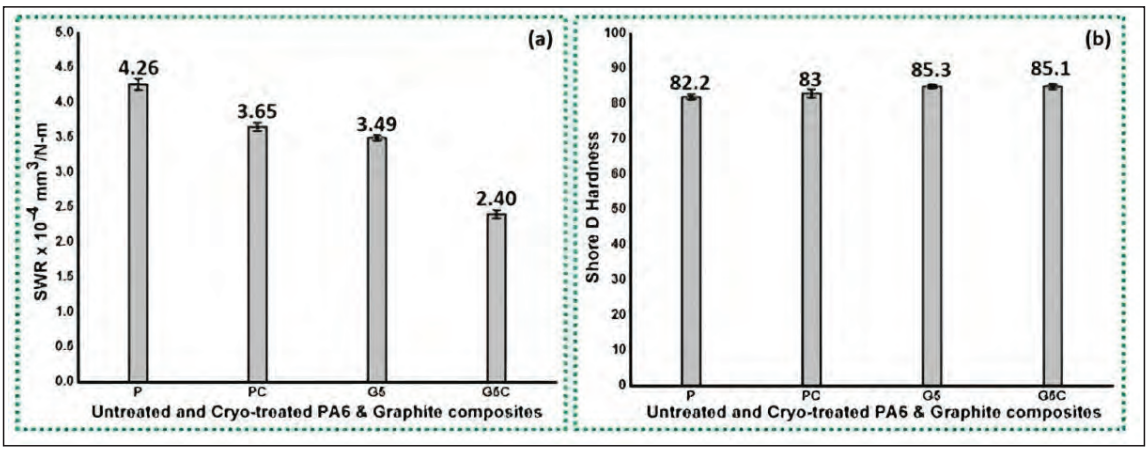

Fig. 2 (a) Specific wear rate, (b) Shore D hardness of PA6 and its Graphite composite before and after Cryogenic Treatment

The Shore D hardness of the samples are illustrated in Fig. 2(b). The values represented in the graph are average of multiple readings. Hence, even though the hardness seems to be increasing for virgin PA6 after cryogenic treatment, the standard deviation for both P and PC overlap. There are previous studies which report ~10-15% increase in the hardness of virgin PA6 after cryogenic treatment at -185°C for 12 h [6,10]. However, it can be seen here that the hardness of PA6 remains unaffected by the treatment. Similarly, the hardness of the sample G5 remains more or less same after cryogenic treatment too. These results indicate that the semi-crystalline nature of the PA6 matrix does not change significantly after the treatment and hence the hardness values remain nearly similar.It is imperative to note here that even though the hardness of the PA6 and its graphite reinforced composite does not change after cryogenic treatment, the wear performance shows noteworthy improvement. The SEM of the worn-out surfaces, shown through Fig. 3(a) to (d), reflect a similar trend to that of SWR values shown in Fig. 2(a). The worn-out surface of untreated PA6 looks more damaged than the rest of the samples. The abrasion grooves on the surface are more deep and pronounced. After cryogenic treatment, the SWR of PA6 improves, albeit it still exhibits deep groves, as seen in Fig. 3(b). The improvement in the wear performance of sample G5 reflects as a relatively smooth worn-out face as evident from Fig, 3(c).

This improvement can be credited to the nano-reinforcing effect of graphite as well its lubricating nature. Once the wear of the surface initiates, the formation of transfer layer and the presence of graphite particles between the contact surfaces creates a lubricating barrier which helps in reducing the SWR [18–21]. Cryogenic treatment is known to densify the polymeric structure, cause favourable chain realignment and strengthen the interface between polymer matrix and filler [9,10,17]. From the worn-out surface of the G5C sample, it can be seen that surface appears to be the least damaged amongst the samples. The presence of lubricating graphite particles and the positive structural changes in PA6 matrix brought about by the treatment can be credited for the enhanced wear performance, as seen from worn-out surface in Fig. 3(d) as well. In

order to investigate this, FTIR was done for PA6 and its graphite composite, both untreated and cryo-treated, and the changes in their chemistry are compared. Fig. 4 shows the FTIR graphs of all the 4 samples in a comparative manner.

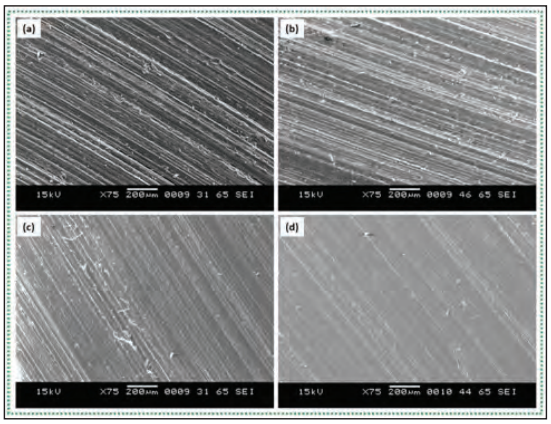

Fig. 3 SEM micrographs of worn-out surfaces of samples (a) P (b) PC (c) G5 (d) G5C

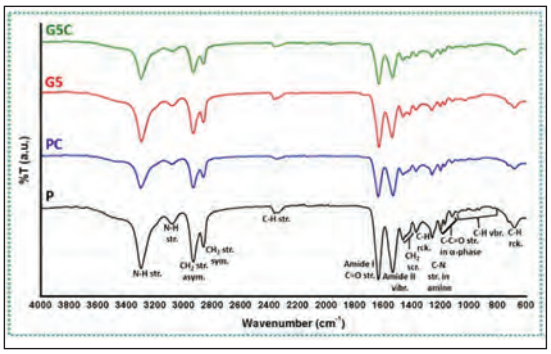

Fig. 4 FTIR spectra of untreated and cryo-treated PA6 and its graphite composite

With reference to the previous literature [10,22–24], following characteristics peaks can be assigned for virgin PA6 polymer under present study (sample P): N-H stretch at 3298 and 3082 cm-1, asymmetric CH2 stretch at 2931 cm^{-1}, symmetric CH_2 stretch at 2860 cm^{-1}, C-H stretch at 2335 cm^{-1}, amide I C=O stretch at 1635 cm^{-1}, amide II vibrations (combination of N-H bend and C-N stretch) at 1533 cm^{-1}, cluster of CH_2 scissoring vibrations between 1460-1420 cm^{-1}, C-H rocking at 1369 cm^{-1}, C-N stretch in amine at 1259 cm^{-1}, multiple vibrations for C-C=O stretch in α-phase between 1200-1110 cm^{-1}, cluster of multiple CH vibrations (stretch, rocking, bending, etc.) between 1080-800 cm^{-1}, and C-H rocking at 723 and 680 cm^{-1}. It was observed from the FTIR that cryo-treated PA6 reflects more or less same peaks, however with minor changes. A new peak appears in sample PC at 1442 cm^{-1}, indicating CH_2 scissoring. Additionally, an upshift was observed in the positions of two peaks, viz. N-H stretch and C-H stretch. These peaks shift from 3298 cm^{-1} to 3330 cm^{-1} and 2335 cm-1 to 2345 cm^{-1}, respectively, in case of sample PC. This shift can be credited to the intrasheet bonding taking place in PA6,as reported in other studies [10,25–27]. During cryogenic treatment, as the PA6 material contracts physically, the polymer molecules move closer to each other. The shift in the energy of molecules and bonds lead to weak hydrogen bonding taking place in between the adjacent sheets of the polymer [9,10]. As the parallel sheets of molecules move closer to each other, the structure becomes dense, leading to the formation of longer chains arranged in a compact pattern. This molecular rearrangement imposes motion restriction on the branching chains, thereby reflecting as CH_2 scissoring and a shift in the N-H and C-H stretching. A similar phenomenon is explained in detail in our previous studies [5,7–10,17], and thus, it can be concluded here that PA6 under present study also undergoes the same.

In case of sample G5, even with the addition of 5wt.% graphite, it can be seen from the FTIR graph that the composite reflects maximum of the characteristics peaks of PA6. However, there

are few significant changes, such as downshift in the position of amide I C=O stretch from 1635 cm^{-1} in P to 1629 cm^{-1} in G5. Additionally, a new peak appearsat 1737 cm^{-1} reflecting C=O stretch vibrations, which looks like a shoulder to the amide I C=O stretch peak at 1629 cm^{-1}. The appearance of such a C=O shoulder to a C=O peak and the shifting of amide I C=O peak indicates a disturbance in the structure of PA6 chains, which can be brought about by the physical presence of graphite particles and its bonding with the polymeric matrix. The bonding between graphite and PA6 can be confirmed by the upshifting of C-H stretch peak from 2335 cm^{-1} to 2362 cm^{-1} and the disappearance of minor C-H vibrations from G5 sample, which were previously at 1076, 831 and 723 cm^{-1} in case of sample P.It is well known that the N-H end group and the C=O branch in the chain of PA6 are the potential sites for filler interaction [12,28–30]. The interaction of graphite with these chain end groups and branching groups will impose a physical motion restriction to the PA6 chains, thereby disappearing the C-H vibrations in case of G5. Thus, the disappearance of these peaks indicates good extent of adhesion and/or reactive coupling between PA6 and graphite. Upon cryogenic treatment, G5C composite reflects a similar FTIR graph to that of G5 composite, albeit many peaks reflecting CH vibrations in between 1120 to 700 cm-1 disappear. Additionally, 2 new peaks appear at 1965 cm^{-1} and 1440 cm^{-1} reflecting C=O stretch and amide III C-N symmetry vibration, respectively. The response of G5C to cryogenic treatment is similar to that of sample PC, wherein the contraction of material at low temperatures will result in a dense structure having longer chains arranged in a compact pattern. In addition to these changes, the graphite particles which tend to bond with the PA6 chain end groups and branching groups, also experience contraction at low temperatures. The combined effect of molecular rearrangement of PA6 chains and the physical contraction of graphite particles causes vibrations in the bonds formed between them. As the bonding of graphite occurs at N-H group and C=O group, the appearance of these 2 new peaks is justified, resulting from the motion restriction imposed by the molecular rearrangement.Thus, it can be seen from the FTIR analysis that the structural modifications brought about by the cryogenic treatment of PA6 and PA6/graphite composites makes the material dense, stable and stronger as compared to untreated material. This ultimately reflects in the mechanical performance of the materials, thereby, supporting the enhanced wear resistance of the cryogenically treated PA6 and PA6/graphite composite.

4. Conclusion

The aim of present work was to improve the wear performance virgin PA6 polymer by two approaches; viz. reinforcing with graphite and cryogenic treatment of the material. It can be concluded from the above results and discussion that both the routes prove beneficial to achieve enhanced wear performance. The incorporation of 5 wt.% graphite into PA6 matrix give ~18% improvement, while cryo-treated virgin PA6 exhibits ~14% enhancement when treated at -185°C for 12 h. On the other hand, the cryogenic treatment of PA6/graphite composite itself at same parameters results in a substantial ~44% improvement in wear performance as compared to untreated virgin PA6 polymer. Thus, the present work advocates the use of cryogenically-treated PA6/5 wt.% graphite composite instead of untreated virgin PA6 polymer for heavy tribological applications. Thus, the superior performance of cryo-treated PA6/graphite composite is represented by superimposing its

wear rate constant and hardness on the material selection Ashby diagram [31,32] for comparison with existing polymeric materials.

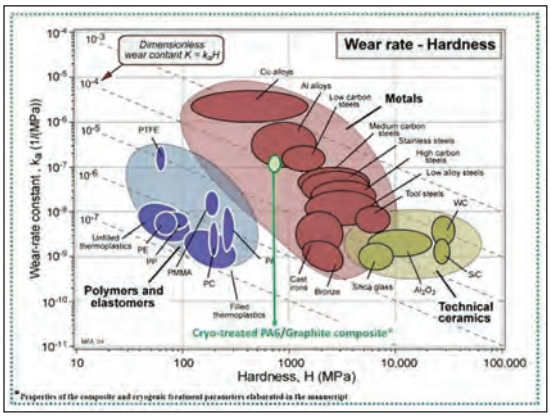

Fig. 5 Position of PA6/graphite composite explore in present work on the materials selection chart based on the Wear rate constant and Hardness [31,32]

Acknowledgement

The authors are thankful to the Centre for Advanced Materials Research and Technology [ISO Certified (9001:2015)], Plastic & Polymer Engineering Department, Maharashtra Institute of Technology, Aurangabad (M.S.), India for providing the FTIR testing facility. In addition, the authors are grateful to the Department of Metallurgical and Materials Engineering, Visvesvaraya National Institute of Technology (VNIT), Nagpur (M.S.), India for assisting with the FE-SEM testing of the samples.

Declaration: The authors declare that there is no conflict of interest for the publication of present work. No funding was received for present work.

References:

1. Kausar A. Trends in graphene reinforced polyamide nanocomposite for functional application: a review. Polym.-Plast. Technol. Mater. 2019;58:917–33.
2. Srinivas CL, Sarcar MMM, Suman KNS. ABRASIVE WEAR PROPERTIES OF GRAPHITE FILLED PA6 POLYMER COMPOSITES. 2012;
3. Sathees Kumar S, Kanagaraj G. Investigation on Mechanical and Tribological Behaviors of PA6 and Graphite-Reinforced PA6 Polymer Composites. Arab. J. Sci. Eng. 2016;41:4347–57.
4. SATHEESKUMAR S, KANAGARAJ G. Experimental investigation on tribological behaviours of PA6, PA6-reinforced Al2O3 and PA6-reinforced graphite polymer composites. Bull. Mater. Sci. 2016;39:1467–81.
5. K. N. Pandey, D. R. Peshwe and A. Kumar, Influence of cryogenic treatment on wear behaviour of Polytetrafluoroethylene) – Teflon, Indian Journal of Cryogenics 38: 62, 2013
6. Pande KN, Peshwe DR, Kumar A. Effect of the Cryogenic Treatment on Polyamide and Optimization of Its Parameters for the Enhancement of Wear Performance. Trans. Indian Inst. Met. 2012;65:313–9.
7. Chopra S, Deshmukh KA, Somvanshi MV, Patil NV, Rakhe SR, Sontakke RV, et al. Structural Elucidation and Mechanical Behavior of Cryogenically Treated Ultra-High Molecular Weight Poly-ethylene (UHMWPE). Trans. Indian Inst. Met. 2021;74:255–65.
8. Damdhar VS, Pande KN, Peshwe DR, Gogte CL. To Investigate the Wear Mechanism on Cryogenic Treatment of PTFE-Mica Filled Composite Coatings in Cookware. Trans. Indian Inst. Met. 2015;68:611–21.
9. Deshmukh KA, Chopra S, Khajanji P, Deshmukh A, Peshwe DR. Effectiveness of cryogenic treatment on PBT composites: prediction of interfacial interaction parameter and its influence on filler bonding and wear performance. Polym. Bull. 2022;79:381–405.
10. Chopra S, Sreya S, Babhulkar RV, Halde SP, Deshmukh KA, Peshwe DR. Cryogenic Treatment of Polymer/MWCNT Nano-Composites for Mechanical and Tribological Applications [Internet]. Nanotechnol. Aerosp. Struct. Mech.2019 [cited 2023 Jan 31];103–61. Available from: https://www.igi-global.com/chapter/cryogenic-treatment-of-polymermwcnt-nano-

composites-for-mechanical-and-tribological-applications/www.igi-global.com/chapter/cryogenic-treatment-of-polymermwcnt-nano-composites-for-mechanical-and-tribological-applications/225625

11. Unal H, Mimaroglu A. Friction and wear performance of polyamide 6 and graphite and wax polyamide 6 composites under dry sliding conditions. Wear 2012;289:132–7.

12. Chen J, Zhu J, Luo Y, Wu H, Guo S, Qiu J. Achieving enhanced interfacial adhesion and highly oriented structure in PA6/Graphite composites for excellent tribological performance. Compos. Sci. Technol. 2022;229:109719.

13. Chopra S, Batthula S, Deshmukh K, Peshwe D. Tribological Behaviour of Multi-Walled Carbon Nanotubes (MWCNT) Filled Polybutylene Terephthalate (PBT) Nanocomposites. Trans. Indian Inst. Met. 2017;70:801–7.

14. Indumathi J, Bijwe J, Ghosh AK, Fahim M, Krishnaraj N. Wear of cryo-treated engineering polymers and composites. Wear 1999;225–229:343–53.

15. Theiler G, Gradt T. Friction and Wear of Polymer Materials at Cryogenic Temperatures [Internet]. In: Kalia S, Fu SY, editors. Polymers at Cryogenic Temperatures. Berlin, Heidelberg: Springer; 2013 [cited 2023 Feb 11]. page 41–58.Available from: https://doi.org/10.1007/978-3-642-35335-2_3

16. Demirci M, Bagci M. Erosion Resistance of CFRP Composite Materials with Different Fiber Weaves Exposed to Cryogenic Treatment. Tribol. Trans. 2021;64:82–90.

17. Deshmukh KA, Pode GR, Roy SR, Gupte BK, Deshmukh AD, Chopra S, et al. Effect of Cryo-Ageing at Liquid Nitrogen Temperature and Subsequent Thermal-Annealing on the Interface of Talc Filled Polypropylene with Different Particle Size. Trans. Indian Inst. Met. 2018;71:403–9.

18. Alajmi M, Alrashdan KR, Alsaeed T, Shalwan A. Tribological characteristics of graphite epoxy composites using adhesive wear experiments. J. Mater. Res. Technol. 2020;9:13671–81.

19. McGee AC, Dharan CKH, Finnie I. Abrasive wear of graphite fiber-reinforced polymer composite materials. Wear 1987;114:97–107.

20. Gheisari R, Polycarpou AA. Tribological performance of graphite-filled polyimide and PTFE composites in oil-lubricated three-body abrasive conditions. Wear 2019;436–437:203044.

21. Vishal K, Rajkumar K. Dry sliding wear behavior of Poly Ether Ether Ketone (PEEK) reinforced with graphite and synthetic diamond particles. Diam. Relat. Mater. 2022;130:109404.

22. Chopra S, Deshmukh KA, Deshmukh AD, Gogte CL, Peshwe D. Prediction, evaluation and mechanism governing interphase strength in tensile fractured PA-6/MWCNT nanocomposites. Compos. Part Appl. Sci. Manuf. 2018;112:255–62.

23. Sharma K, Braun O, Tritsch S, Muff R, Hufenus R, Perret E. 2D Raman, ATR-FTIR, WAXD, SAXS and DSC data of PET mono- and PET/PA6 bicomponent filaments. Data Brief 2021;38:107416.

24. Vasanthan N, Salem DR. FTIR spectroscopic characterization of structural changes in polyamide-6 fibers during annealing and drawing. J. Polym. Sci. Part B Polym. Phys. 2001;39:536–47.

25. Uddin AJ, Gotoh Y, Ohkoshi Y, Nagura M, Endo R, Hara T. Hydration in a new semiaromatic polyamide observed by humidity-controlled dynamic viscoelastometry and X-ray diffraction. J. Polym. Sci. Part B Polym. Phys. 2005;43:1640–8.

26. Qu C, Tang Y, Wang D, Fan X, Li H, Liu C, et al. Improved processability of PA66-polyimide copolymers with different polyimide contents. J. Appl. Polym. Sci. 2021;138:49640.

27. Tong X, Wang Z, Zhang ML, Wang XJ, Zhang G, Long SR, et al. Synthesis, Characterization and Non-Isothermal Crystallization Kinetics of a New Family of Poly (Ether-Block-Amide)s Based on Nylon 10T/10I. Polymers 2021;13:72.

28. Umar M, Ofem MI, Anwar AS, Salisu AG. Thermo gravimetric analysis (TGA) of PA6/G and PA6/GNP composites using two processing streams. J. King Saud Univ. - Eng. Sci. 2022;34:77–87.

29. Lin Y, Hill DE, Bentley J, Allard LF, Sun YP. Characterization of Functionalized Single-Walled Carbon Nanotubes at Individual Nanotube-Thin Bundle Level. J. Phys. Chem. B 2003;107:10453–7.

30. Tagaya M, Motozuka S, Kobayashi T, Ikoma T, Tanaka J. Mechanochemical Preparation of 8-Hydroxyquinoline/Hydroxyapatite Hybrid Nanocrystals and Their Photofunctional Interfaces. Ind. Eng. Chem. Res. 2012;51:11294–300.

31. Ashby MF, Ferreira PJ, Schodek DL. Chapter 5 - Material Property Charts and Their Uses [Internet]. In: Ashby MF, Ferreira PJ, Schodek DL, editors. Nanomaterials, Nanotechnologies and Design. Boston: Butterworth-Heinemann; 2009 [cited 2023 Feb 14]. page 147–76.Available from: https://www.sciencedirect.com/science/article/pii/B9780750681490000076

32. Ashby PM. Materials and Process Charts Compilation.

COMPARISON OF RESIDUAL STRESS GENERATION IN Al/Sic METAL MATRIX COMPOSITE AND DIE STEEL AFTER WIRE CUT ELECTRO DISCHARGE MACHINING

Yogesh Sable[a], Hanumant Dharmadhikari[b]

[a]Department of Mechanical Engineering, Jawaharlal Nehru Engineering College, Aurangabad, India

[b]Department of Mechanical Engineering, Marathwada Institute of Technology, Aurangabad, India

Abstract: *Use of Al/Sic composites are increasing due to their owing properties like high hardness, high strength, low density, high wear resistance, high impact strength. It is used in many industrial fields like aerospace, automobile, electrical and structural applications.*

WEDM process uses spark energy to remove the material, due to thermal process of material removal alteration happen at surface layer of base material called recast layer. Residual stresses are generated in this recast layer and heat affected zone which may affect the fatigue life of material. For longer life residual stress generated in recast layer and heat affected zone should be as lower as. This paper focus on residual stress generation in Al/Sic metal matrix composite and dies steel and their comparison after WEDM.

Keywords: *WEDM, Residual Stress, Al/Sic Composite, fatigue life*

1. Introduction

Metallic composite called Metal Matrix Composites are fabricated by combining base metal or alloy matrix and reinforcement in the form of fibres, whiskers, particles. Usually mostly used metal matrix is aluminium and its alloy due to their properties like ductility, machinability, formability, low density with stiffness, wear resistant and load carrying capacity of reinforcement material. Among various reinforcement material SiC is usually used because of its high hardness, high corrosive resistance and low cost. Al/Sic metal matrix composites offers combined advantages such as high strength to weight ratio, high wear resistance. This material use in automobile industry, aerospace industry, defense industry [1].

AISI D2 die steel is high carbon, high chromium steel, having high wear resistance, good toughness and Compressive strength, good deep-hardening properties and resistance to tempering. As it is good quality and high hardness material it is use for various applications like punching dies, blanking dies, forming dies, coining dies, etc.[2]

For machining hard material and complex shape with precision Wire Electro machining is widely used. In this machining process number of electrical sparks generated between two terminals normally workpiece as anode and wire as cathode in a dielectric medium and material is get removed from workpiece. The temperature developed by spark near machining surface is around 8000 ^{0}C to 12000 ^{0}C. The series of high temperature spark results in a noticeable phase transformation, at workpiece surface. The productivity of machining process is depend upon machining parameters, workpiece parameter and environmental condition. While machining any material a locally high temperature electric discharge created , which may cause change in mechanical as well as physical properties over machining surface and

also developed residual stresses in recast layer and heat affected zone. These residual stress may affect the fatigue life of the material and also creates some cracks or distortion near the surface.

Bulent Ekmekci [3] As non-homogeneities of recast layer is increases residual stress increases at machining surface which may affect the fatigue strength of material and may results in micro cracks over the machined surface. Ahmed Naif Ibrahim et.al [4] studied the effect of type of electrode , peak current and pulse on time on the surface residual stress and observed that with copper and graphite electrode less tensile residual stresses reaches at pulse current 22 and pulse on time 120 µs. Bulent Ekmekci et. al [5] Tensile residual stresses are produced by EDM .The maximum value of residual stress is almost equal to ultimate tensile strength of material. Then residual stress value falls down to compressive stress which depends on the thickness of material. J.P. Kruth et.al [6] observed that as number of finishing steps increasing residual stress and depth of penetration of residual stress decreases. F.Ghanem et.al [7] performed experiments on two hardenable steel X155CrMoV12 and C90 and two non hardenable steel X2CrNiMo 17-12-02 and X6Cr17 and studied the effect EDM process on this various material in terms of roughness, micro-hardness, residual stress and found that metallurgical transformation, surface hardening and residual stress are controlled by the type of material being used for machining. In case of non hardenable steel small growth of grain size in white layer were observed. A. G. Mamalis et.al [8] found that shot energy is responsible for intensity of residual stress and its penetration depth. Reza Bagherian Azhiri et. al [9] In presence of ultrasonic vibration Electro Discharge machining has done on AISI D2 steel and observed the effect of ultrasonic power, pulse on time, pulse off time, discharge current on MRR and surface roughness and residual stresses and result showed that pulse current and workpiece rotation have more effect on MRR and surface roughness and pulse on time is most significant parameter for residual stress. Ahmed Naif Al-Khazraji et.al [10] has performed EDM on AISI die steel by two type of electrode copper and graphite and input machining parameters like pulse current and pulse on time and observed that with graphite electrode and dielectric as kerosene produced minimum residual stress and comparatively graphite electrode copper electrode produces around 50% lower residual stress. Y.H.Guu et.al. [11] surface quality and machining damage by EDM were studied with machining parameter like pulse current and pulse on time and result showed that thickness of recast layer and surface roughness are increases as power input. EDM Process produces residual stress tensile in nature. Nagarajan Lenin et.al [12] fabricated Al-Lm25/ Fly ash/B4C hybrid composites and WEDM with pulse on time, pulse off time and wire feed rate to see the effect on volume removal rate and surface roughness. From results it is revile that GHO algorithm is best algorithm for increasing the volume removal rate and minimising the surface roughness values. Sanjay Kumar et. al [13] done WEDM on high carbon high chromium D2 steel and investigated the effect of duty cycle, peak current, and wire feed on residual stress, surface roughness and erosion rate. It was observed that interaction of high peak current and duty cycle produces high tensile residual stress. Behnam Khosrozadeh et.al [14] investigated the effect of ultrasonic-assisted EDM and powder mix dielectric EDM process on heat altered zone, micro cracks, surface roughness and residual

stress. It was found that magnitude of residual stress in ultrasonic- assisted EDM is lower than normal EDM and powder mix dielectric EDM process. J.F. Liu et.al [15] developed finite element model to predict residual stress distribution in EDM parts. Average residual stress is found maximum in below the top surface, which near about similar to experimental data. Low discharge energy is found suitable for lower tensile stress. S.L. Soo et.al [16] with low damage EDM generator and optimized trim-pass strategies, not found significant changes in fatigue life after WEDM and flank milling of Ti6246 material. Pujari Srinivasa Rao et.al [17] performed WEDM on 2014 T6 aluminum alloy and found more variation in the value of residual stress at various combination of WEDM parameters.

It is observed from various research article that, in case of WEDM as material, machining parameters changes variation in residual stress observed and also, it is noticed that less work has been done on effect of WEDM parameters on creation of residual stress and material being get machined.

2. Experimental Setup

The experiments were carried out on a wire-cut EDM machine (ELEKTRA SPRINTCUT 734) of Electronica Machine Tools Ltd. Diameter-0.25mm electrode of Brass wire used as electrode tool, di-electric fluid used as distilled water. Three Machining parameters- Pulse on time, Peak current and Pulse off time considered as input factors with three level as given in Table 1.

Table 1: Input factors and their levels

Factors	Levels		
	Level 1	**Level 2**	**Level 3**
Pulse on time	106	112	118
Peak Current	190	200	210
Pulse off time	30	34	38

For conducting experiments with three parameters and three levels full factorial design is used and total 27 trials are conducted for both type of materials.

The matrix material aluminum alloy LM-25 is high strength, high corrosive resistant material also its strength can be improve by heat treated conditions .LM25 mainly use for that application wherever we required good mechanical properties are required in desired shape or dimensions cast ability to achieved the desired standard. It has good machinability and mechanical properties. Following is the chemical composition of material

Table 2: Chemical Composition of Aluminum Alloy LM-25

Material	Copper	Magnesium	Silicon	Iron	Manganese	Nickel	Zinc	Lead	Tin	Titanium	Aluminum
LM25	0.1%	0.2-0.45%	6.5-7.5%	0.5 %	0.3 %	0.1%	0.1%	0.1%	0.05%	0.2%	Remainder

Reinforcement material SiCis an artificial (man-made) mineral known for its very high hardness and strength, abrasion resistance, chemical and thermal stability, high melting point, oxidation resistance, high erosion resistance, etc. for reinforcement powder form 1200 grit SiC is used. Aluminum alloy-SiC composite are fabricated by stir casting process.

D2 steel is high-carbon, high-chromium tool steel. It has high strength, high toughness, high hardness, high wear and abrasion resistant properties. It is heat treatable and can improve its hardness by heat treatment. Following is the chemical composition of material

Table 3: Chemical Composition of D2 die steel

Material	Carbon	Manganese	Silicon	Cobalt	Chromium	Molybdenum	Vanadium	Phosphorus	Nickel	Copper	Sulphur	Iron
D2	1.50%	0.60%	0.60%	1%	11%	0.7%	1.10%	0.03%	0.30%	0.25%	0.03%	Remainder

3. Result and Discussion

While Wire cut electro-discharge machining high temperature discharge generated near the surface to remove material, because this thermal process residual stresses are set up in recast layer and heat affected zone. The surface residual stress is important factor for the fatigue life of engineering products. Therefore, as low as residual stress, more will be fatigue life of material. The measurement of residual stress has done on XRD, for that suitable sized workpiece machined on WEDM. The retained layer of wire and dielectric was cleaned by very fine grit paper. Contaminations on the surface were cleaned using acetone solution.

X-ray Residual Stress Analyzer used for measuring the residual stress in Wire-EDMed machined surfaces. A number of independent X-ray runs at different ψ angles were performed to calculate residual stresses. The measurement depth were taken up to 50 µm. Following table no.4 & 5 shows values of experimentation with residual stress developed in Al/Sic and D2 die steel material respectively.

Table 4: Experimentation runs with Residual Stress for Al/SiC Metal matrix composite

Sr. No.	Pulse on time (µs)	Peak current (A)	Pulse off time (µs)	Residual Stress (MPa)
1	106	190	30	52.3
2	106	200	30	71.3
3	106	210	30	81.5
4	106	190	34	-34.2
5	106	200	34	62.5
6	106	210	34	101.2
7	106	190	38	72.3
8	106	200	38	91.3
9	106	210	38	136.2
10	112	190	30	61.3
11	112	200	30	93.2
12	112	210	30	-4.5
13	112	190	34	-42.3
14	112	200	34	138.2
15	112	210	34	124.5
16	112	190	38	-90.2
17	112	200	38	95.4
18	112	210	38	-136.4
19	118	190	30	124.3
20	118	200	30	114.2
21	118	210	30	122.5
22	118	190	34	98.2
23	118	200	34	131.1
24	118	210	34	123.1
25	118	190	38	98.3
26	118	200	38	126.5
27	118	210	38	124.5

Aluminum alloy having melting temperature of 800-900 0C and for reinforced material SiC it is 2600-2730 0C where as for die steel having melting temperature range of 1300-1550 0C and WEDM produces spark in the temperature range of 8000-12000 0C. After machining on WEDM solidification process mainly occurs in three phases. The first is removed molten material

Table 5: Experimentation runs with Residual Stress for De die steel material

Sr. No.	Pulse on time (µs)	Peak current (A)	Pulse off time (µs)	Residual Stress (MPa)
1	106	190	30	240
2	106	200	30	224
3	106	210	30	198
4	106	190	34	186
5	106	200	34	202
6	106	210	34	214
7	106	190	38	144
8	106	200	38	218
9	106	210	38	266
10	112	190	30	341
11	112	200	30	218
12	112	210	30	267
13	112	190	34	336
14	112	200	34	332
15	112	210	34	294
16	112	190	38	184
17	112	200	38	249
18	112	210	38	356
19	118	190	30	344
20	118	200	30	284
21	118	210	30	378
22	118	190	34	411
23	118	200	34	318
24	118	210	34	298
25	118	190	38	198
26	118	200	38	256
27	118	210	38	388

thrown into the working liquid solidifies when the working liquid cools and forms the debris. The second is that part of the molten material is thrown onto the corresponding electrode surface and cooled it is not more in case of WEDM and third, the residual materials that have not been removed from surface of work piece cooled on the surface of the work piece. For particle reinforced metal matrix composites, the coefficient of thermal expansion of matrix is different from that of particle. As the temperature rises, the internal stresses are released. Due to the difference in thermal expansion coefficient between the matrix material and the particles, the expansion of the matrix is much larger than that of the particles. In the expansion process, the matrix and the particles will inhibit each other and generate lower residual stresses and sometimes it is compressive stress, where as in case of die steel all particles having same coefficient of thermal expansion therefore particles not inhibit each other and forms higher residual stress near the machining surface. Fig. 2 shows the comparison of residual stress value for Al/SiC MMC and D2 steel material.

From fatigue life point of view tensile residual stress majorly influenced the fatigue life of material. As from above result maximum magnitude of tensile residual stress occur in D2 die steel, which may affect fatigue life as compare to Al/SiC , but tensile strength of D2 material is more as compared to Al/SiC MMC material.

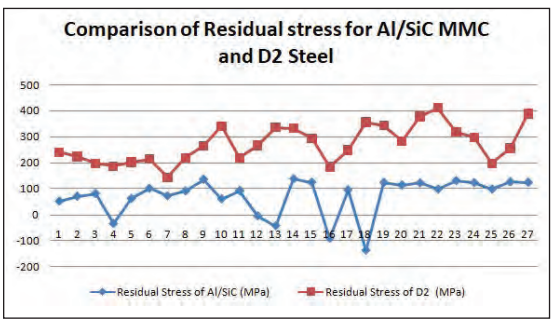

Fig. 1 Comparison of Residual stress for Al/SiC MMC and D2 Steel

4. Conclusion

Wire cut electro discharge machining has been done on Al/SiC metal matrix composite and D2 dies teel material with varying pulse one time, pulse off time and peak current at three levels. from obtained result it is conclude that

1. Tensile residual stress is induced after WEDM process while Al/SiC MMC and D2 steel WED machined expecting few values of Al/SiC.

2. Residual stress magnitude is more in case of D2 steel material as compared to Al/SiC MMC.

3. Tensile residual stress may affect fatigue life of material.

References:

1. Ji-Peng Chen, Lin Gu and Guo-Jian He "A review on conventional and nonconventional machining of SiC particle-reinforced aluminium matrix composites", Springer, Advance Manufacturing an International Journal, (2019).

2. Goutham Murari V.P.,Selvakumar G. and Chandrasekhara Sastry C.," Experimental Investigation ofWire-EDM Machining of Low Conductive Al-SiC-TiC Metal Matrix Composite" MDPI, Metals International Journal, Vol.10,(2020),pp.1-31

3. Bulent Ekmekci "Residual stresses and white layer in electric dischargemachining (EDM)" ,Elsevier, Applied Surface Science, 253 (2007), pp.9234-9240

4. Ahmed Naif, Samir Ali Amin and Saad Mahmood Ali "Surface Residual Stresses Induced by Shot Blast Peening after EDM of AISI D2 Die Steel using two types of Electrode",International Journal of current Engineering and Technology,Vol.5,issue No.1, (2015),pp.227-234

5. Bulent Ekmekci.A.Erman Tekkaya and Abdulkadir Erden, "A semi-empirical approach for residual stresses in electric discharge machining (EDM)" ,Elsevier, International Journal of Machine tools & Manufacture,46 (2006), pp.858-868

6. J.-P.Kruth,Ph.Bleys " Measuring residual stress caused by Wire EDM of tool steel", International Journal of Electrical Machining, No.5,(2000)

7. F.Ghanem, C. Braham and H.Sidhom "Influence of steel type on electrical discharge machined surface integrity", Elsevier, Journal of Materials Processing Technology, 142 (2003), pp.163-173

8. A.G.Mamalis,G.C.Vosniakos, and N.M. Vacevandis "Residual Stress Distribution and Structural Phenomena of High-Strength Steel Surfaces Due to EDM and Ball-Drop Forming" Annals of the CIRP Vol.37, issue 1,(1988),pp.531-535

9. Reza Bagherian Azhiri, Abolfazal Samani Bideskan, Farid Javidpour and Ramin Mehdizad Tekiyeh "Study on material removal rate, surface quality, and residual stress of AISI D2 tool steel in electrical discharge machining in presence of ultrasonic vibration effect", Springer, The International Journal of Advance Manufacturing Technology, (2018)

10. Dr. Ahmed Naif Al-Khazraji,Sr.Samir Ali Amin and Saad Mahmood Ali "Study the Effect of the Graphite Powder Mixing Electrical Discharge Machining on Creation of Surface Residual Stresses for AISI D2 Die Steel Using Design of Experiments" , Engineering and Technology Journal, Vol.33, Part(a),No.6,(2015)

11. Y.H.Guu, H. Hocheng, C.Y. Chou and C.S.Deng "Effect of electrical discharge machining on surface characteristics and machining damage of AISI D2 tool steel" Elsevier, Materials Science and Engineering, A 358 (2003),pp.37-43

12. Nagarajan Lenin, Mahalingam Sivakumar, Gurusamy Selvakumar, Devaraj Rajamani, Vinothkumar Sivalingam, Munish Kumar Gupta, Tadeusz Mikolajczyk and Danil Yurievich Pimenov "Optimization of Process Control Parameters for WEDM of Al-LM25/Fly Ash/B4C Hybrid Composites Using Evolutionary Algorithms: A Comparative Study ", MDPI, metals International Journal (2021)

13. Sanjay Kuamr, Sandeep Grover and R.S.Walla "Effect of hybrid wire EDM conditions on generation of residual stresses in machining of HCHCr D2 tool steel under ultrasonic vibration", Springer,International Journal on Interactive Design and Manufacturing (2018)

14. Behnam Khosrozadeh and Mohammadreza Shabgard "Effects of hybrid electrical discharge machining processes on surface integrity and residual stresses of Ti-6Al-4V titanium alloy", Springer, International Journal of advance Manufacturing Technology (2017)

15. J.F.Liu and Y.B.Guo "Residual Stress Modeling in Electric Discharge Machining (EDM) by Incorporating Massive Random Discharges" Elsevier ,Proceedis CIRP, 45, (2016),pp.299-302

16. S.L.Soo, M.T.Antar, D.K.Aspinwall, C. Sage, M.Cuttell, R.Perez and A.J.Winn "The effect of wire electrical discharge machining on the fatigue life of Ti-6Al-2Sn-4Zr-6Mo aerospace alloy", Elsevier, Procedia CIRP 6(2013),pp.215-219

17. Pujari Srinivas Rao, Koona Ramji and Beela Sayanarayana "Effect of wire EDM conditions on generation of residual stresses in machining of aluminum 2014 T6 alloy" ,Elsevier, Alexandria Engineering Journal (2016)

A SHORT REVIEW ON THE PROCESSING OF Ni-BASED SUPER-ALLOYS BY METAL ADDITIVE MANUFACTURING

Saroj Kumar Sahu[a], Adiraj Behera[b], Ajit Behera[c], Renu Prava Dalai[a]

[a]Department of Metallurgical & Materials Engineering, Veer Surendra Sai University of Technology, Burla, India

[b]Department of Metallurgical and Materials Engineering, GCE, Keonjhar, Odisha, India

[c]Department of Metallurgical and Materials Engineering, NIT, Rourkela, Odisha, India

Abstract: *Ni-based super-alloys are widely applied in aerospace, automobile, and energy industries (power plants) because they retain their high strength when working under high-temperature conditions. Conventional methods like melting-casting, investment casting, and powder metallurgy methods are developed for Ni-based super-alloys. However, these methods have certain limitations: segregation, near net shape, and material loss during machining in the melting-casting technique, whereas formation of prior particle boundaries in the powder metallurgy method. But these limitations are not observed in the investment casting method, but the process is not cost-effective to produce a large number of products. Recently, few researchers take attempted to process the Ni-based super-alloys using a metal additive manufacturing process to get near net shape products without the prior particle boundaries and segregation at a reasonable cost compared to investment casting. The two commercially available Ni-based super-alloys are Inconel 625 and Inconel 718, processed by metal additive manufacturing (MAM). The selective laser melting (SLM) process is based on the principle of layer-by-layer material incremental MAM which produce a full density product without segregation of the powders. Hence, this review is based on the processing of Ni-based super-alloys of the IN718 and IN625 generally used in the turbine blades.*

Keywords: *Ni-based super-alloys; metal additive manufacturing; selective laser melting; powder metallurgy*

1. Introduction

Ni-based super-alloys are widely applied in aerospace, automobile, and energy industries (power plants) because they retain their high strength when working under high-temperature conditions. Nickel-based super-alloys retain their uniquemechanical and corrosion properties at high temperaturesused in gas-turbine engine components [1-4]. Nickel-based super-alloys are developed by melting-casting, investment casting, and powder metallurgy routes. Particle segregation, agglomeration, formation of prior particle boundaries, and high cost (investment casting) are the limitations of conventional methods. In this regard, MAM techniques produce complex parts with near net shape than conventional techniques [5-7]. The metal additive manufacturing(MAM) of Ni-based super-alloys is a new technique which emerging in the field of manufacturing industries.The Ni-based super-alloys are strengthened due to the γ′, γ″precipitates and carbides[8].Conventional methods like melting-casting, investment casting, and powder metallurgy methods are developed for Ni-based super-alloys. However, these methods have certain limitations: segregation, near net shape, and material loss during machining in the melting-casting technique, whereas formation of prior particle boundaries in the powder metallurgy method. But these limitations are not observed in the investment casting method, but the process is not cost-effective to produce a large number of products. Therefore the MAM process provides a better solution to these problems.

2. Different types of additive manufacturing processes used to developNi-based super-alloy

Recently Ni-based super-alloys are mainly produced through different MMA manufacturing techniques such as SLM, EBM, DED, DMD, USAM,etc. [9-11].Table 1 revealed the detailed classification of the MA manufacturing process. There are different types of metal additive manufacturing. For the fabrication of Ni-based super-alloys SLM, a powder-based process is commonly used which provides better mechanical properties and fine cellular or columnar microstructure compared to the other methods. The parts produced by this method provide full density and better performance with good accuracy. As a result, SLM meets the demand of different industries where that need lightweight and complex parts.

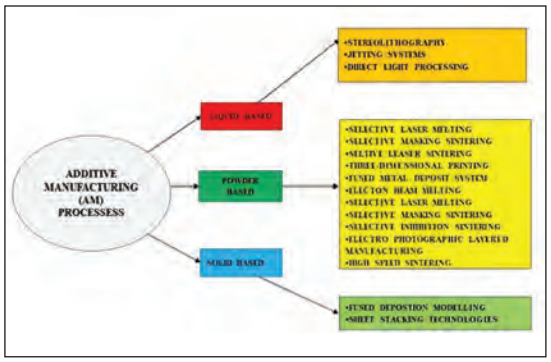

Fig. 1 Various Types of Additive Manufacturing Processes

2.1 Selective Laser Melting (SLM)

A laser selectively meltsthe successive layers of powder and develops a layer-by-layer product during the processing of the Ni-based super-alloys[11-14]. This process is also named a laser powder bed fusion process. In this process, various alloying elements like Cu, Al, Ti, and Cr, can be added to develop the Co-based and Ni-based super-alloys.This technique produces complex or intricate metal parts easily with better properties compared to the other AM processes. Nowadays SLM is very popular because of its higher rate of deposition and to develop a large part with minimum cost. Fig.2 shows a schematic of a lab-built SLM experiment setup to fabricate the super-alloys.Figure 3 depicts thespecimen orientations during SLM processing on a substrate.

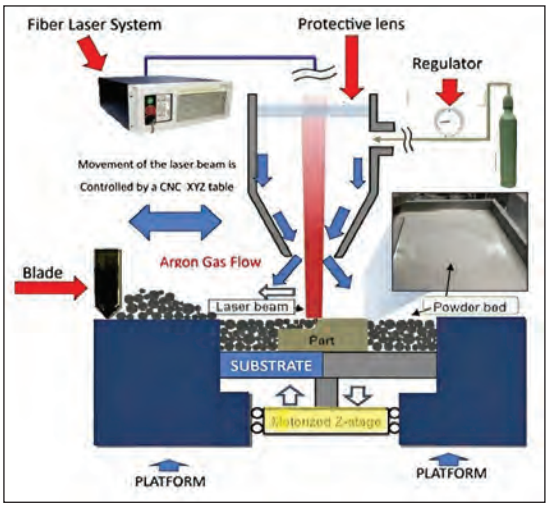

Fig.2. Schematic of a lab-built SLM experiment setup

2.2 SLM of IN718

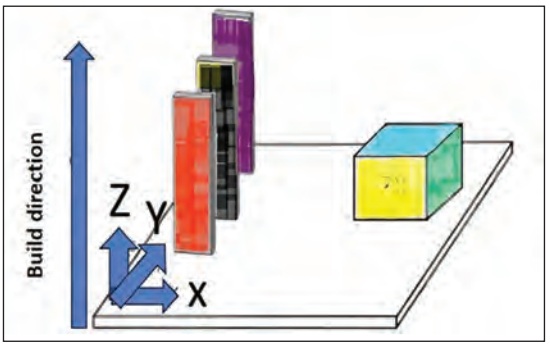

Fig. 3. Specimen orientations during SLM processing

IN718 is a precipitation-strengthened or hardened alloy and it retains its high strength properties at high temperatures [18, 19]. IN718 contains a higher amount of Al and Ti with Nb. The precipitation strengthening in IN718 is due to the presence of Nb, Al, and Ti because they form intermetallic compounds such as γ′ (Ni_3(Al, Ti, Nb)), γ″ (Ni_3Nb), and δ (Ni_3Nb) [18, 20]. However, δ phase is more stable and retains the high strength properties at high temperature. The γ″ phase can be converted to the δ phase above 650 °C [21]. Processing of IN718 super-alloy using conventional methods creates problems like segregation, shrinkage, and expensive. Low cracking tendency and good formability of the SLM process is the most suitable method to develop the IN718 Ni-based super-alloy. However, controlling the processing parameters of the SLM process eliminates the micro-defects [20].

2.2.1 Heat treatment of IN718 after SLM

Heat treatment after the SLM process creates a homogeneous microstructure and precipitates the different strengthening phases. It also helps to dissolve the undesirable brittle lave phases [22]. The presence of the brittle lave phases decreases the mechanical properties of IN718.SLM processgenerally precipitates these phases in the interdendritic regions due tolaser irradiation. Wang et al.[23] observed SLM processed IN718 samples have no precipitates (γ′and γ′′). To precipitate these strengthening phases and to dissolvethe undesirable brittle lave phases heat treatment is a necessary step after SLM processing. The common heat treatment procedure for precipitation-strengthened Ni-based super-alloys consists of solution plus aging treatment. Li et al.[24] suggested that a proper solution temperature is able to enhance the performance of IN718 fabricated by the SLM method. Because the strengthening precipitates dissolve at a higher temperature whereas lower temperaturesare not able to precipitate the strengthening phases. Ni et al. reported that aging treatment after the solution treatment completed the precipitation process and increase the fraction of the strengthening precipitatephasesup to 45.5% compared to the IN718 samples without heat treatment [25].

2.2.2 Hot isostatic pressing (HIP) of the SLM processed IN718

HIP is generally used to close the pores generated in the additive manufacturing engineering parts and improve the mechanical properties. The HIP is able to dissolve the undesirable lave phases due to the high temperature used in the process. It redistributes the alloying elements and formsan equiaxed γ phase. Kuo et al. [26] reported that without HIP there is an accumulation of the δ phase precipitates in the interdendritic regions. Accumulation of these precipitates leads to premature failure of the SLM-processed parts.

Table 1 Summary of the process parameters in the SLM process[32]

Powder-related properties	Laser-related properties	Powder-bed-related properties
Chemical Composition	Laser type	Deposition strategy
Particle size and shape	Laser power	Layer thickness
Particle size distribution	Sport size	Powder-bed density
Surface morphology	Defocusing	
Internal porosity	Scanning speed	
Powder flowability	Scanning strategy	Building chamber atmosphere
Apparent density	Hatch spacing	

2.3 SLM of IN625

IN625, superalloys, was developed to use in the aerospace industries for gas turbine engines but its unique properties attract other industries [27]. Solution and precipitation strengthening

is due to the presence of the alloying elements Cr, Mo, and Nb. Machining of the IN625 alloy is difficult due to its very high strength, as a result, processing of the IN625 alloy is not favorable by the traditional methods. IN625 developed by the SLM process shows columnar microstructure with elongated grains and has a γ-FCC matrix [28, 29]. Due to a higher rate of cooling during the SLM process,complete precipitation ofthe γ′′ intermetallic phasesis not possible. The heat treatment after the SLM processing precipitates the γ′′ (Ni_3Nb) and carbides (MC, M6C, and M23C). Li et al. [30] reported that heat treatment changes the microstructure and hardness of the IN625 developed by the SLM method. Afkhamiet al.[31] reported that the fatigue resistance property of the SLM processed parts deteriorates due to poor surface finish. However, HIP improves the fatigue resistance property of IN625. C. Li et al.[16] observed that fully dense IN625 alloy is developed by the SLM method and heat treatment after SLM processing provides better mechanical properties.Table 1 represents the different process parameters required during the SLM processing. However, to obtain an SLM part with a good surface finish, near net shape, and better mechanical properties optimization of the process parameters is one of the most essential steps.

2.3.1 Heat treatment of IN 625 after SLM

Heat treatment of IN625 developed by SLM dissolves the undesirable brittle lave phases. This heat treatment precipitates the different strengthening phases (γ′ and γ′′) and improves the mechanical properties of the superalloy. [33] Hu et al. [34] observed a higher solution temperature decreases the volume fraction and size of the lave phases. Also mentioned, yield strength and hardness decrease when the solution temperature increases. However, elongation increases the yield strength of the superalloy. Hu et al. [35] suggested that a proper solution temperature enhances the performance of IN625 fabricated by the SLM process. Li et al. [36] studied the original microstructure of the IN625 superalloy developed by SLM and observed that the microstructure consists of austenite with no carbide precipitation or laves phases. Li et al. [37] reported that heat treatment recrystallizes the microstructures, increases the grain size, reduces dislocation density, and reduces tensile residual stress in IN625 samples produced by SLM.

3. Conclusions

The following conclusions are obtained on the review of SLM in IN718 and IN625

(i) Processing of IN718 and IN625 super-alloys by conventional methods generates problems like segregation, shrinkage, difficulty in machining, and expensive (investment casting).

(ii) The low cracking tendency and good formability of the SLM process make the process suitable for the production of high-strength IN718 and IN625 Ni-based super-alloys.

(iii) HIP and proper heat treatment are necessary to obtain better mechanical properties and dissolve the brittle lave phases in IN718.

(iv) A fully dense IN625 alloy can be developed by the SLM method and heat treatment after SLM processing provides better mechanical properties.

Acknowledgment

The authors acknowledge Department of MME, VSSUT Burla, Odisha, India, to provide the necessary facilities to complete this work

4. References

1. Zhong Z, Gu Y, Yuan Y. Microstructural stability and mechanical properties of a newly developed Ni–Fe-base superalloy. *Mater SciEng* A 2015; 622: 101-107.
2. Tan L, Li Y, He G, Liu F, Nie Y, Jiang L. Optimized hot workability of a powder metallurgy nickel-base superalloy. *MaterCharac* 2019;147: 340-352.
3. Sahu, SK., Mishra, DK., Behera, A., Dalai, RP.An overview on the effect of heat-treatment and cooling rates on Ni-based superalloys. *Mater Proc* 2021;.47: 3309-3312.
4. Smith TM, Gabb TP, Kantzos CA, Thompson AC, Sudbrack CK, West B, Ellis DL, Bowman CL, *J Alloy Compd*2021; 873:159789.
5. Li X, Zhu Z, Liu K, Shi J, Zou X, Lu X, Cao G, Wu S. Enhanced strength-ductility synergy in a selective laser melted Inconel 718 superalloy by refining γ precipitates.*Mater Let* 2023; 333:133678.
6. Jia Q, Gu D. Selective laser melting additive manufacturing of Inconel 718 superalloy parts: Densification, microstructure and properties. *J Alloy Compd* 2014; 585: 713-721.
7. Goncharov IS, Razumov NG, Silin AO, Ozerskoi NE, Shamshurin AI, Kim A, Popovich AA. Synthesis of Nb-based powder alloy by mechanical alloying and plasma spheroidization processes for additive manufacturing. *MaterLet* 2019; 245: 188-191.
8. Jiang R, Song YD, Reed PA. Fatigue crack growth mechanisms in powder metallurgy Ni-based superalloys—A review. *I JFat* 2020;141:105887.
9. Jia Q, Gu D. Selective laser melting additive manufacturing of Inconel 718 superalloy parts: Densification, microstructure and properties. *J Alloys Compd* 2014; 585:713-721.
10. Zhang F, Levine L E, Allen AJ, Stoudt MR, Lindwall G, Lass EA, Campbell CE . Effect of heat treatment on the microstructural evolution of a nickel-based superalloy additive-manufactured by laser powder bed fusion. *Acta mater* 2018; 152: 200-214.
11. Gonzaleza JA, Mirelesa J, Staffordb SW, Pereza MA, Terrazasa CA, Wickera RB. Characterization of Inconel 625 fabricated using powder-bed-based additive manufacturing technologies. *J Mater Proces Tech* 2019; 264: 200–210.
12. Mostafaei A, Neelapu SHVR, Kisailus C, Nath LM, Jacobs TD, Chmielus,M. Characterizing surface finish and fatigue behavior in binder-jet 3D-printed nickel-based superalloy 625. *Add Manuf* 2018; 24: 200-209.
13. Nath P, Nanda D, Dinda GP, Sen I. Assessment of microstructural evolution and mechanical properties of laser metal deposited 316L stainless steel. *J Mater EngPerfor*2021;30: 6996-7006.
14. Nagarajan B, Hu Z, Song X, Zhai W, WeiJ. Development of Micro Selective Laser Melting: The State of the Art and Future Perspectives. *Engineering* 2019; 5: 702-720.
15. Zhang F, Levine LE, Allen AJ, Stoudt MR, Lindwall G, Lass EA, Campbell CE. Effect of heat treatment on the microstructural evolution of a nickel-based superalloy additive-manufactured by laser powder bed fusion. *Add man* 2018;152:200-214.
16. Li C, White R, Fang XY, Weaver M, Guo YB. Microstructure evolution characteristics of Inconel 625 alloy from selective laser melting to heat treatment. *Mater SciEng* A2017;705:20-31.
17. InaekyanK, KreitcbergA, Turenne S, Brailovski V.Microstructure and mechanical properties of laser powder bed-fused IN625 alloy. *Mater SciEng* A 2019;768: 138481.
18. Teng Q, Li S, Wei Q, ShiY.Investigation on the influence of heat treatment on Inconel 718 fabricated by selective laser melting: Microstructure and high temperature tensile property. *J Man Process* 2021; 61:35-45.
19. Amirjan M, Bozorg M, Sakiani H .Investigation of microstructure and corrosion behavior of IN718 superalloy fabricated by selective laser melting. *Mater ChemPhy* 2021; 263:124368.
20. McLouth, TD,Witkin DB, Bean GE, Sitzman SD, Adams PM, Lohser JR, Yang JM, Zaldivar RJ .Variations in ambient and elevated temperature mechanical behavior of IN718 manufactured by selective laser melting via process parameter control., *Mater SciEng A* 2020; 780:139184.
21. Moussaoui K, Rubio W, Mousseigne M, Sultan T, Rezai F .Effects of Selective Laser Melting additive manufacturing parameters of Inconel 718 on porosity, microstructure and mechanical properties. *Mater SciEng A* 2018; 735:182-190.

22. Cao M, Zhang D, Gao Y, Chen R, Huang G, Feng Z, Poprawe R, Henrich J, ZieglerS.The effect of homogenization temperature on the microstructure and high temperature mechanical performance of SLM-fabricated IN718 alloy. *Mater SciEng* A 2021; 801:140427.

23. Wang Z, Guan K, Gao M, Li X, Chen X, Zeng,X. The microstructure and mechanical properties of deposited-IN718 by selective laser melting. *J Alloy Compd* 2012; 513:518-523.

24. Li J, Zhao Z, Bai P, Qu H, Liu B, Li L, Wu L, Guan R, Liu H, Guo Z. Microstructural evolution and mechanical properties of IN718 alloy fabricated by selective laser melting following different heat treatments. *J Alloy Compd* 2019; 772: 861-870.

25. Ni M, Liu S, Chen C, Li R, Zhang X, Zhou K .Effect of heat treatment on the microstructural evolution of a precipitation-hardened superalloy produced by selective laser melting. *Mater Sci Eng* A 2019; 748:275-285.

26. Kuo Y, Horikawa S,Kakehi K .Effects of build direction and heat treatment on creep properties of Ni-base superalloy built up by additive manufacturing. *Scr Mater* 2017; 12974–12978.

27. Levy GN, Schindel R,Kruth J. Rapid manufacturing and rapid tooling with layer manufacturing (LM) technologies, state of the art and future perspectives. *CIRP Ann Manuf Technol* 2003; 52:589–609.

28. Amato K, Hernandez J, Murr L, Martinez E, Gaytan S, Shindo P, Collins S. Comparison of microstructures and properties for a Ni-base superalloy (alloy 625) fabricated by electron beam melting. *J Mater Sci Res* 2012; 1: 3.

29. Kreitcberg A, Brailovski V, Turenne S. Effect of heat treatment and hot isostatic pressing on the microstructure and mechanical properties of Inconel 625 alloy processed by laser powder bed fusion. *Mater SciEng* 2017;689:1-10.

30. Li S, Wei Q, Shi Y, Zhu Z, Zhang D. Microstructure characteristics of Inconel 625 superalloy manufactured by selective laser melting. *J Mater Sci Technol* 2015; 31: 946–952.

31. Afkhami S, Dabiri M, Alavi SH, Bjork T, Salminen A. Fatigue characteristics of steels manufactured by selective laser melting. *Inter J Fatigue* 2019; 122:72-83.

32. Nagarajan B, Hu Z, Song X, Zhai W, Wei J.Development of Micro Selective Laser Melting: The State of the Art and Future Perspectives. *Engineering* 2019;5:702–720.

33. Kreitcberg A, Turenne VBS. Effect of heat treatment and hot isostatic pressing on the microstructure and mechanical properties of Inconel 625 alloy processed by laser powder bed fusion. *Mater Sci Eng* A 2017;689:1-10.

34. Hu YL, Lin X, Zhang SY, Jiang YM, Lu XF, Yang HO, Huang WD. Effect of solution heat treatment on the microstructure and mechanical properties of Inconel 625 superalloy fabricated by laser solid forming. *J Alloys Comp.* 2018; 767: 330-344.

35. Hu XA, Zhao GL, Liu FC. Microstructure and mechanical behavior of Inconel 625 alloy processed by selective laser melting at high temperature up to 1000 °C. *Rare Met* 2020; 39: 1181–1189.

36. Li S, Wei Q, Shi Y, Zhu Z, Zhang D. Microstructure Characteristics of Inconel 625 Superalloy Manufactured by Selective Laser Melting. *J Mater Sci Tech.*2015; 31: 946-952.

37. Li C, White R, Fang XY, Weaver M, Guo YB. Microstructure evolution characteristics of Inconel 625 alloy from selective laser melting to heat treatment. *Mater SciEng*: A 2017; 705: 20-31.

THE BROAD USAGE SPECTRUM OF THERMOELECTRICITY FROM LOW TEMPERATURE PHOTOVOLTAIC TO HIGH TEMPERATURE FURNACES: AN OVERVIEW

Vaishali Sushil Poddar*[1], Dr. N. B. Dhokey[2]

[1] Department of Materials and Metallurgical Engineering, National Institute of Advanced Manufacturing Technology (NIAMT), Ranchi, India.

[2] Dept of Metallurgy and Materials Science, COEP Technological University, Pune, India.

*Corresponding author: vspoddar@niamt.ac.in

Abstract: *Thermoelectric (TE) material is a need of future as it provides a means for harvesting waste heat energy and is also the cleanest form of energy. Many types of TE have attracted the attention in the last years because of their technological potential in the field of optoelectronics, light emitting diodes (LEDs), medical, aerospace and defense applications due to the thermoelectric conversion properties, chemical stability and non-toxicity. Not only this, TE can be adjoint to other renewable energy sources like photovoltaic (PV) to improve their efficiency. As compared to commercially available PV Cells whose efficiency usually varies in between 15 to 20 %, there is around 6.5% rise in overall thermal efficiency of PV-TE-EC (Evaporative Cooling) based hybrid power generator using suitable solar concentrator with the operating temperature of around 85°C. In high temperature applications at 750-800°C, β-$FeSi_2$ based TE is the ecofriendly and suitable material for high temperature application. The power output is calculated for 29 legs of p-type and n-type β-$FeSi_2$ and the maximum power output and power density are 4.1 mW and 0.0284 $mWcm^{-2}$ respectively. Using necessary relations in mathematical modeling a proper combination of eco-friendly transition metal silicides in each multi-segmented TE leg is proposed. For the designed multi-segmented TE leg, to be used in 500 – 1200 K temperature range, the effective Seebeck coefficient, circuit voltage and effective Seebeck – Thomson coefficient for an unicouple is determined to be 149 μVK^{-1}, 0.104 V and 277 μVK^{-1} respectively. The maximum power output obtained is around four times what is obtained in an only β-$FeSi_2$ based TE.*

Keywords: *thermoelectric; Seebeck effect; TEG module; power; multi-segmented thermoelectric.*

1. Introduction:

Various techniques have been employed for synthesis of thermoelectrics (TEs), but for many of them there is no such specific route which can lead to their industry level synthesis. An ideal TE material should be a phonon glass and an electron crystal, which means that the materials should have a low lattice thermal conductivity just like glass, and a high electrical conductivity just like in a crystal [1].

According to the second law of thermodynamics, the energy input to a system is never completely converted to usable energy output. The difference between the two constitutes the unutilized heat and it is though in variable quantities is available in almost every system. Thermoelectric materials, used in power generation, scavenge the unutilized heat from the source and convert it to a usable electrical form of energy. The unutilized heat may be of high temperature, medium temperature, or low temperature grade. That means heat is dumped, for example from industrial processes like hot metallurgical processing (high temperature: greater than 600°C), from exhaust gases released by the combustion units (medium temperature: 250 to 600°C) or from hot surfaces of the indirectly involved processing units (low temperature: less than 250°C) into the environment causing

thermal pollution [2]. Surprisingly, around 66% of the unutilized heat in industries is available in the low temperature range of around 66-230°C. TE can work as a renewable energy source in low temperature regime or as a supplement to conventional energy sources in high temperature regime [2-3]. In the medium temperature range, TE can work in either ways depending on the system or the purpose for which it is used [2,4]. Figure 1 illustrates the mostly preferred TE material to be used at a particular temperature [3-7]. Therefore, TE comes under the category of sustainable energy-efficient technology with the additional advantages of simple configuration, no moving parts, no vibration, no noise, no pollution, and high stability.

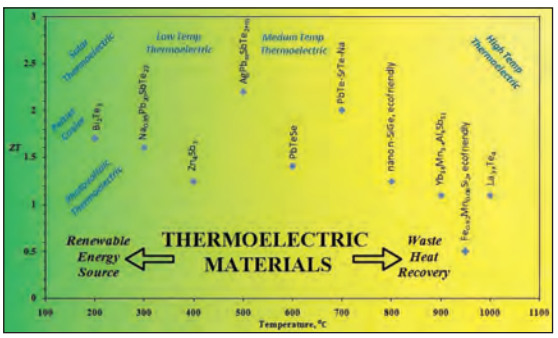

Fig. 1 Highest ZT Thermoelectric materials to be used at various temperatures for various applications.

The TE uses Peltier effect for cooling and Seebeck effect for energy generation. Some TEs are good as Peltier coolers, some are good as TEGs and few are good in both refrigeration and power generation. Few examples of each of the category are cited in Fig. 2. To make many of the TEs multidimensional suitable measures need to be taken in two perspectives: (1) Joule heat to be kept as minimum as possible; and (2) No increment in lattice thermal conductivity due to increasing temperature. This can be achieved by suitable use of doping, nanostructuration, band engineering and use of proper set of materials (e.g. use of oxide dielectric layer in between the layers of TE material) [7-13].

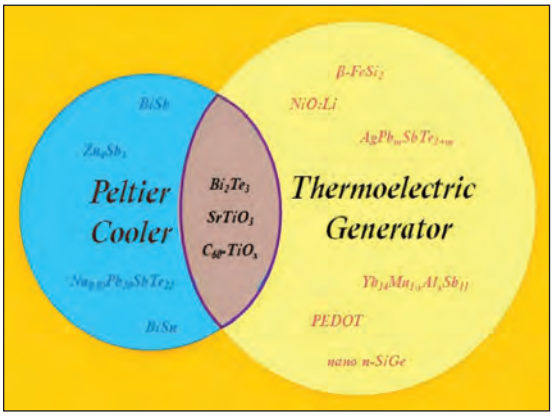

Fig. 2 Thermoelectric materials classification with respect to the power generation mode and refrigeration mode.

However, the challenge in using TE is that for a particular temperature, the thermoelectric system should be inclusive to all forms of heat source, be able to run continuously, have a long life, are low cost and are light in weight. For a particular TE, the TE performance index, figure-of-merit, ZT, is maximum over a narrow temperature range and it decreases beyond that range. For example, PbTe has ZT of 1.9 between 250 – 300 °C, but beyond this temperature the ZT is low [14-15]. For such low ZT temperatures, another TE need to be employed.

2. A Typical TE Circuit and its Components:

TE is characterized by its dimensionless Figure of merit (ZT) as given in Eq. (1).

$$ZT = \frac{S^2 \sigma T}{k} \quad \ldots (1)$$

where S, k, σ and T are the Seebeck coefficient (μV K^{-1}), thermal conductivity (W m^{-1} K^{-1}), electrical conductivity (Ω^{-1} m^{-1}) and absolute working temperature (K) respectively [4-5]. Eq. (1) can be pictorially represented as shown in Fig. 3 (a). The TE module is designed using p-type and n-type TE material legs. Various characteristics are required to be investigated to determine the maximum output power from the prepared TE module. These legs are connected electrically in series but thermally in parallel as shown in Fig. 3(b)-(c). The electrical analogy for the TE module is shown in Fig. 3(d). On both top and bottom surfaces of the TE circuit, the SiC plate, alumina plate and silver foil are represented as capacitors with their respective resistances. Across the TE circuit, temperatures Th and Tc are sustained which results in charge flow. The electrical circuit with grey background in Fig. 3(d) summarizes the circuit to determine the Seebeck coefficient. The working model to apply load resistance and evaluate the TE power output is shown in Fig. 3(e).

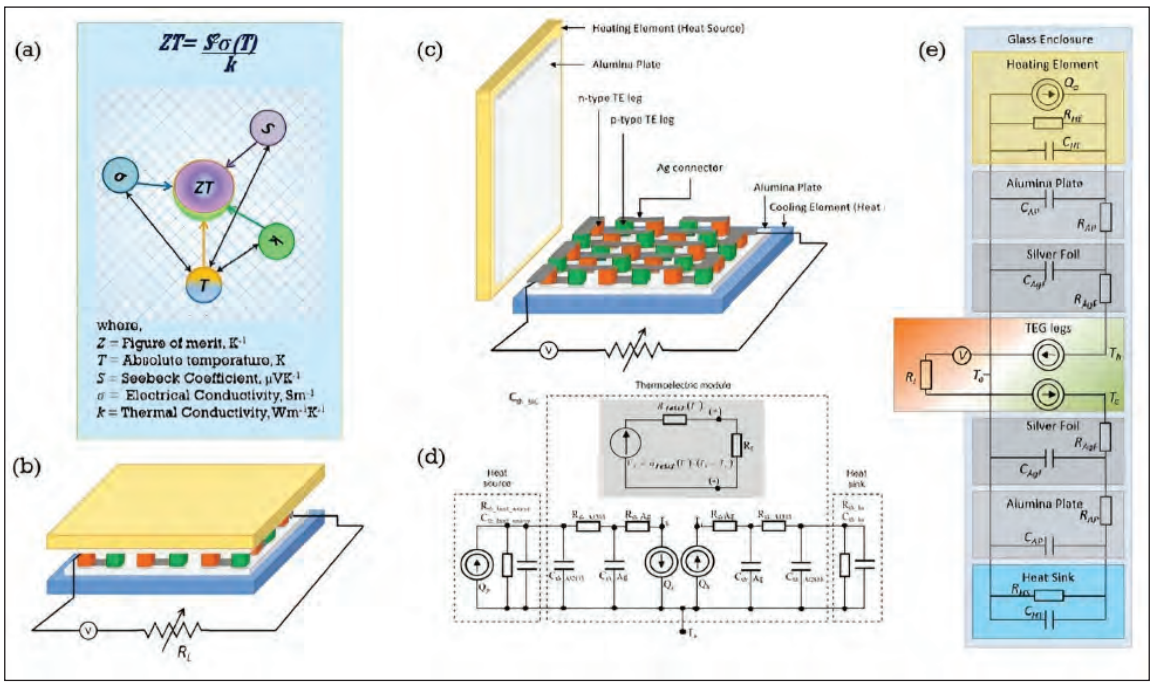

Fig.3 Schematic of a Thermoelectric: (a) Dependency of Figure-of-Merit, ZT of the TE material on various parameters (b) Appearance of the complete TE assembly, (c) Various parts of the TE assembly, (d) Electrical analogy of the TEG module, (e) Working model of the TEG module.

3. Low Temperature Applications: Photovoltaic (PV)

The usage of photovoltaic (PV) cell for electricity generation increased appreciably from last few decades owing to its environmental sustainability, availability, and applicability. However, in PV most of the solar energy gets dissipated in the form of heat into the PV system. This waste heat causes increase in temperature of PV cell and degrades its efficiency and

performance. In the current context, efforts are made to improve the efficiency by utilizing this dissipated heat. One of the ways is to use low temperature thermoelectric (TE), based on the Seebeck effect, along with the PV cell. The overall efficiency with respect to temperature of hybrid Photovoltaic-Thermoelectric (PV-TE) is 0.6 – 1.91% more than PV alone.

Both PV and TE systems depend strongly on temperature and thus to reduce the temperature and improve the performance of PV-TE hybrid system, effective and affordable direct evaporative cooling (EC) system was used in this study. The mathematical model studied for performance evaluation was based on cascaded hybrid Photovoltaic-Thermoelectric-Direct Evaporative Cooling System (PV-TE-EC) combinations, i.e. PV-EC (without TE), PV-TE-EC, PV-2TE-EC (two cascaded layers of TE sandwiched between PV and EC) and PV-3TE-EC (three cascaded layers of TE sandwiched between PV and EC as shown in Fig. 4 (a)) systems. The TE module placed adjacent to the lower surface of the PV is fabricated from p-type and n-type bismuth telluride (ZT ~1). Various hybrid systems made of PV and TE assisted or not assisted with EC are studied e.g., PV, PV-TE, PV-EC, PV-TE-EC, PV-2TE-EC, and PV-3TE-EC. These hybrid systems used PV, TE, and EC in parallel arrangements [16].

The individual and overall power output contributions from PV and TE in the hybrid systems with respect to the concentration ratio are summarized in Fig. 4(b). As the concentration ratio is increased, the overall power output of all the hybrid systems got increased. An increase in solar concentration ratio increases the overall temperature of the hybrid systems. In addition, the temperature rise augments the evaporative cooling effect from EC and results into higher equivalent temperature difference across TEs. This reduces the power output from PVs but increases the power output from TEs. This leads to an increase in the overall efficiency of PV-TE-EC, PV-2TE-EC, and PV-3TE-EC in the ascending order. At concentration ratio 7, PV-TE-EC, PV-2TE-EC and PV-3TE-EC produce the output power of 970, 993 and 1014 Wm^{-2} respectively. This corresponds to the efficiency increment of PV-TE-EC, PV-2TE-EC and PV-3TE-EC by 2.15, 4.87 and 6.54% respectively [16].

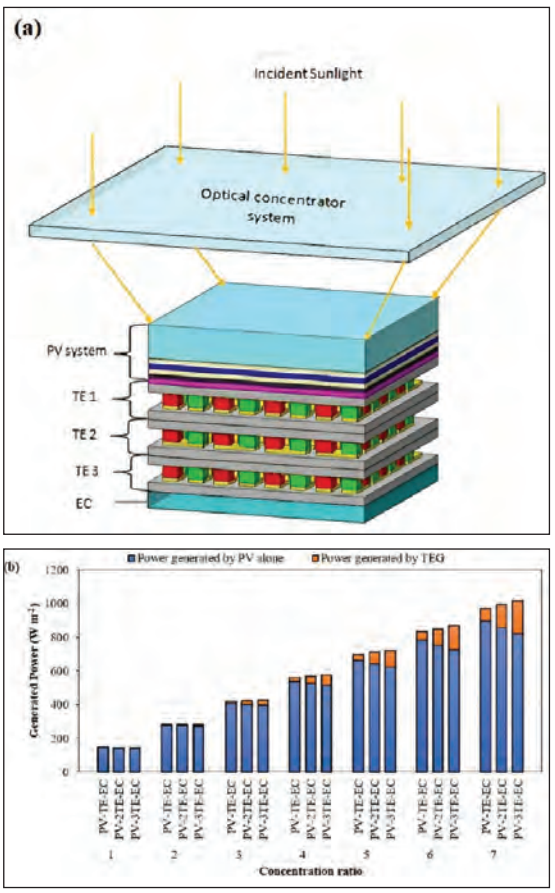

Fig. 4 PV-3TE-EC hybrid system: (a) Schematic representation of the structural diagram, (b) Power output with respect to solar concentration ratios [16].

4. Low Temperature Applications: Solar Thermoelectric Generator (STEG)

STEG can be used to generate electricity from tapped solar energy and therefore they are an attractive renewable energy solution for standalone power conversion. In addition, STEG has been used in power generation for health monitoring system, wireless sensors, space applications and several other low power applications. In this, Solar concentrators are placed over the heat source to conduct the thermal energy to TE and to perform energy conversion analysis of the TE at various solar concentration ratios. The energy conversion efficiency is found to be around 15% and 23 % for TE material with ZT 1 and 2 respectively. A modification to the set-up of STEG is also tried in which the solar energy is concentrated on three layered TE (first layer: Bismuth telluride, second layer: Lead telluride, third layer: Silicon) using metamaterial. Finned heat sink is used to increase the efficiency of conversion of solar energy to electricity to around 24%. However, the consideration over here is that all the energy falling on the metamaterial layer is reaching the TE top surface [17].

6. High Temperature Applications: β-$FeSi_2$ based Thermoelectric

In high temperature applications at 750-800°C, β-$FeSi_2$ based TE is the ecofriendly and suitable material for high temperature application. The β-$FeSi_2$ based TE circuit is constructed as shown in Fig. 3(b)-(e). In this TE circuit, 29 legs of β-$FeSi_2$ TE are used in the TE circuit and the maximum power output obtained is 4.1 mW at 1200 K. Power density per TE leg cross sectional area is determined to be around 0.0284 $mWcm^{-2}$. The contact resistance per leg using silver foil is determined at 1000 K to be around 5.27 X 10^{-6} Ω [7].

7. High Temperature Applications: Multi Segmented Thermoelectric Generator

To increase the overall efficiency of TE generator (TEG), multi-segmented p-type and n-type legs are designed as shown schematically in Fig. 5(a) and described in the chart from Fig. 5(b). Multi-segmented TEGs are designed with different TE materials segmented such that a TEG material with higher Z at high temperature is segmented with a different TEG material with higher Z at low temperature [18]. The thermoelectric properties mentioned in Fig. 5(b) are averaged over the usable temperature range. A transition metal silicide thermoelectric device as shown in Fig. 5(a) is made from TE materials which are having highest ZT value over the desired working temperature range. The p-type segments are represented as P_1, P_2, P_3 and n-type segments as N_1, N_2. The TE characteristics as given in Fig. 5(b) are used to determine the lengths of each of the thermoelectric material in each of the legs [18]. The design has been prepared with the cot junction temperature at 1200 K, cold junction temperature at 500 K, overall Length of leg as 50 mm and cross section area for each leg as 100 mm^2.

The length of each segment in a TE leg is determined using Eq. (2). Here, i denotes the sequence of the segment material and j represents the position of segment material in the leg.

$$\frac{k_{ij}\Delta T_{ij}}{l_{ij}} = \frac{k_{ij+1}\Delta T_{ij+1}}{l_{ij+1}} \quad \ldots (2)$$

Consider a leg with N number of segments, the effective Seebeck coefficient, S´, for the multi-segmented TEG is determined using Eq. (3) and is found to be 149 μVK^{-1}.

$$S'_{pn} = \sum_{i=p,n} \sum_{j=1}^{N} \frac{|S_{ij}|(T_{ij-1} - T_{ij})}{T_H - T_C} \quad \ldots (3)$$

The circuit voltage, V_T is determined using effective Seebeck coefficient as shown in Eq. (4) and is found to be 0.104 V.

$$V_T = S'_{pn}(T_H - T_C) \quad \ldots (4)$$

The effective Seebeck – Thomson coefficient, Sˆ, at hot junction interface is given as Eq. (5) and is determined to be 277 μVK^{-1}:

$$\hat{S} = |S_{p1}| + |S_{n1}| \pm \left|\frac{\Delta S_{p1}}{2}\right| \frac{T_{p1}}{T_H} \pm \left|\frac{\Delta S_{n1}}{2}\right| \frac{T_{n1}}{T_H} \quad \ldots (5)$$

The effective Seebeck – Thomson coefficient, Sˆ, at hot junction interface is given as Eq. (5) and is determined to be 277 μVK^{-1}:

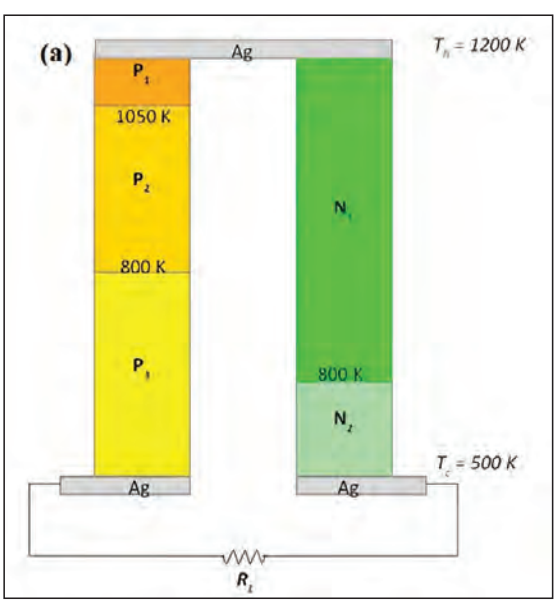

(b)

Sr. No.	TE Leg Type	TE Material	Melting point, K	Crystal Structure	Band Gap, E_g, eV	ZT_{max}	Working temperature range, K	Resistivity, ρ, Ω cm	Thermal Conductivity, k, W/cmK	Seebeck Coefficient, S, V/K
1	p-type	$Cr_{2.5}Mn_{0.5}(Si_{0.8}Al_{0.2})$	1743	Hexagonal, c/a=1.4358	0.7	0.25	500-800	0.0018	0.055	0.000135
2		$MnSi_{1.75}$	1430	Nowotny Ladder	0.60	0.7	800-1050	0.0031	0.054	0.00013
3		$Fe_{0.9}Mn_{0.1}Si$	1400	Orthorhombic	0.52	0.59	1050-1200	0.0017	0.028	0.00016
4	n-type	$Mg_2Si_{0.5}Sn_{0.5}Se_{0.02}$	1270	Cubic	—	0.0	500-800	0.00083	0.011	0.0002
5		$Fe_{0.9}Co_{0.1}Si$	1400	Orthorhombic	0.57	0.41	800-1200	0.00176	0.037	0.000128

Fig. 5 Segmented Transition Metal Silicide based Thermoelectric Device: (a) Schematic diagram of the multi-segmented T, (b) TE characteristics of p-type and n-type transition metal silicides [7,19-21].

8. Conclusions:

- Commercially available PV cell efficiency usually varies between 15 to 20 %. There is around 6.5% rise in overall thermal efficiency of PV-TE-EC (Evaporative Cooling) based hybrid power generator with the operating temperature of around 85°C.
- In high temperature applications at 750-800°C, β-$FeSi_2$ based TE is the ecofriendly and suitable material for high temperature application. The power output is calculated for 29 legs of p-type and n-type β-$FeSi_2$ and the maximum power output and power density are 4.1 mW and 0.0284 mWcm^{-2} respectively.
- Using necessary relations in mathematical modeling a proper combination of eco-friendly transition metal silicides in each multi-segmented TE leg is proposed. For the designed multi-segmented TE leg, to be used in 500 – 1200 K temperature range, the effective Seebeck coefficient, circuit voltage and effective Seebeck – Thomson coefficient are determined to be 149 μVK^{-1}, 0.104 V and 277 μVK^{-1} respectively.
- The maximum power output obtained is around four times what is obtained in an only

β-$FeSi_2$ based TE. The practical feasibility of manufacturing such composite TE legs need to be checked.

- Thermoelectric material is a need of future as it provides a means for harvesting waste heat energy and is also the clean form of energy. Many techniques have been employed for synthesis of TE, a potential candidate for scavenging energy but for many of the varieties of TEs, there is no such specific route which can lead us to the synthesis of this material on an industry level.
- A unicouple or TE Generator or TE Cooler needs to be formed of p-type and n-type thermoelectric material to achieve higher value of Figure of merit, Z.
- Some TE materials contain toxic elements or less abundance elements which narrow down their scope of application. An ideal TE material should be a phonon glass and an electron crystal, which means that the materials should have a low lattice thermal conductivity just like glass, and a high electrical conductivity just like in a crystal and at the same time should be environmentally friendly.
- Many types of TE have attracted the attention in the last years because of their technological potential in the field of optoelectronics, light emitting diodes (LEDs), medical, aerospace and defense applications due to the thermoelectric conversion properties, chemical stability, non-toxicity and relatively low cost of production. There is a huge scope to do research in the choice of the element and its quantity that need to be added to get high ZT thermoelectric material.

9. References:

1. Hilaal Alam, Seeram Ramakrishna, "A review on the enhancement of figure of merit from bulk to nano-thermoelectric materials", Nano Energy Vol. 2, 2013, pp: 190-212.
2. Johansson, M. T., Söderström, M., " Electricity generation from low-temperature industrial excess heat—an opportunity for the steel industry", Energy Efficiency, 7(2), 2013, 203–215. doi:10.1007/s12053-013-9218-6.
3. Zabek, D., & Morini, F., "Solid State Generators and Energy Harvesters for Waste Heat Recovery and Thermal Energy Harvesting", Thermal Science and Engineering Progress. 2018, doi:10.1016/j.tsep.2018.11.011.
4. Rull-Bravo, M., Moure, A., Fernández, J. F., & Martín-González, M., "Skutterudites as thermoelectric materials: revisited," RSC Advances, 5(52), 2015, 41653–41667. doi:10.1039/c5ra03942.
5. Terry Tritt, "Thermoelectric Materials, Phenomena, and Applications: A Bird's Eye View," Annual Review of Materials Research, Vol. 41, 2011, pp: 433-448.
6. Mikhail Fedorov, "Thermoelectric silicides: Past, Present and Future," Journal of Thermoelectricity, Vol. 2, 2009, pp: 51-60.
7. V. S. Poddar, N. B. Dhokey, "Evaluation of Thermoelectric Properties of Doped β-Iron Disilicide Prepared by the Powder Metallurgy Technique", Transactions of the Indian Institute of Metals, 2021, 74, pp: 399-410.
8. Cain, T. A., Kajdos, A. P., & Stemmer, S., "La-doped SrTiO3 films with large cryogenic thermoelectric power factors", Applied Physics Letters, 102(18), 2013, 182101. doi:10.1063/1.4804182
9. Ian T. Witting, Thomas C. Chasapis, Francesco Ricci, Matthew Peters, Nicholas A. Heinz, Geoffroy Hautier, G. Jeffrey Snyder, "The Thermoelectric Properties of Bismuth Telluride", Advanced Electronic Materials – Progress Report, 2019, 1800904 pp:1-20, https://doi.org/10.1002/aelm.201800904

10. Balout, H., Boulet, P., & Record, M.-C., "Thermoelectric Properties of Mg2Si Thin Films by Computational Approaches", The Journal of Physical Chemistry C, 118(34), 2014, 19635–19645. doi:10.1021/jp506323r

11. Liu, Y., Xu, L., Zhao, C., Shao, M., & Hu, B., "Tuning the Seebeck effect in C60-based hybrid thermoelectric devices through temperature-dependent surface polarization and thermally-modulated interface dipoles", Physical Chemistry Chemical Physics, 19(22), 2017, 14793–14800. doi:10.1039/c7cp01736g

12. Klochko, N. P., Klepikova, K. S., Zhadan, D. O., Petrushenko, S. I., Kopach, V. R., Khrypunov, G. S., Khrypunova, A. L., "Structure, optical, electrical and thermoelectric properties of solution-processed Li-doped NiO films grown by SILAR", Materials Science in Semiconductor Processing, 83, 2018, 42–49. doi:10.1016/j.mssp.2018.04.010

13. V. S. Poddar, N. B. Dhokey, "Thermoelectric Properties of Iron Disilicide and Manganese Silicide: Synthesis and Characterization", Transactions of the Indian Institute of Metals, 2019, 72 (10), pp:2711–2719, doi: 10.1007/s12666-019-01743-8.

14. Papageorgiou, C., Hatzikraniotis, E., Lioutas, C. B., Frangis, N., Valassiades, O., Paraskevopoulos, K. M., & Kyratsi, T., "Thermoelectric Properties of Nanocrystalline PbTe Synthesized by Mechanical Alloying",. Journal of Electronic Materials, 39(9), 2010, 1665–1668. doi:10.1007/s11664-010-1234-0

15. Liu, W., Hu, J., Zhang, S., Deng, M., Han, C.-G., & Liu, Y. (2017). New trends, strategies, and opportunities in thermoelectric materials: A perspective. Materials Today Physics, 1, 50–60. doi:10.1016/j.mtphys.2017.06.001.

16. V. S. Poddar, V. A. Ranawade, N. B. Dhokey, Study of Synergy between Photovoltaic, Thermoelectric and Direct Evaporative Cooling System for Improved Performance, Renewable Energy, January 2022, 182, Pages 817-826, DOI:10.1016/j.renene.2021.10.040.

17. Guiqiang Li , Samson Shittu, Xiaoli Ma, Xudong Zhao, "Comparative analysis of thermoelectric legs optimum geometry between photovoltaic-thermoelectric and solar thermoelectric", Energy, Vol. 171, 15 March 2019, Pages 599-610.

18. Kanimba, E., Pearson, M., Sharp, J., Stokes, D., Priya, S., & Tian, Z. (2017). A modeling comparison between a two-stage and three-stage cascaded thermoelectric generator. Journal of Power Sources, 365, 266–272. DOI: 10.1016/j.jpowsour.2017.08.09.

19. Macario, L. R., Cheng, X., Ramirez, D., Mori, T., & Kleinke, H., "*Thermoelectric Properties of Bi-Doped Magnesium Silicide Stannides*", ACS Applied Materials & Interfaces, 2018. DOI:10.1021/acsami.8b15111.

20. Fedorov, M. I., Isachenko, G. N., "*Silicides: Materials for Thermoelectric Energy Conversion*", Japanese Journal of Applied Physics, 2015, 54(7S2), 07JA05. DOI:10.7567/jjap.54.07ja05.

21. Zhang, L., Tosho, T., Okinaka, N., & Akiyama, T. "*Design of Cascaded Oxide Thermoelectric Generator*", MATERIALS TRANSACTIONS, 2008, 49(7), 1675–1680. DOI:10.2320/matertrans.mra2008085.

ANALYSIS OF SPIN NUMBER VARIATIONS IN A SPIRAL AIR JET MILL USING SINGLE PHASE CFD SIMULATIONS

Kunal K. Sharma[a*], Devang V. Khakhar[a]

[a]Department of Chemical Engineering, Indian Institute of Technology Bombay, Powai, Mumbai, India.

Abstract: *Grinding large quantities of particulate materials is an important operation in many industries. The focus of the present work is the analysis and optimization of an air jet mill, which is a versatile equipment used in many industries for fine grinding powders to sizes less than around 10 microns. The efficiency of the grinding process in an air jet mill typically varies from 2% to 4%, depending on the design and operating parameters so even small improvements in efficiency can result in significant energy savings. Amongst many of the available machines, spiral air jet mills are attracting the attention because of their advantages like absence of the moving parts and low temperature rise during grinding, resulting in better temperature control with low maintenance. We study the gas flow in the mill using Computational Fluid Dynamics (CFD) using open FOAM and actual machine behaviour by means of experiments. The spin number is the ratio of tangential velocity to the radial velocity of the flow. A particle inside the jet mill experiences the drag towards the outlet in the radially inward direction and a centrifugal force in the radially outward direction. A balance of the two forces defines the cut size of the particle at which both the forces are equal and opposite in direction. As per the resultant equation,the cut size is inversely proportional to the spin number squared, assuming other variables to be constant. Thus, as the system is dilute with respect to the particles, getting the flow behaviour of single phase helps to predict the cut size variation. Simulations were carried out for variable gas flow rate (Q), classifier height (ht), classifier radius (rt), rotation (RPM) of the peripheral surface, the chamber sizes (R), the chamber heights (H) of the machine, fluid kinematic viscosity and the machine scale-up. Only one parameter varied at a time keeping others unchanged from a base case, for univariate analyses. We have found that the spin number decreases with rise in input gas flow rate (Q) and with falling peripheral surface rotation (RPM), increases with higher chamber radial size and lower classifier radius, and spin number is not affected significantly by chamber height and classifier height. As per the simulations, the machine spin number drops more steeply for higher fluid viscosities. On the experimental front, the runs with different chamber sizes were carried out and it was found that larger diameter chambers yield smaller product particles, the findings of which are in the accordance with simulation results (higher spin number yielding smaller product cut sizes).*

Keywords: *Grinding;10-micron size powder product; single phase CFD; univariate analyses.*

1. Introduction:

Spiral Air Jet Mills are widely used in various industries, including pharmaceuticals, chemicals, food, and cosmetics, due to their ability to produce fine powders with consistent particle size and narrow particle size distribution. These mills use compressed air to generate a high-speed jet stream, which is directed into the grinding chamber. The air stream, along with the grinding material, is drawn into the centre of the chamber by a spiral, where the material is subjected to high-speed collisions and grinding forces. The resulting fine powder is then separated from the coarser particles through the use of a classifier. One of the key advantages of Spiral Air Jet Mills is their ability to produce fine powders with consistent particle size and narrow particle size distribution typically less than 10 microns. This is achieved through precise control over the grinding process and the use of an efficient classifier. Additionally, Spiral Air Jet Mills are known for their energy efficiency, as they use a relatively low amount of energy to produce fine powders. This makes them an attractive option

for companies looking to reduce their energy consumption and lower their carbon footprint. The Spiral Air Jet Mill is known for its energy efficiency, gentle grinding process, and ability to produce ultra-fine high-quality powders with narrow particle size distributions. But, since their creation in the 1930s, the mills have remained practically unmodified [1].

Size reduction happens predominantly towards the outer walls as a result of particle–wall and particle–particle collisions. The size reduction intensity is determined by the impact velocity or throughput. The categorization process is influenced by particle size. A particle is subjected to two dominant forces during classification: inertia centrifugal force and fluid drag force. The radial flow of gas towards the exit at the mill centre creates the drag force. The vortex's centrifugal forceshold the coarse particles in the crushing chamber [2].

The centrifugal and radial drag forces acting on the vortex particles are proportional to their size (x). As size reduces owing to fracture, centrifugal force (proportional to x3) declines faster than radial drag (proportional to x2) forces. The particle will leave the mill if the drag force exceeds the centrifugal force; otherwise, it will remain in the mill and be subjected to more impact loadings until it breaks; otherwise, the particles will be broken down further until they are small enough to escape the mill. [2,3].

Finer particles have a stronger tendency to escape as the ratio of drag force to centrifugal force (the inverse of the spin number squared) improves with particle size. As a consequence, the air jet mill simultaneously breaks and classifies the particles. Despite the fact that spiral jet mills consume a lot of energy, they offer a few benefits. The mill has many perks over other mills, such as the ability to create particles smaller than 10 micrometres with a narrow particle size distribution, low temperature rises due to high gas flow rates, high reliability due to the mill's lack of mechanical working components, applicability for particles with a wide range of material hardness, and low contamination due to autogenous action. Moreover, when compared to other mills, such as ball mills, which have energy efficiency ranging from 0.1 to 1%, jet mills have a fairly high energy efficiency of 2-5 percent of the provided energy consumed to build new surfaces [4, 5, 6, 7].

To achieve an aim of any project normally three approaches are encountered viz. theoretical, experimental and computational. Of the three approaches, computational method is relatively cost-effective, quick, and user-friendly. It is utilized in fields like engineering and science to model physical phenomena through a set of equations referred to as governing equations. Advancements in computer performance have greatly impacted computational methods, with one example being Computational Fluid Dynamics (CFD). CFD has gained popularity among researchers due to its efficiency, leading to developments in numerical methods for fluid flow. While commercial CFD codes are available for purchase, the difficulty in modifying them and limitations in computing nodes due to licensing have led to the creation of open-source CFD codes, such as Open FOAM. This open-source code, written in C++, allows users to upgrade and further develop the code. Its systematic structure, ease of use, and reliability have drawn researchers' attention.

This study proposes a single-phase numerical simulation of spiral air jet mill using the Open FOAM V7.0 open-source CFD tool, incorporating the standard k-ε turbulence model. The goal

is to simulate the machine to qualitatively predict the cut size variation. Plus, single phase simulations shall be able to dictate the behaviour of the machine for dilute 2 phase systems. This work will be particularly relevant to researchers working on simulations of turbulent jets concerning jet mill single phase dynamics.

1.1 Expression for the cut size equation:

The particle size at which the drag and centrifugal forces balance is referred to as thecut size dcut. Assuming the tangential particle velocity matches the tangential air velocity, aforce balancing ($F_d = F_c$) yield:

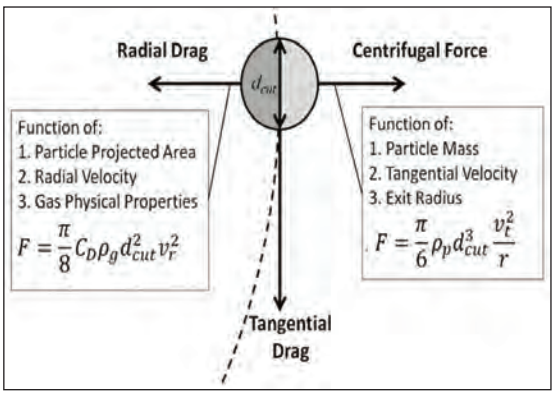

Fig. 1. Force balance across the particle. [2]

$$\frac{\pi}{8} C_D \rho_A {v_r}^2 {d_{cut}}^2 = \frac{\pi}{6} \rho_p {d_{cut}}^3 \frac{{v_t}^2}{r} \qquad (1)$$

Where; ρ_A is the air density, ρ_p is the particle density, CD is the drag coefficient,Vr is the radial air velocity, Vt is the tangential air velocity and r is the radial position of the particle. Further,

$$d_{cut} = B \frac{{v_r}^2}{{v_t}^2} \qquad (2)$$

Where, B includes all the remaining terms of the equation. Hence, the cut size is proportional to the inversely squared spin number (Vt/Vr).

Nomenclature

Q	gas flow rate
LPM	litres per minute
rt	classifier tube radius
ht	classifier height
R	chamber radius
H	chamber height
RPM	rotation per minute
x	particle size
K, k	turbulent kinetic energy
ε	turbulent kinetic energy dissipation (epsilon)
RANS	Reynolds Averaged Navier Stokes equations
CFD	Computational Fluid Dynamics
U	mean velocity (vector)
d_{cut}	particle cut diameter
F_d	Drag force
F_c	Centrifugal force
ρ_A	air density
ρ_p	particle density
CD	drag coefficient
r	radial position of the particle
B	proportionality constant in cut size equation
fw	fixed wall
sd1	cyclic side 1
sd2	cyclic side 2
u	net velocity
v	effective kinematic viscosity
∇ • (v ∇ u)	viscous stress term
Vt/Vr	spin number
V	machine volume

2. Computational Methodology

2.1 Problem information and software details:

The problem investigated in the present work is the numerical study carried out on single phase flow of air in the spiral air jet mill using k-ε turbulence model from Reynolds-averaged Navier Stokes (RANS) family. The validation of the turbulence model with the experimental data (for the various radial size variation of chambers only) will be discussed with the help of computed results.The simulation jobs were carried out using CFD code open FOAM version 7.

2.2 Assumptions

The conventional jet mill is simplified for simulations, neglecting the jet effects, wherein instead of jet inlets, whole chamber peripheral surface area is considered as an inlet and the same is provided with the radial and tangential components of velocity of the fluid. The fluid is turbulent in nature, but we are concerned with the overall variation of the spin number with radial distance, hence, wall boundary layer effects are not in focus. Similarly, RANS is used to capture overall profile and so the smaller length scalecalculations are neglected. Also, the fluid is assumed to be incompressible and Newtonian in nature. A sector of jet mill is considered in simulations, hence, the zone extending the classifier tube till the top wall of the chamber is of no interest.

2.3 Computational Domain

The physical scenario considered in the study is the simplified geometry of jet mill. To account for the flow patterns inside the mill, the outer chamber peripheral wall (radius, R and height H) of the jet mill is acting as an input to the system rotating with certain RPM (tangential velocity component, Vt) with the radial component (normal velocity component, Vr) directing towards the centre of the chamber. The outlet surface is placed at the classifier height (ht). The chamber upper face, chamber lower face and the curved surface area of cylindrical classifier are walls. The computational domain is as shown.

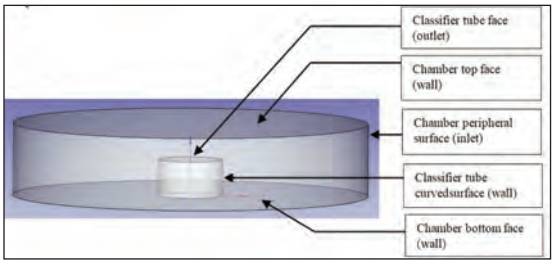

Fig. 2. Schematic of Computational geometry.

2.4 Computational Grid:

The computational domain and the grid are generated in GMSH, an open-source meshing software. The domain as shown above is developed by defining points, lines, rotation (if needed) then surfaces, defining transfinite curves with mesh points progression and bumps, recombining the surfaces for structured meshing throughout the surface, then applying the rotational extrusion to the surface and then tagging the regions like inlet, outlet, fixed wall (fw) and cyclic side1(sd1), cyclic side 2(sd2) and volume are defined. as a script file for GMSH. To lower down the computational time, a 3D sector (15deg.) of jet mill is considered, with cyclic boundary conditions on flat faced sides. Additionally, the meshing near the walls is made finer compared to the central part of the sector to further optimise the computational cost with reasonable accuracyresolving the fluid flow physics properly. The mesh is made finer in the zones of higher velocity gradients.

It is ensured that the surface area and the location of grid-points on both the cyclic surfaces are identical to avoid inaccuracies. The mesh is then imported in open FOAM using gmsh To Foam command, and the pressure-velocity boundary conditions for the respective boundaries are updated as needed.

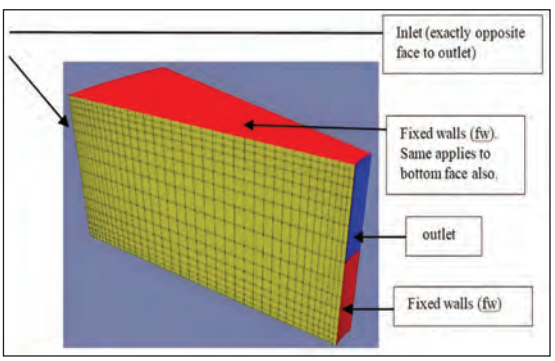

Fig. 3. Computational domain with grid-points and boundary conditions

2.5 Governing Equations:

The governing equations in this scenario represent the Reynolds averaged continuity and momentum equations for incompressible and turbulent flow assumptions, they are as shown:

$$\nabla \cdot u = 0 \qquad (3)$$

$$\frac{\partial u}{\partial t} + \nabla \cdot (uu) - \nabla \cdot (\nu \nabla u) = -\nabla p \qquad (4)$$

Where, p is kinematic pressure, u is the velocity, v is the effective kinematic viscosity, and it is taken care by the k-epsilon turbulence model for the present work. The term "∇ • (v ∇ u)" is the viscous stress term.

2.6 Numerical Schemes, Solutions and Boundary conditions:

The unsteady part is discretised by Euler scheme, gradients by Gauss linear, the divergence are discretised by Gauss limited linear V for velocity and rest are set to Gauss limited linear. On the solution fronts, the tolerances are set to 1e-6as residuals. The boundary conditions for walls are 'no Slip' and for flat faces side1 (sd1) and side 2 (sd2) its 'cyclic' with both the patches coupled together with 'neighbour Patch'. Pressure at inlet and walls is 'zeroGradient' and at outlet, it is set to atmospheric conditions. Similarly, velocity at inlet is 'cylindrical Inlet Velocity' with both radial and tangential components defined, while at the outlet it is set to 'zerogradient'. Both Pressure and Velocity are set to 'cyclic' for sd1 and sd2 patches.

The solution for the governing equations is obtained by iterative method through PISO algorithm. This algorithm is available in open FOAM by default and can be applied using the keyword 'pisoFoam'. The ready computational grid is subjected to the grid independence study, to ensure grid independent results. The grid independence study was carried out with multiple meshesand the independence is achieved for a grid with number of cells 1.39 million for 360 deg which reduces to around 5400 cells for 15 deg. sector of cylindrical chamber. The grid independence study is discussed later.

3. Results and discussions

The simulation data is exported using Paraview and then fed to an in-house C program code that is developed to bin the geometry in the radial coordinates and obtain the average spin number for a bin. The data points of the bins are then connected to yield a curve using xmgrace. In general, a convention is followed wherein the spin number (Vt/Vr) Vs. the fractional radial distance from the mill centre are plotted and the concerned parameter is analysed. The schematic of velocity streamlines are as shown:

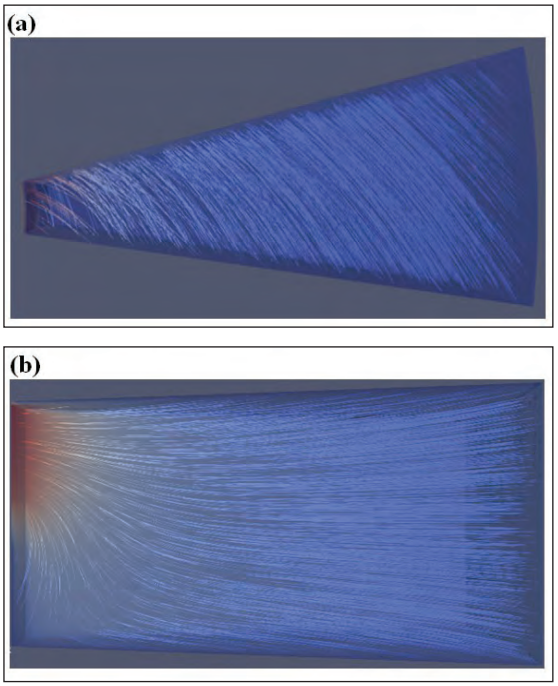

Fig. 4. Velocity streamlinesfrom inlet (right) to outlet (left). (a) top view and (b) front view.

The gas is entering from the right peripheral surface and exiting the domain from the upper half of left periphery which is outlet. In the top view, it is visible that the velocity streamlines are flatter (higher radius of curvature) near the left upper half than the left lower half which highlights the gas exit. In the front view, it can be seen that the streamlines are eventually getting concentrated at the outlet yielding longer streamlines and so higher radial velocity magnitudes.

3.1 The Grid Independence

The GMSH software is used for meshing, where in the number of points per unit length (nl) of side 1 (sd1) is used as a basis for the entire mesh. Additional effects like bump and progression are used to control the mesh regions as per the requirements. The increase in "nl" makes the entire mesh finer.

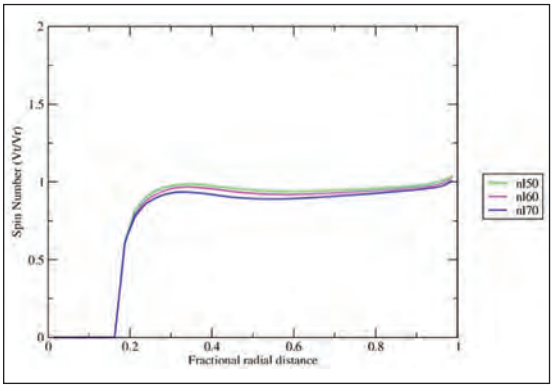

Fig. 5 Grid Independence

The nl is varied from a lower value of 50, which represents the coarser mesh, to 60 and 70, which represents the finer meshand they are taking almost the same values, hence a minimum of nl = 50 is taken, balancing the accuracy and the computational cost, and it is ensured that the mesh density is always higher than nl = 50, wherein the structural mill parameters are to be analysed. In all the graphs, the curves begin from right side (the chamber radius, R) as inlet and gas leaves the mill at outlet from the left side (where the spin number becomes 0). In between, the curve represents the spin number variation across the radial distance in the mill from inlet to outlet.

3.2 The effect of K and epsilon on the mill geometry

The initialisation of Turbulent kinetic energy and the turbulent kinetic energy dissipation rate impact the flow pattern of the fluid in turbulence; hence these have been changed for the mill to take into account such effects. While considering the incompressible fluid with turbulence, the K values are supposed to be smaller and the effect

of the same has been analysed for the variation keeping epsilon constant and thereby vice-versa is done for epsilon, keeping k constant.

Table 1: Deciding k-epsilon parameters with variation in both on case-by-case basis.

	K	epsilon
Case0	0.00000005	0.00000005
Case1	0.005	0.005
Case2	0.5	0.5
Case3	5	5
Case4	50	50
Case5	500	500
Case6	5000	5000

The values of k are varied from 0.1 to 20 for an epsilon of 500, and thereby it can be seen that there is no substantial change in the profile. Similarly, in the case of epsilon from 300 to 50000 for k of 0.1, all the curves are overlapping each other. There has been a significant change in trend in the third graph, wherein the turbulent kinetic energy and its dissipation rate are increasing, as shown in the table 1.

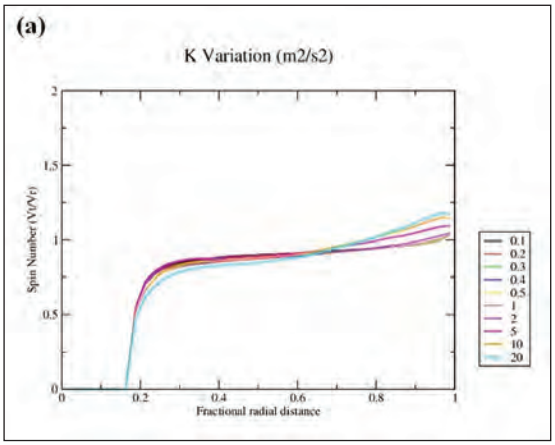

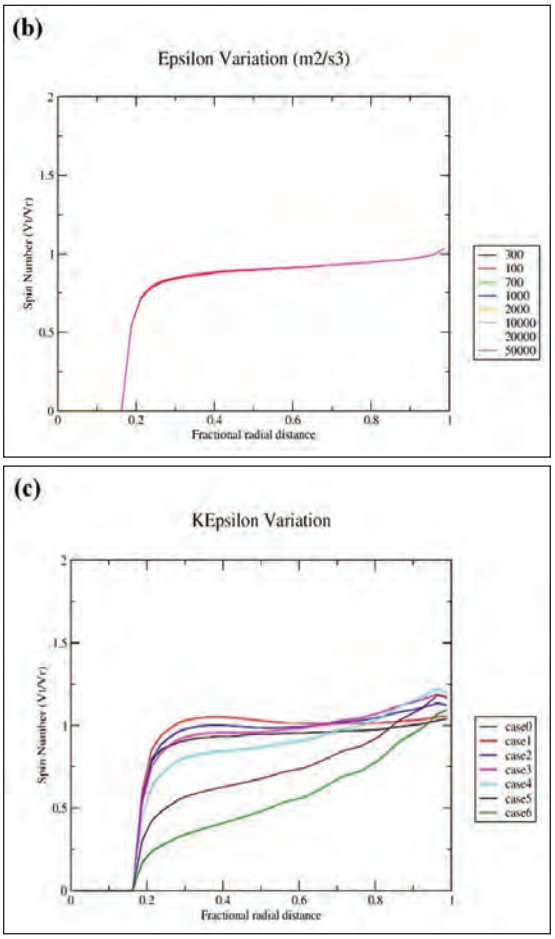

Fig. 6. K-epsilon variation in a single-phasejet mill. (a) K variation with constant epsilon. (b) Epsilon variation constant K. (c) Variation of K and epsilon both.

With increasing k-epsilon values in Figure 6(c), the curves become steeper and steeper, for the same simulation time of the mill. Essentially, the nature of the curves are primarily dependent on the k and epsilon values given at the inlet boundary condition, otherwise the curves would have overlapped as the k-epsilon effect would have been washed out while reaching steady state. In the subsequent studies, the K is 0.1 m^2/s^2 and the epsilon is 500 m^2/s^3.

3.3 Parametric variations:

To begin with, a base case is established, learning from grid independence, the k-epsilon studies, the experimental design, and the operating range of the machine. The base case is as follows:

Table 2: Base case parameters

Parameter	Value
Chamber Radius (R)	5cm
Chamber Height (H)	2cm
Classifier Radius (rt)	0.9cm
Classifier Height (ht)	1cm
Initialised Radial Velocity	0.75m/s
Initialised RPM	150
Initialised K	0.1 m^2/s^2
Initialised epsilon	500m^2/s^3

The overall volumetric flow rate varies from 300 LPM to 750 LPM, which is the normal operating flow rate of jet mills with such dimensions. The parametric effects of chamber height, chamber size, classifier height, classifier size, flow rate, RPM, and the scale-up have been studied.

3.3.1. Effect of Chamber radius and Chamber Height

The chamber cylindrical radius is varied as 2 cm, 3 cm, 4 cm, and 5 cm in order to plot the fractional radius. Higher chamber radii may be taken, and accordingly, the comparison should be normalized with respect to the biggest radius considered. Similarly, the chamber height is varied as 1.5 cm, 1.75 cm, 2 cm, 2.25 cm, 2.5 cm, and 3 cm, keeping in mind that the chamber height (H) should always be greater than the classifier height (ht) to allow gas to exit from the machine.

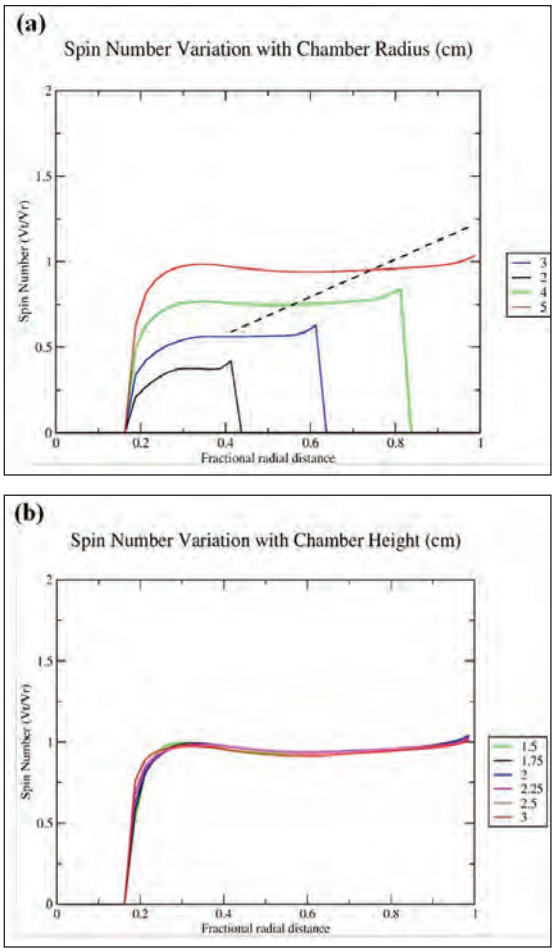

Fig. 7. Spin Number variation with (a) chamber radius and (b) chamber height.

High chamber radii result in a higher spin number at the inlet, and the spin number is almost always maintained at a constant value of 1 (for the red curve) over the majority of the fractional radial distance, except for the exit effects. With larger chambers (R), the range (R-rt) increases for the same classifier (r), resulting in more length at which the spin number can

remain at higher values; this is advantageous, so chambers with a higher radius are preferable. Changing the chamber height shows no variation in spin number as all the curves are almost overlapping. The locus of the maximum spin number is connected through a dotted line (R^2=0.9998) a shown with the equation:

$$\frac{Vt}{Vr} = 1.082 \times (fractional\ radial\ distance) - 0.0331 \quad (5)$$

The fact has been experimentally verified, wherein semi batch runs with chamber radii of 4 cm, 5 cm, and 6 cm were executed, and the mean particle sizes were around 15 microns, 6 microns, and 2 microns, respectively. A higher spin number results in a product with a smaller cut diameter.

3.3.2. Effect of Classifier Radius and Classifier Height:

The classifier radius is changed to 0.9 cm, 1.35 cm, 1.8 cm, 2.25 cm, 2.7 cm, and 3.6 cm, such that all the values stay lower than the chamber radius. Following the similarity, the classifier height is changed from 0 to 15mm with an interval of 2.5mm, all values lower than the chamber height of 20mm.

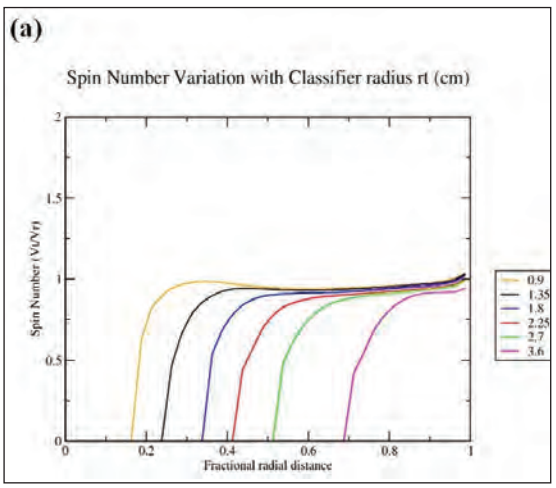

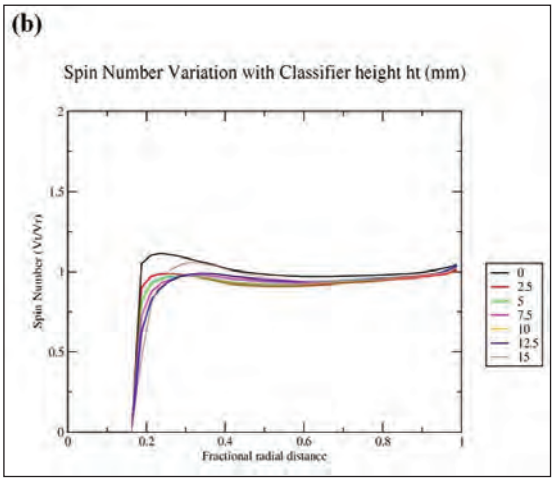

Fig.8 . Spin Number variation with (a) classifier radius and (b) classifier height.

Interestingly, the bigger classifiers tank the spin number more than the smaller ones. This is disadvantageous as the R-rt distance is reduced; hence, smaller classifier radii are preferable. Also, the simulated flow shows that there has been a negligible effect of the variation of the classifier height on the spin number, and the overlapping of the curves just formed a zone enclosing all the spin numbers.

3.3.3 Effect of Flow Rate Q (LPM) and RPM of Peripheral Surface:

The gas inlet flow rate values should be varied according to the normal operating conditions. The flowrate here highlights the amount of gas fed to the machine from the inlet with a direction normal to the peripheral surface, and hence it will directly contribute to the radial velocity; the same is evident in the curves. As the gas flow rate increases, the spin number decreases.

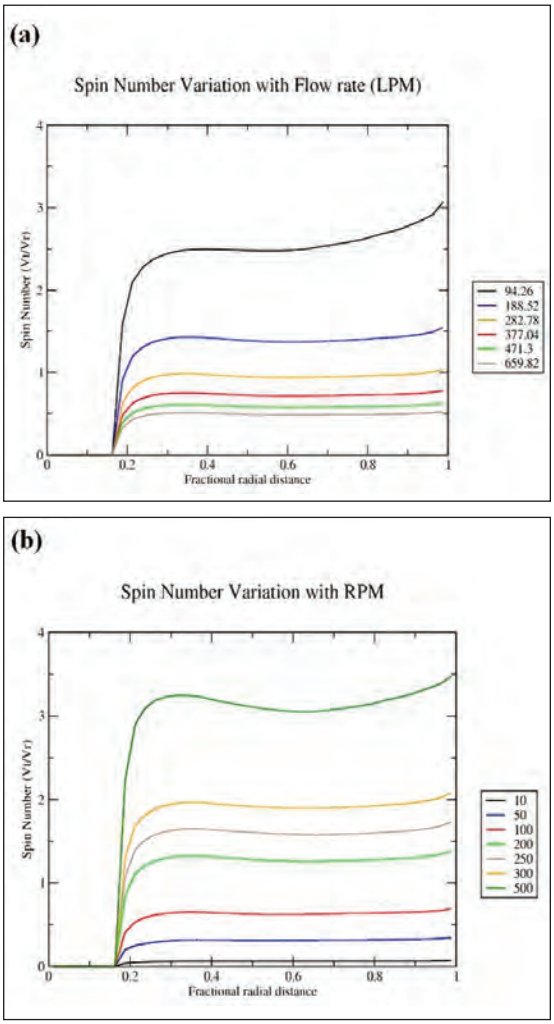

Fig.9. Spin Number variation with (a) gas flow rate and (b) RPM of peripheral surface.

The increase in RPM of the peripheral surface is directly leading to higher tangential velocities. More RPM results in larger spin numbers. One key thing to note is that, the curves are more straight at lower RPMs. This is due to the fact that the radial component is initially at its minimum as the gas moves from the inlet to the outlet and the flow area decreases, resulting in increasing radial velocity, whereas as the gas approaches the exit, the tangential velocity only reaches the 2nd maxima (1st being at the entry point), and then both the radial and tangential velocities become 0, and the entire velocity is in the z direction, representing that the gas is out of the system. More RPM means higher 1st maxima relative to the 2nd maxima and the delta between them hence increases. The spin number may have gone undefined in this region, but the precautions for the same are taken care of while post-processing the data using the C program.

3.3.4. Scale-up:

The structural parameters have been enlarged in all directions, keeping the operating parameters like RPM constant. The Q values have been modified such that the same radial velocity is supplied in all the cases. In all the x, y, and z directions, if all the lengths (l) are increased by the factor, say, "w," giving the final length as 'w*l', then the corresponding volume will be "w3*V," where "V" is the volume equivalent for the length (l).

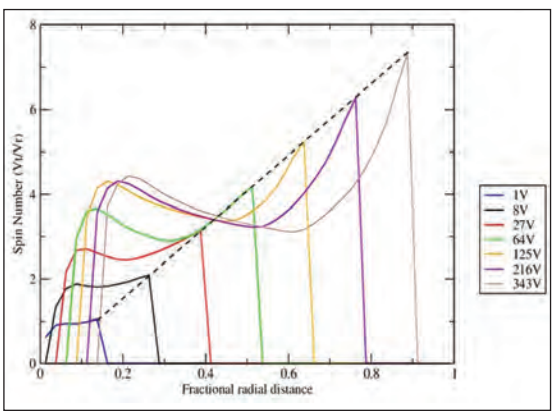

Fig.10. Spin Number variation with machine Scale-up.

The dimensions of the machine are increased linearly, the volume is thus increased by the power 3, and the corresponding spin number for the scaled-up systems is plotted as shown.

While plotting the curves, the radial distance of the biggest machine is taken as the basis for the calculation of fractional radial distance. The maximum and average spin numbers and the range (R-rt) increase with scaling up. As the volume increases in comparison to smaller machine sizes, there is a distinct minimum between the two maxima.The locus of the maximum spin number is connected by the dotted line (R^2=1), the corresponding equation is as follows:

$$\frac{Vt}{Vr} = 8.3725 \times (fractional\ radial\ distance) - 0.1047 \qquad (6)$$

3.3.4. Effect of Fluid Kinematic Viscosity:

The effect of fluid kinematic viscosity has been prominent in this study. As evident, from the curves as the viscosity is increased from the base case configuration of 1.6e-5 to 100e-5 m^2/s and the simulations were run for 1sec of the process time, it can be observed thatthe curves at higher kinematic viscosities possess higher average slope. The reason being, that the effect of tangential component of spin number is damped, more in the fluid with higher viscosity while reaching towards the centre compared to less viscous fluid.

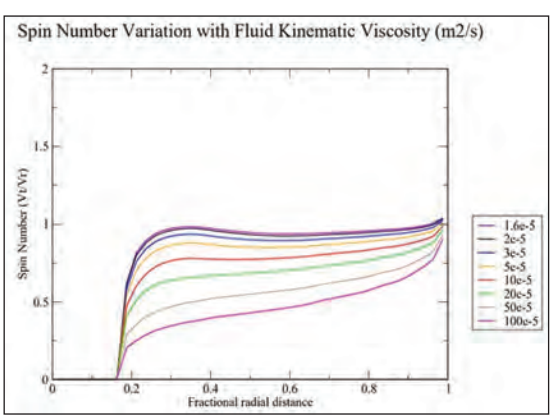

Fig. 11. Spin Number variation with Fluid Kinematic Viscosity.

4. Conclusions:

As the cut diameter of the product from the jet mill is dependent on the spin number, the distribution of spin number across the geometry is crucial to be known. In reality, the two-phase flow of particles and the fluid is dilute and essentially fluid impact on particles is the major contributor (1 way coupling). The single-phase simulations of air in the mill are carried out on the basis of structural and operational parameters and their effects on the spin number are examined. The results are valid considering that the particles in the mill are way too small to deviate from the gas flow. The flowrate is kept within the range of actual mill operation. The following are the inferences from the study.

1. Higher chamber radii are favoured for the higher spin numbers and they are maintained over longer ranges (R-rt), the same is experimentally verified. The chamber height poses no variation on spin number.
2. Smaller classifier tube radiuses are favoured for bigger ranges (R-rt) while the maxima of the spin number stay constant. Spin number can be considered independent of classifier height.
3. For higher spin number (Vt/Vr) more tangential velocity and less radial velocity components are beneficial. So, in similar lines higher peripheral surface RPM and lower radial flow rate (Q) favour higher spin number.
4. Higher fluid kinematic viscosities will lead to more rapid drop of spin number towards the center while identical maxima at the periphery.
5. Extending the current study for scale-up on the basis of spin number alone, leads to the fact that bigger machines favour higher spin

numbers and over longer ranges, the locus of the maximum spin numbers follow a linearity.

6. The linearity relation for the locus of maximum spin numbers for the cases of variable chamber radii and machine scale-up are obtained.
7. The combo of OpenFOAM and the in-house C code for writing utilities to post-process the data was found advantageous.

Acknowledgements

The author is thankful for the kind guidance of Prof. Devang V. Khakhar (Indian Institute of Technology Bombay, Powai, Mumbai 400076, India), Prof. Jyeshtharaj B. Joshi (Institute of Chemical Technology, Mumbai 400019, India) (Homi Bhabha National Institute, Mumbai 400094, India) and other lab users for having fruitful discussions with them. The author acknowledges the use of the computer system infrastructure provided by the Fluid Mechanics Lab, Department of Chemical Engineering, Indian Institute of Technology Bombay, Mumbai.

References:

1. Andrews, N. Method and Apparatus for Providing Material in Finely Divided Form. U.S. Patent US002032827, 3 March 1936.
2. Rodnianski, V., Krakauer, N., Darwesh, K., Levy, A., Kalman, H., Peyron, I., Ricard, F., Aerodynamic classification in a spiral jet mill. Powder Technol. 243, (2013). 110–119.
3. Satyajeet Bhonsale, Lewis Scott, Mojtaba Ghadiri and Jan Van Impe, Numerical Simulation of Particle Dynamics in a Spiral Jet Mill via Coupled CFD-DEM. MDPIpharmaceutics. 13, (2021) 937.
4. Midoux, N., Hošek, P., Pailleres, L., Authelin, J., Micronization of pharmaceutical substances in a spiral jet mill. Powder Technol. 104, (1999) 113–120.
5. Chamayou, A., Dodds, J.A., Air jet milling. Handbook Powder Technol. 12, (2007) 421- 435.
6. Muller, F., Polke, R., Schadel, G., Spiral jet mills: hold up and scale up. Int. J. Miner. Process. 44, (1996) 315–326.
7. Mahesh M. Dhakate, Jyeshtharaj B. Joshi, D.V. Khakhar, Analysis of grinding in a spiral jet mill. Part 1: Batch grinding, Chemical Engineering Science. 231, (2021) 116310- 116321.

AN ENVIRONMENT-FRIENDLY $Na_{0.4}K_{0.1}Bi_{0.5}TiO_3$ CERAMIC FOR ONE-TO-ONE REPLACEMENTOF PZT-BASED CERAMICS IN MULTIPLE APPLICATIONS

Pravin Varade[1,*], Soorya S.[1], N. Shara Sowmya[1], N. Venkataramani[1], Ajit R. Kulkarni[1]

[1]Department of Metallurgical Engineering and Materials Science, Indian Institute of Technology-Bombay, Mumbai, India.

Abstract: *The availability of advanced materials has enabledthe development of new gadgets for household appliances, automobiles, and strategic/smart devices. In the race for such developments intertwined with commercial gains, toxicity of the component elements and resultant materials became secondary. One such successful example is the advent of Pb-based piezoelectric materials with its inherent toxicity effect on humans and the environment. In the functionality of inter-converting mechanical and electrical energy, commercially established piezoelectric materials like PZT address a wide range of applications, such as actuators, sensors, and transducer devices. Significant efforts have been directed in recent times towards eliminating lead from piezoelectric ceramics. However, to date, the best lead-free piezo ceramics synthesized in the research laboratories have not yielded compositions with useful piezoelectric properties so that they may readily replace the well-established commercial compositions of PZT. Thus, the problem of Pb pollution during fabrication, use and burial lingers on. In the present work, our efforts are focused on developing Pb-free piezoelectric material with properties matching closely with that of PZT and identifying the figure of merit for non-resonant applications similar to that of a PZT composition, for a direct and easy replacement of lead-based elements in existing devices, without entailing any other design changes and fabrication protocols. We have successfully demonstrated such one-to-one replacement in spark igniter and piezo buzzer.*

Keywords: *Ceramic, Ferroelectric, Pb-free, non-resonant, Spark igniter, Piezo buzzer*

1. Introduction

Lead zirconatetitanate (PZT) based piezo-ceramics have been widely used in the manufacture of actuators, sensors, transducers, and other electromechanical devices because of their excellent piezoelectric properties [1]. However, PZT ceramics contain about 60% of toxic lead. Due to its volatility and high vapor pressure, it is released into the atmosphere during sintering, causing serious environmental and health problems. Another cause for concern is its disposal at the end of the life cycle [2]. Considering health concerns on account of Pb toxicity, governments world over have enacted laws that ban the use of lead in the manufacture of many products. Until now, materials based on PZT have dominated the industry of piezoelectric ceramics. Hence, there is a need to replace lead in the field of piezoelectric ceramics and limit environmental pollution. Eventhough a lot of literature on lead-free ferroelectric ceramics is available, deeper research leading to the application is needed to substitute lead-based materials in devices. Lead-free ferroelectric ceramics based on alkali niobates is one of the most promising materialsand is asubject of growing interest. Our approach has beento develop and/or modify environmentally safe piezoceramics with properties matching closely with PZT and which may replace specific piezo products. We believe this is achievable through the identified figure of merits (important material parameters) for a chosen application. We believe this will allow us to maintain the superiority of the piezo material performance when a specific piezo component is replaced directly in

a commercial PZT based device. In the present work, lead-free eco-friendly $Na_{0.4}K_{0.1}Bi_{0.5}TiO_3$ (NKBT) ceramic is chosen due to its high electromechanical coupling (0.54), high Curie temperature (320°), and excellent mechanical properties [3], [4]. In order to implement our objective, two applications of piezoceramic which are operated in non-resonance mode are considered. First is a spark igniter, a device that generates sparks on an application of mechanical force. This device works on direct piezoelectric effect, and PZT-4 is the current choice of material in this device. The second application is a piezo buzzer, in which a piezo disk is used (Fig 1). If a piezo disk is attached to a metal diaphragm, it becomes a speaker that can be used to create a high-pitched tone. The large bending caused due to theapplication of an electric field generates the sound of various tones. Arduino microcontroller can be used to play multiple tunes from the piezo buzzer. This piezo buzzerhas applications in shock detection, microphones, accelerometer, musical pickups,and in ultrasound imaging.

2. Experimental work

$Na_{0.4}K_{0.1}Bi_{0.5}TiO_3$ solid solution ceramic was prepared by solid-state reaction method. The detailed processing route is mentioned elsewhere [5]. Though the synthesis approach followed in this work is an established process, the repeatability of the properties is highly dependent on ensuring careful processing conditions.A spark igniter and a piezobuzzer wereprocured from the market and the piezo crystals present in it were removed. These piezo crystals were characterized by various techniques to identify the exact material used in these applications. XRD patterns of these removed piezo crystals and prepared NKBTceramic were collected using a powder X-ray diffractometer (PANalytical, USA) in the 2θ range of 20° – 80° with the step size of 0.020° at room temperature. The prepared NKBT ceramic is used in place of existing piezo crystals in the above stated devices. The performance of the devices was evaluated with this one-to-one replacement. For the spark igniter, the cylindrical samples of dimension (5 mm diameter and 10 mm height) were prepared. For buzzer application, disc shape samples of dimensions (20 mm diameter and 0.2 mm thickness) were prepared. The prepared piezoelectric disk was bonded to the brass plate with silver epoxy from MG Chemicals© (8331s-15g syringe). The schematic of the same is shown in Fig 1. The bonding layer was made as thin as possible. This bonded assembly was kept undervacuum for 15 min to remove any trapped air at the bond and cured at 80° for 1 h. The top surface of the piezoelectric disk was brushed with a silver electrode using n-butyl acetate as thinner for silver containing ink (SPI# 05002-GA). Later,the NKBT samplewas poled at a DC field of 25 kV/cm at RT for 30 minutes in a silicon oil bath, using a high-voltage DC power supply (Aplab, H5K02 N). The planar electromechanical coupling factor (kp) is calculated using the resonant and anti-resonant frequencies obtained from the impedance vs frequency spectrum. These spectra were recorded on a dielectric impedance analyzer (Novocontrol Alpha High-Resolution Dielectric Analyzer) for silver-coated poled-NKBT sample and piezo crystals from spark igniter and buzzer.P-E hysteresis loops were measured on a ferroelectric analyzer (TF Analyzer 2000, Aixact, Germany) using a triangular waveform at 1 Hz. The dielectric, ferroelectric and piezoelectric properties of all three samples (each from spark igniter, buzzer and prepared NKBT) were recorded and compared. The piezoelectric buzzers were tested using the Arduino microcontroller at an input

voltage of 5 V. The sound pressure level was measured in dB (Decibel) using the Sound Meter app.

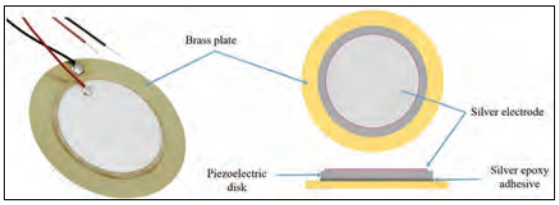

Fig. 1. Schematic of piezoelectric disk buzzer made with same dimensions for one-to-one replacement.

3. Results and Discussion

3.1 Phase analysis (XRD)

The XRD patterns of NKBT ceramic, piezo crystals from spark igniter and buzzer in the 2θ range of 20° to 80° with a step size of 0.02° are displayed in Fig 2. The XRD pattern of NKBT pellet sintered at 1150°C/ 3h confirms the expected perovskite phase formation without any impurity. The obtained pattern of NKBT matches well with the ICSD 98045 database and verifies the MPB composition with the coexistence of rhombohedral and tetragonal phases, which is necessary to obtain superior piezo properties. The recorded XRD patterns of piezo crystals from the spark igniter and buzzer match with PDF#70-4364 and PDF#70-4571 database which identifies these materials as PZT-4 and PZT-5H ceramics, respectively. PZT-4 is ahard piezoelectric ceramic, where the domain mobility is low. PZT-5H is a soft piezoelectric ceramic, where the domains can be easily switched with external parameters such as electric field, mechanical force and temperature.

3.2. Resonance and anti-resonance measurement

It is well known that the domains are randomly oriented in as-sintered ferroelectric polycrystalline ceramics. As a result, the net

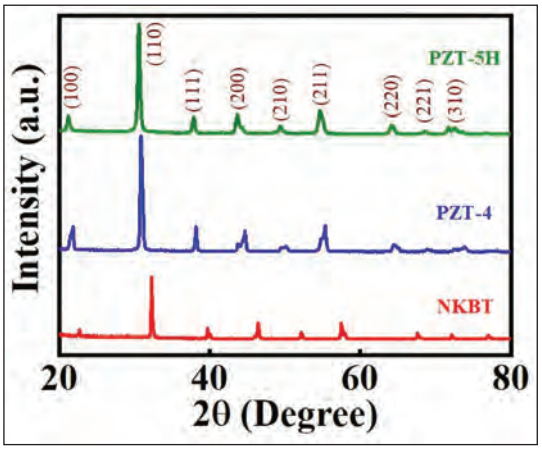

Fig. 2. Room temperature X-Ray diffraction patterns of NKBT, PZT-4 and PZT-5H ceramics.

spontaneous dipole moment is zero. Thus, in order to observe the intrinsic piezoelectric character, a 'poling' process is mandatory. Electrical poling is a process by which upon application of an external electric field, materials with random ferroelectric domain orientation become polarized with a non-zero polarization developed along the direction of the applied field. To know the extent of domain wall motion (poling) with respect to electric field and temperature, electrical impedance |Z| studies were performed as shown in Fig 3.

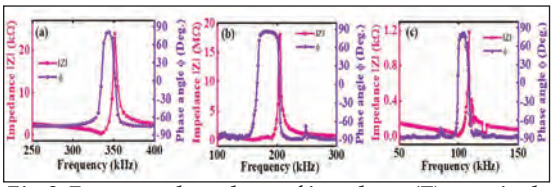

Fig. 3. Frequency dependence of impedance (Z) magnitude and phase angle (φ) for the (a) NKBT, (b) PZT-4 and (c) PZT-5H ceramics.

When a piezoelectric material is exposed to an AC electric field, the ceramic material changes dimensions cyclically at the cyclic frequency of the field. The frequency at which the ceramic material vibrates most readily, and converts the

electrical energy input into mechanical energy most efficiently, is the resonance frequency. The minimum impedance frequency is the resonance frequency, f_r. and the maximum impedance frequency is the anti-resonance frequency, f_{ar}.

It can be seen from Fig 3(a), the NKBT ceramic is fully poled. The hard PZT-4 (Fig 3(b)) and soft PZT-5H (Fig 3(c)) piezo crystals from the procured commercial spark igniter and buzzer, respectively, showed a high order of poling. The hard PZT-4, which contains acceptor ions shows a higher impedance in comparison to the soft PZT-5H ceramic. Since the soft PZT contains donor ions, which are responsible for the lower impedance. Also, the resonance frequency for the soft PZT-5H is smaller than for the hard PZT-4. However, in impact applications (spark igniter), operation at resonance frequency is not required. In a piezoelectric buzzer, since the piezoelectric disk is attached perpendicular to the poled direction, the disk undergoes flexure. A thinner disk coupled with a thin diaphragm undergoes more flexure since it requires a lower load for a required displacement than a thicker device. Consequently, a higher voltage is required for the thicker device for the same sound pressure level. It is also to be noted that resonance frequency will increase as the thickness decreases corresponding to the change in the capacitance of the material. The audible frequency range of humans is 20 Hz to 20000 Hz. So it is not possible to operate the buzzer at resonance for any of the piezoelectric materials studied in this work.

3.3. Dielectric and ferroelectric measurements - ε_r and PE Hysteresis loop

Figure 4(a) compares the room-temperature dielectric constant of NKBT, PZT-4, and PZT-5H ceramics as a function of frequency. The fluctuation in data points at higher frequencies is associated with resonance phenomena. Being a soft ferroelectric system, PZT-5H shows the highest dielectric constant. The high value of εr is utilized in capacitors, and coolants (mineral oil). The variation of ε_r as a function of temperature was also measured for all three ceramics to determine the corresponding Curie temperature (TC).

Figure 4 (b) shows the room - temperature polarization vs electric field (PE) hysteresis loops measured on NKBT, PZT-4 and PZT-5H ceramics under an applied alternating electric field of 50 kV/cm at 1 Hz. It's known that the PE loop is a fingerprint of ferroelectric materials. Hence, the obtained well-saturated and symmetric PE hysteresis loops exhibited the typical ferroelectric nature of these ceramics. A larger coercive field of 28 kV/cm for NKBT in comparison to PZT-based ceramics implies the hard ferroelectric nature of NKBT. The properties of NKBT and PZT ceramics are given in Table 1. A higher EC in PZT-4 than that of PZT-5H, classifies the PZT-4 ceramic as a hard ferroelectric. The higher E_C property of PZT-4 is utilized in high-power ultrasonic and sonar applications [6]. Smaller E_C for PZT-5H is attributed to the higher domain mobility. In severalapplications such as thickness gages, accelerometers, hydrophones, and musical pick-ups, a smaller E_C is useful.

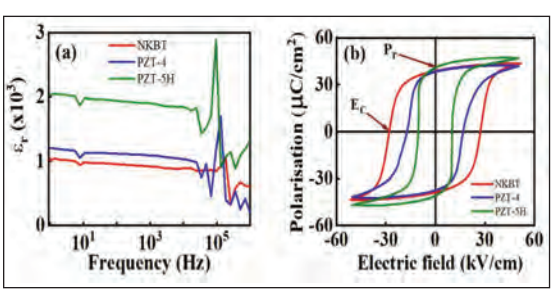

Fig. 4. Comparison of room temperature data, (a) Dielectric constant; (b) PE hysteresis loops of NKBT, PZT-4 and PZT-5H ceramics.

In one to one replacement of PZT-4 and PZT-5H ceramics by NKBT ceramic from the spark igniter and piezoelectric buzzer, respectively, the following observations are made:

- A viable spark is obtained from the spark igniter with the replaced NKBT ceramic. A high g33 coefficient of NKBTmade this replacement strategy successful in the spark igniter.
- An audible tune with 30 dB is attained from the piezo buzzer with the replaced NKBT ceramic. However, the piezo buzzer with PZT-5H crystal responds with 42 dB audible tune. A low value of d*33 coefficient of NKBT is the reason for its inferior performance compared to the PZT-5H. However, NKBT ceramic can be used to replace PZT-5H from the buzzer, where an audio tune of less than or up to 30 dB is required.

Table 1. Property comparison of NKBT, PZT-4 (hard) and PZT-5H (soft) ferroelectric ceramics.

Properties	Material systems		
	NKBT	**PZT-4**	**PZT-5H**
Dielectric constant, ε_r at 1 kHz	910	1100	1900
Curie temperature ( )	300	320	230
Remnant Polarization, P_r(μC/cm^2)	39	38	41
Coercive field, E_C (kV/cm)	28	17	11
Piezoelectric charge coefficient, d_{33} (pC/N)	198	430	610
Piezoelectric strain coefficient, d^*_{33} (pm/V)	326	-	650 [7]
Piezoelectric voltage coefficient, g_{33} x10^{-3} (V.m/N)	40	20 [8]	23
Coupling coefficient, Kp	0.54	0.58 [9]	0.74 [10]
Young's Modulus, E (GPa)	102	68 [11]	60 [12]
Fracture toughness, K_{IC} (MPa.m$^{0.5}$)	1.6	1.2	-
Compressive strength (MPa)	220	140	-

4. Conclusions

Developing new materials, without toxic elements to substitute existing devices, is a workable strategy. A good agreement in properties is observed between NKBT and hard PZT-4 ceramics, unlike soft PZT-5H ceramic. A one-to-one replacement of material is made in a spark igniter and piezo buzzer. A successful replacement of PZT-4 is demonstrated in the spark igniter. The NKBT buzzer could not reach the performance of PZT-5H buzzer. However, the applications requiring a maximum sound pressure level of (SPL) of 30dB, the NKBT buzzer can be used.

Acknowledgments

The authors are grateful to the IRCC, Indian Institute of Technology, Bombay, for the XRD, dielectric, and polarization (BDS) facilities. The authors would like to acknowledge Dr. Kaustubh Kambale, College of Engineering Pune, for availing poling facility.

References

1. S. Zhang et al., "Recent Developments in Piezoelectric Crystals," *J. Korean Ceram. Soc.*, vol. 55, no. 5, pp. 419–439, Sep. 2018, doi: 10.4191/kcers.2018.55.5.12.
2. M. Jaishankar, T. Tseten, N. Anbalagan, B. B. Mathew, and K. N. Beeregowda, "Toxicity, mechanism and health effects of some heavy metals," *Interdiscip. Toxicol.*, vol. 7, no. 2, pp. 60–72, Jun. 2014, doi: 10.2478/intox-2014-0009.
3. A. Ullah, C. Won Ahn, A. Ullah, and I. Won Kim, "Large strain under a low electric field in lead-free bismuth-based piezoelectrics," *Appl. Phys. Lett.*, vol. 103, no. 2, p. 022906, Jul. 2013, doi: 10.1063/1.4813420.
4. P. Varade, N. Shara Sowmya, N. Venkataramani, and A. R. Kulkarni, "Microstructural and mechanical behavior of Na0.4K0.1Bi0.5TiO3 ferroelectric ceramics," *Ceram. Int.*, vol. 48, no. 18, pp. 26546–26552, Sep. 2022, doi: 10.1016/j.ceramint.2022.05.350.
5. N. S. Sowmya, P. Varade, N. Venkataramani, and A. R. Kulkarni, "Lead-free Na0.4K0.1Bi0.5TiO3 ceramic: Poling effect and enhancement in electromechanical and piezoelectric voltage coefficient," *J. Eur. Ceram. Soc.*, vol. 40, no. 15, pp. 5384–5391, Dec. 2020, doi: 10.1016/j.jeurceramsoc.2020.07.010.

6. S. R. Anton, A. Erturk, and D. J. Inman, "Bending strength of piezoelectric ceramics and single crystals for multifunctional load-bearing applications," *IEEE Trans. Ultrason. Ferroelectr. Freq. Control,* vol. 59, no. 6, pp. 1085–1092, Jun. 2012, doi: 10.1109/TUFFC.2012.2299.

7. O. Bilgen, M. Amin Karami, D. J. Inman, and M. I. Friswell, "The actuation characterization of cantilevered unimorph beams with single crystal piezoelectric materials," *Smart Mater. Struct.,* vol. 20, no. 5, p. 055024, May 2011, doi: 10.1088/0964-1726/20/5/055024.

8. X.-G. Chen et al., "Two-Dimensional Layered Perovskite Ferroelectric with Giant Piezoelectric Voltage Coefficient," *J. Am. Chem. Soc.,* vol. 142, no. 2, pp. 1077–1082, Jan. 2020, doi: 10.1021/jacs.9b12368.

9. E. Taghaddos, T. Ma, H. Zhong, Q. Zhou, M. X. Wan, and A. Safari, "Fabrication and Characterization of Single-Aperture 3.5-MHz BNT-Based Ultrasonic Transducer for Therapeutic Application," *IEEE Trans. Ultrason. Ferroelectr. Freq. Control,* vol. 65, no. 4, pp. 582–588, Apr. 2018, doi: 10.1109/TUFFC.2018.2793874.

10. H. Boukabache, C. Escriba, and J.-Y. Fourniols, "Toward Smart Aerospace Structures: Design of a Piezoelectric Sensor and Its Analog Interface for Flaw Detection," *Sensors*, vol. 14, no. 11, pp. 20543–20561, Oct. 2014, doi: 10.3390/s141120543.

11. M. A. Fraga, H. Furlan, R. S. Pessoa, and M. Massi, "Wide bandgap semiconductor thin films for piezoelectric and piezoresistive MEMS sensors applied at high temperatures: an overview," *Microsyst. Technol.,* vol. 20, no. 1, pp. 9–21, Jan. 2014, doi: 10.1007/s00542-013-2029-z.

12. S. Shahab, S. Zhao, and A. Erturk, "Soft and Hard Piezoelectric Ceramics and Single Crystals for Random Vibration Energy Harvesting," *Energy Technol.,* vol. 6, no. 5, pp. 935–942, May 2018, doi: 10.1002/ente.201700873.